University of Southampton Research Repository

University of Southampton

Faculty of Engineering and Physical Sciences

Electronics and Computer Science

Microring resonators for vortex beam emission and their all-optical wavelength tuning

by

Hailong Pi

Thesis for the degree of Doctor of Philosophy

March 2022

University of Southampton

Abstract

Faculty of Engineering and Physical Sciences

Electronics and Computer Science

Doctor of Philosophy

Microring resonators for vortex beam emission and their all-optical wavelength tuning

by

Hailong Pi

A vortex beam possesses a helical phase front and carries a phase singularity along the propagation axis. The salient properties of vortex beams, including the theoretically unbounded orbital angular momentum (OAM) and spatially variant states of polarization (SOPs), have been utilized for a range of applications, including optical sensing, communications, manipulation and imaging. This thesis reports integrated vortex beam emitters and all-optical wavelength tuning based on microring resonators. The work may be further explored for potential applications such as light detection and ranging (LiDAR) and communication systems.

An integrated Terahertz (THz) vortex beam emitter is presented for the first time based on simulation to generate tunable OAM states. The design can convert infrared waveguide modes into a freely propagating THz beam via difference-frequency generation. The output OAM state carries a topological charge that is tunable with input wavelengths. Three devices are evaluated in a test frequency range from 9 THz to 13.5 THz, and the topological charge can change from -2 to 4. A frequency shift accompanies the change in the topological charge, and its magnitude depends on the planar dimensions of the emitter.

An on-chip vector vortex beam emitter is demonstrated for the first time via numerical simulation to generate all points on a first-order Poincaré sphere (FOPS). It consists of a waveguide-coupled, nanostructured Si microring resonator. The fundamental transverse electric and transverse magnetic input modes produce radial and azimuthal polarization, respectively. These two linear polarization states can form a pair of eigenstates for the FOPS. Consequently, tuning the phase contrast and the intensity ratio of these two coherent inputs can control the SOPs of generated vortex beams.

Flexible wavelength modulation of the generated vortex beams is desired to enhance sensing and communication performance. An all-optical wavelength tuning device is experimentally demonstrated based on two coupled microrings, which may combine with the proposed emitters. Pumping the symmetric and antisymmetric resonances of the device can induce attractive and repulsive optical gradient forces, respectively. The optical gradient forces can reconfigure the device and tune its resonant wavelengths. Besides, the wavelength difference between the symmetric and antisymmetric resonances can be significantly increased and decreased by the device's positive and negative pull-back instabilities, respectively.

Research Thesis: Declaration of Authorship

Print name: Hailong Pi

Title of thesis: Microring resonators for vortex beam emission and their all-optical wavelength tuning

I declare that this thesis and the work presented in it are my own and has been generated by me as the result of my own original research.

I confirm that:

1. This work was done wholly or mainly while in candidature for a research degree at this University;
2. Where any part of this thesis has previously been submitted for a degree or any other qualification at this University or any other institution, this has been clearly stated;
3. Where I have consulted the published work of others, this is always clearly attributed;
4. Where I have quoted from the work of others, the source is always given. With the exception of such quotations, this thesis is entirely my own work;
5. I have acknowledged all main sources of help;
6. Where the thesis is based on work done by myself jointly with others, I have made clear exactly what was done by others and what I have contributed myself;
7. Parts of this work have been published as journal papers and conference contributions in the list of publications.

Signature: Date:

Acknowledgements

First and foremost, I would like to thank my supervisors, Dr Jize Yan and Dr Xu Fang, for their dedicated support and guidance and giving me freedom in my dissertation study. Their professional knowledge, suggestions and encouragement would always inspire and help me solve problems. They are kind and generous persons who are willing to share their knowledge and experience. I felt privileged and truly grateful for the opportunity to work with them.

I would also like to thank Dr Carlo E. Campanella and Dr David J. Thomson for all the helpful support, insightful discussions and collaborative work. Their knowledge and experience have greatly helped my research.

I am very grateful to the staff of the Southampton Nanofabrication Centre, Dr Owian Clark, Dr Kiang Kian Shen, Dr Libe Arzubiaga Totorika, Dr Anushka Gangnaik, Dr Xiangjun Wang and Tracey Anscombe. They introduced the cleanroom facilities to me and helped me solve many problems during the fabrication process.

I want to thank my friends and coworkers, Dr Yu Feng, Xiangming Xu, Peng Li, Gaoce Han, Shumeng Wang, Wangke Yu and Chuang Sun. They help me a lot with numerical simulation, nanofabrication and experiments. I enjoyed the discussions with them. Their enthusiasm and persistence have always encouraged me during the research.

I would like to thank my friends and colleagues, Dr Bigeng Chen, Dr Han Du, Shiyue Yang, Fei He, James Frame, Shengqi Yin, Yue Fan, amongst many others. Without them, my PhD life would not be so enjoyable.

Finally, I would like to thank my parents and my dear wife, for all their love, support, encouragement and sacrifice. I would like to say every piece of my achievements also belongs to them.

Table of Contents

Definitions and Abbreviations

ATT	Attenuator
CMT	Coupled-mode theory
CVB	Cylindrical vector beam
DFG	Difference frequency generation
EBL	Electron beam lithography
FDTD	Finite-difference time-domain
FEA	Finite-element analysis
FOPS	First-order Poincaré sphere
FSR	Free spectral range
FWHM	Full width at the half maximum
HF	Hydrofluoric acid
HOP	Higher-order Poincaré
ICP	Inductively coupled plasma
LG	Laguerre-Gaussian
LHCP	Left-handed circularly polarized
LiDAR	Light detection and ranging
LNOI	Lithium niobate on insulator
nPBI	Negative pull back instability
OAM	Orbital angular momentum
OC	Optical coupler
PBI	Pull back instability
PC	Polarization controller
PD	Photodetector
PECVD	Plasma-enhanced chemical vapour deposition
pPBI	Positive pull back instability
RHCP	Right-handed circularly polarized

SAM	Spin angular momentum
SLM	Spatial light modulator
SOI	Silicon-on-insulator
SOP	State of polarization
SP	Stokes parameter
SPP	Spiral phase plate
TC	Topological charge
TE	Transverse electric
THz	Terahertz
TM	Transverse magnetic
VV	Vector vortex
WDM	Wavelength division multiplexer
WGM	Whisper gallery mode

List of Tables

List of Figures

List of Publications

Journal publications:

[1] H. Pi, T. Rahman, S. A. Boden, T. Ma, J. Yan, and X. Fang, "Integrated vortex beam emitter in the THz frequency range: Design and simulation," APL Photonics 5(7), 076102 (2020). (Featured)

[2] Q. Zhang, E. Plum, J. Y. Ou, H. Pi, J. Li, K. F. MacDonald, and N. I. Zheludev, "Electrogyration in metamaterials: chirality and polarization rotatory power that depend on applied electric field," Advanced Optical Materials 9(4), 2001826 (2021).

[3] X. Xu, H. Pi, W. Yu, J. Yan, "On-chip optical pulse train generation through the optomechanical oscillation," Optics Express, 29(23), 38781-38795 (2021).

[4] H. Pi, W. Yu, J. Yan, and X. Fang, "Coherent generation of arbitrary first-order Poincaré sphere beams on a Si chip," Optics Express, 30(5), 7342-7355 (2022)

[5] H. Pi, C. E. Campanella, D. J. Thomson, and J. Yan, "Positive and negative pull-back instabilities in mode splitting optomechanical devices," ACS Photonics, 9(1), 123-131 (2022).

Conference publications:

[1] H. Pi, F. He, J. Yan, and X. Fang, " Nonlinear generation of THz vortex beams with tunable orbital angular momentum in Si microdisks," CLEO/Europe-EQEC, Virtual conference, 20-25 June, 2021.

Chapter 1 Introduction to thesis structure

1.1 Introduction to thesis structure

A vortex beam is a light beam that possesses a helical phase front and propagates with a phase singularity [1]. In 1992, significant work linked these features to the angular momentum of the beam. Vortex beams were recognised carrying well-defined orbital angular momentum (OAM), which can be many times larger than the spin angular momentum (SAM) [2]. Since then, vortex beams have been explored for optical sensing, communication, manipulation and imaging. All of these fascinating applications demand desired vortex beams. Various generation approaches have been proposed, ranging from using free-space optical components to using integrated devices. Besides the OAM, vortex beams' states of polarization (SOPs) have also attracted great attention. Vortex beams with azimuthally varying polarization patterns are called vector vortex (VV) beams [3]. The transverse inhomogeneous polarization of VV beams has been utilized for many applications, including optical sensing, communications, trapping and microscopy. Many techniques for generating VV beams have been developed, evolving from using optical components in free space towards more compact solutions.

The field of vortex beams is still developing and could be explored for more potential applications, such as light detection and ranging (LiDAR) systems [4]. OAM states and SOPs provide two new degrees of freedom for obtaining objects’ information. Integrated light sources are highly desired for the applications to achieve compact volume. Photonic integration with advantages of compactness, reliability and scalability compared with bulk optics [5, 6] provides a great solution. Integrated vortex beam emitters can generate OAM and VV beams at the stage of light emission, eliminating the need for any subsequent light-conversion element. In this thesis, the scope of integrated, tunable vortex beam emitters is expanded. An integrated vortex beam emitter working in the Terahertz (THz) frequency range is demonstrated for the first time based on simulation. The output THz OAM state carries a topological charge that is tunable with input wavelengths. Controlled generation of VV beam based on a Si microring resonator is also explored. An on-chip VV beam emitter that can generate an arbitrary point on a first-order Poincaré sphere (FOPS) is demonstrated via numerical simulation. The generated vortex beams with flexible wavelength modulation are highly desired, benefiting sensing and communication applications. For example, potential LiDAR applications with wavelength modulation can achieve simultaneous distance and velocity measurement [7]. An all-optical wavelength tuning method based on microring resonators is experimentally demonstrated. The resonant wavelengths of the microring can be tuned by changing the pump’s wavelength. This all-optical wavelength tuning method may combine with the two proposed vortex beam emitters for providing wavelength-modulated vortex beams.

The contents of each following chapter are summarized as below. In chapter 2, the features of vortex beams, including OAM and SOPs, are introduced. The generation of OAM and VV beams are reviewed in detail. In Chapter 3, the first integrated THz vortex beam emitter is demonstrated via numerical simulation. THz waves are generated by the difference frequency generation (DFG) process in a nonlinear microring resonator and form whisper gallery modes (WGMs). A second-order grating is used to extract the confined OAM into the free space. Chapter 4 describes an integrated VV beam emitter on a Si microring based on simulation. The device can generate any polarization state on the FOPS by balancing the transverse electric (TE) and the transverse magnetic (TM) input modes without changing the input wavelength. In Chapter 5, an all-optical wavelength tuning device is experimentally demonstrated based on two coupled Si microrings. The resonant wavelengths of the device can be tuned by changing the pumping wavelength. Positive and negative pull-back instabilities are studied for the first time, originating from attractive and repulsive optical gradient forces, respectively. Chapter 6 summarizes the main achievements of my PhD study and presents future work that can be derived from this study.

Chapter 2 Optical vortex beams

Nowadays, optical vortex beams are exploited in various applications, including optical sensing, communications, optical manipulation, and imaging. One property of an optical vortex beam is carrying an OAM, discovered by Allen et al. in 1992 [2]. An optical vortex beam has a helical phase front and phase singularity along the propagation axis. OAM along the beam axis originates from the helical phase front and depends on the number of interwind helices and their handedness [1]. Apart from the OAM, the SOP of an optical vortex beam is also attracting great attention. When an optical vortex possesses a space-varying polarization pattern across the beam, the vortex beam is called a VV beam [3].

To date, optical vortex beams are still hot topics and are advancing many potential applications by the unique properties of the OAM and SOP. Creating a vortex beam with the corresponding property is the crucial first step for the various applications. The generation methods have been widely studied, ranging from using free-space optical components to using integrated devices. This chapter will describe the generation methods for the desired OAM and SOP of vortex beams.

2.1 Orbital angular momentum of light

Laguerre-Gaussian (LG) modes with circular symmetry are the earliest reported vortex beams carrying OAM. The modes are the solutions of the paraxial scalar Helmholtz equation in cylindrical coordinates [8-10]. The scalar Helmholtz equation is

$$(\nabla^2 + k^2)E = 0 \tag{2.1}$$

where $k = 2\pi/\lambda$ is the wavenumber, *E* is the electric field. A paraxial solution in cylindrical coordinates can be expressed as

$$E(r,\phi,z,t) = u(r,\phi,z)\exp[i(kz - \omega t)] \tag{2.2}$$

where $u(r,\phi,z)$ is the amplitude distribution, ω is the angular frequency. By substituting the equation into the scalar Helmholtz equation and applying the slowly varying envelope approximation which can be expressed as

$$\frac{\partial^2 u}{\partial z^2} \ll k^2 u, \frac{\partial^2 u}{\partial z^2} \ll \frac{\partial u}{\partial z} \tag{2.3}$$

The scalar Helmholtz equation becomes

$$\frac{1}{r}\frac{\partial}{\partial r}(r\frac{\partial u}{\partial r})+\frac{1}{r^2}\frac{\partial^2 u}{\partial \phi^2}+2ik\frac{\partial u}{\partial z}=0 \tag{2.4}$$

From the equation, the LG solution LG_p^l modes can be obtained

$$LG_p^l=\sqrt{\frac{2p!}{\pi(p+|l|)!}}\frac{1}{w(z)}\left[\frac{r\sqrt{2}}{w(z)}\right]^{|l|}\exp\left[\frac{-r^2}{w^2(z)}\right]L_p^{|l|}\left(\frac{2r^2}{w^2(z)}\right)\exp\left[il\phi\right]$$

$$\exp\left[\frac{-ikr^2z}{2(z^2+z_R^2)}\right]\exp\left[-i(2p+|l|+1)\tan^{-1}(\frac{z}{z_R})\right] \tag{2.5}$$

where $w(z)=w(0)[(z^2+z_R^2)/z_R^2]^{1/2}$ is the $1/e$ radius of the Gaussian term, with $w(0)$ being the beam waist and z_R being the Rayleigh range. $L_p^{|l|}$ is the generalized Laguerre polynomials. $(2p+|l|+1)tan^{-1}(z/z_R)$ is the Gouy phase. p determines the number of concentric rings in the intensity distribution. l determines the azimuthal phase term exp $[il\phi]$. The phase term shows that the phase evolves by $2\pi l$ when transversing a close path around the axis (r=0). The integer l is called the topological charge (TC).

Figure 2.1 shows phase distributions of LG beams with l=-1, 0, 1, 2 and p=0. When l is zero, the beam is the fundamental Gaussian beam. For l≠0, each phase distribution shows a helical phase front. The number of intertwined helices increases with the magnitude of l. For the beams with TCs of l=±1, the numbers of intertwined helices are the same. However, their handedness is different due to the signs of the TCs l.

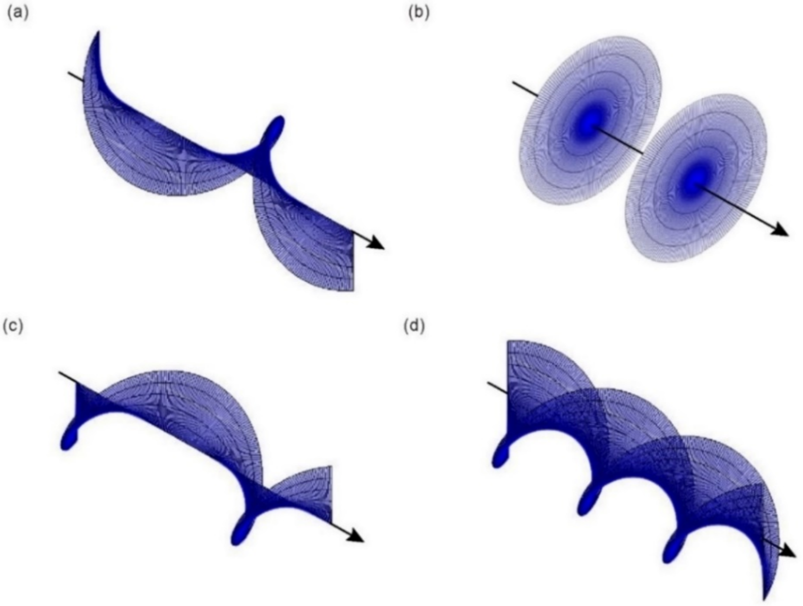

Figure 2.1 Helical phase fronts of optical vortex beams with toplogical charges of (a) l=-1, (b) l=0, (c) l=1, (d) l=2.

Figure 2.2 shows the normalized intensity and phase distributions of LG modes. Here, the LG modes are chosen as LG_0^1, LG_1^1 and LG_1^2. In the intensity cross-section, there are p+1 concentric rings with a zero on-axis intensity. In the phase cross-section, the accumulated phase is $2\pi l$ when traversing a closed path around the axis.

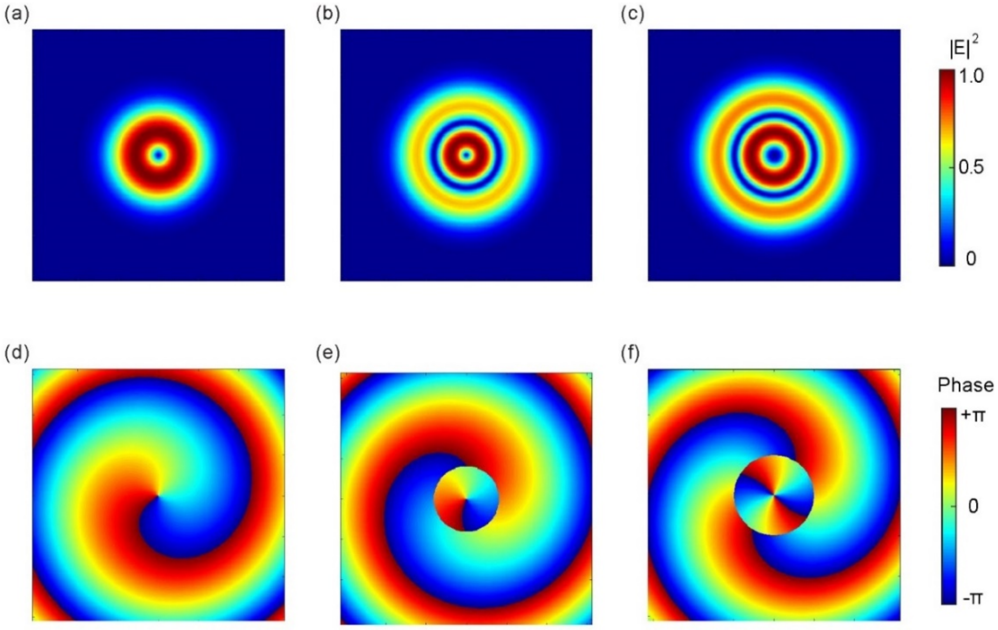

Figure 2.2 Normalized intensity and phase distributions of Laguerre-Gaussian modes: (a) LG_0^1, (b) LG_1^1, (c) LG_1^2.

The helical phase structure is associated with the OAM of LG modes [1, 11]. The Poynting vector is at all times parallel to the surface normal of the phase front, and an azimuthal component of the Poynting vector is around the beam. Therefore, there is an OAM along the beam axis. The OAM of the optical vortex beam can be characterized by using the Poynting vector [1] or the canonical momentum density [12, 13]. Compared to the Poynting vector, the canonical momentum density can be applied to inhomogeneous optical fields and separate the OAM from the SAM of light. Here the canonical momentum density is used to characterize the OAM. The momentum density of light in free space can be written as [13]

$$\boldsymbol{P} = \frac{g}{2}\mathrm{Im}\left[\boldsymbol{E}^* \cdot (\nabla)\boldsymbol{E} + \boldsymbol{H}^* \cdot (\nabla)\boldsymbol{H}\right] \tag{2.6}$$

where ***E*** and ***H*** are the electric and magnetic fields of light. Gaussian units with $g = (8\pi\omega)^{-1}$ are used. The canonical OAM density is expressed as

$$\boldsymbol{L} = \boldsymbol{r} \times \boldsymbol{P} \tag{2.7}$$

An optical vortex beam propagating along the z-axis can be expressed as

$$\boldsymbol{E}(r,\phi,z) = A(r,z)\frac{\hat{\boldsymbol{x}} + m\hat{\boldsymbol{y}}}{\sqrt{1+|m|^2}}\exp(ikz + il\phi) \tag{2.8}$$

where $A(r,z)$ is the amplitude of the beam, m is a complex number, which characterizes the polarization.

The average OAM can be derived as

$$\frac{\boldsymbol{L}}{W} = \frac{l}{\omega}\frac{\boldsymbol{k}}{k} \tag{2.9}$$

where the averaged energy density $W = \frac{g\omega}{2}(|\boldsymbol{E}|^2 + |\boldsymbol{H}|^2)$ and k is the wavevector. The energy of a single photon is $\hbar\omega$. Therefore, the light with azimuthal dependent phase exp $(il\phi)$ carries an OAM of $l\hbar$ per photon. The magnitude of OAM of light is determined by the TC l. It is theoretically unbounded. Generation of light vortices carrying more than 10^4 orders of OAM has recently been demonstrated [14]. Numerous applications taking advantage of this unbounded OAM have emerged, which will be described in section 2.2.

2.2 Applications of OAM

In addition to the physical properties of light, for example, the frequency, amplitude, wavelength, polarization and SAM, the theoretically unbounded OAM provides another degree of freedom for photonic technologies. The OAM has been studied for various applications in a wide variety of fields, such as optical sensing, optical communication, quantum communication, manipulation and imaging.

2.2.1 Sensing applications

Optical fields are of great importance in sensing since they allow for high contact-less sensitive techniques. OAM has been used to detect spinning objects. When a light beam with OAM is scattered from a spinning object, the light beam will undergo a frequency shift. This phenomenon is called the rotational Doppler effect [15]. The frequency shift is proportional to the product of the rotation frequency of the object and the OAM of the light. The rotational Doppler effect has been experimentally verified by building a 120-m free-space optical link in a realistic city environment [16]. In order to improve the measurement sensitivity, interferometers have been utilised [17-19]. Using an OAM with TC of l=5050, the sensitivity can be as high as 3×10^{-9} rad/s [20]. Recently, the OAM has been studied for refractive index sensing [21]. The refractive index is measured by the orientation change of the light's intensity profile when vortex beams are superposed. The mentioned sensing applications are based on the OAM modes in the free space. The OAM in optical fibres has also been explored for sensing, such as temperature [22], strain [23], refractive index [24] measurement.

Besides detecting targets' rotational motion, OAM has been explored to detect objects' lateral motion [25]. By analysing the changes in OAM of a titled light beam eclipsed by a moving object, the object's lateral motion can be detected using a single light beam. OAM can also be used to acquire a target's azimuthal information [26]. The range of employed OAM modes decides the azimuthal resolution. A higher resolution can be obtained when more modes are utilized. Recently, the OAM has been studied for identifying an object's shape information [27]. This is achieved by determining the difference between the OAM spectra of the indecent and outgoing light. OAM beams provide a new degree of freedom for object detection and have the potential to improve sensing performance. Currently, LiDAR technology, a laser-based sensing technique for accurate distance measurement, has been one of the most crucial sensor technologies for autonomous vehicles and artificially intelligent robots [4]. The detecting methods based on OAM beams are promising to be the supporting or alternative technologies to the conventional LiDAR systems.

2.2.2 OAM in communication

The potentially unlimited number of OAM states provides new freedom for encoding information, enlarging the capacity of optical communication. Terabit level of data rates has been demonstrated by OAM multiplexing in free space [28]. In free space, the transmission of OAM modes of light over a distance of 143 km has been demonstrated [29]. Inevitably, the performance of optical free-space communication based on OAM multiplexing will be influenced by turbulence and microparticles in the atmosphere. The wavefront of the OAM modes would be scrambled, and the orthogonality between OAM channels would be destroyed. Recently, OAM transmission under atmospheric turbulence [30] and high scattering [31] have been studied. These techniques would benefit the high-performance optical communication in turbulent environments.

Compared to the free-space-based OAM multiplexing, fibre-based OAM multiplexing is suitable for short-distance communication in a complex environment. Terabit-scale OAM division multiplexing in fibres have been demonstrated [32]. The OAM multiplexing devices are based on free-space optics, which increases the complexity of the fibre-based system. In order to achieve simple and practical applications, an integrated fibre-based OAM (de)multiplexer has been proposed. A vortex grating fabricated on the fibre facet enables the direct multiplexing and demultiplexing of OAM states [33]. Recently, an optical fibre communication system was proposed based on a micrometresized silicon optical vortex beam emitter [34]. This technique paves the way to use integrated photonic devices as transceivers in an OAM-based optical fibre communication system.

2.2.3 Quantum communication

OAM of light has engendered many applications in quantum information and science and quantum technology [35]. Higher-dimensional quantum key distribution protocols can be achieved based on mutually unbiased bases, implemented by photons carrying OAM. The increase in dimension can increase information capacity and achieve higher key generation rates per photons [36]. Current research is trying to enlarge the distance over which secure keys can be distributed [37, 38]. Using OAM has also enabled the quantum teleportation of two degrees of freedom of a single photon. This technique can improve the technical control of scalable and complicated quantum technologies [39]. Optical quantum cloning of OAM photon qubits has also been demonstrated through Hong-Ou-Mandel coalescence interference, which is useful for distributing quantum information and security assessment of quantum cryptography [40]. Storing OAM photonic qubits in matter systems is of great importance for the quantum techniques mentioned above. Quantum memory for storing and retrieving OAM qubits has been proposed using a dynamic electromagnetically induced transparency protocol [41]. Recently, a dielectric metasurface has been utilized to generate quantum entanglement of spin and orbital angular momentum of photons [42]. This progress would lead to integrated quantum optic circuits operating on a nanophotonic platform.

2.2.4 Optical manipulation

Optical trapping has been very active since 1970 and was typically accomplished with a single Gaussian beam [43]. Absorbing particles usually cannot be trapped stably by the normal optical tweezer due to the high scattering force [44]. The dark centre of an optical vortex beam provides a suitable tool for trapping these particles. Meanwhile, the OAM of the vortex beam can be transferred to the particles, leading them to rotate around its axis [45]. When combined with SAM, the OAM can control the spinning of a trapped particle. A beam with l=1 and σ=1 or σ=-1 has a total angular momentum of 0 and $2\hbar$ per photon, respectively. The two total angular momenta can stop or start the spinning of the trapped particle, respectively [46]. In addition to the absorbing particles, metal nanoparticles and low-refractive-index particles can also be trapped using an optical vortex beam [47, 48]. The mentioned particles are typically large compared with the beam size. When the focused beam is larger than the particle, the particle will be confined off-axis with respect to the beam. OAM causes it to orbit around the beam axis [49, 50]. With the control of multiple optical vortex beams, multiple particles can be trapped on the beams' bright circumference and circulate rapidly around the rings. These circulating particles can create flow and can be used as an optically driven pump [51].

2.2.5 Optical imaging

OAM has also led new approaches within imaging. The annular intensity cross-section of a vortex beam can be used to null bright points of light which might overwhelm the image. This approach has been used within a telescope to suppress light from a bright star to observe neighbouring objects [52]. Microscopic techniques have also benefited from the OAM. A new form of interferometric has been proposed using a helically phased beam as a reference wave. A complete sample profile can be reconstructed from a single exposure [53]. By exploiting the spiral phase of a vortex beam for edge contrast enhancement, high-resolution imaging can be achieved in light microscopy and stimulated emission depletion microscopy techniques [54]. Optical vortex beams can also combine with surface plasma. Fluorescence microscopy was demonstrated using standing surface plasmon waves induced by optical vortices, achieving high-resolution wide-field imaging [55]. A perfect vortex beam can be used to improve the performance of this microscopy further. This type of optical vortex beam can improve the efficiency of the excitation of surface plasma and reduce the background noise of the excited fluorescence [56].

2.3 Generation methods

All the fascinating applications described in section 2.2 require the stable creation of vortex beams. Various generation methods have been studied [57], which can be classified as passive or active, depending on whether amplifying media is involved. The passive generation methods include the dynamic phase plate and geometric phase plate. The active methods include free-space lasers and integrated OAM lasers.

2.3.1 Passive generation methods

2.3.1.1 Dynamic phase plates

The generation of OAM modes relies on constructing a specific phase distribution by introducing optical path differences. A spiral phase plate (SPP) can introduce such optical path differences by providing a thickness gradient varying along the azimuthal angle. The first SPP for OAM generation was implemented in 1994 using conventional machining, as shown in Figure 2.3(a) [58]. The required spiral phase structure can also be mapped onto the surface of a mirror instead of using a thin transparent plate. A spiral phase mirror has been produced by direct machining with a diamond turning lathe [59]. A TC of more than 10000 has been produced based on this device, as shown in

Figure 2.3(b) [14]. However, the machined spiral phase devices are macroscopic. Direct laser writing techniques are promising approaches to downsize SPPs. An SPP with a diameter of several micrometres has been demonstrated [60]. The technique has also been used to fabricate SPPs on fibre tips [61].

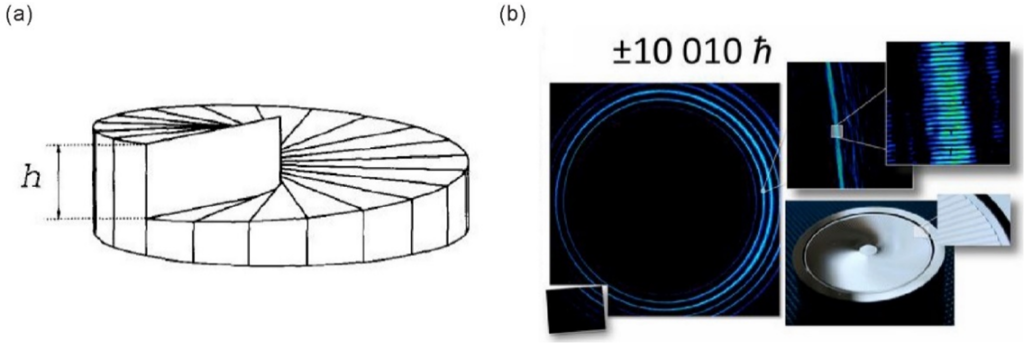

Figure 2.3 Spiral phase plates for the generation of OAM modes. (a) The schematic of the spiral phase plate [58]. (b) The spiral phase mirror for generating the topological charge of 10010 [14].

Metasurfaces with thin surfaces provide a promising solution to achieve compact SPPs. A metasurface consists of a two-dimensional array of optical resonators, imprinting phase discontinuities on propagating light. Subwavelength metallic nanoantennas and thin films have been proposed to be optical resonators [62, 63]. By engineering the geometries of resonators, the desired spatial gradient of the phase discontinuity along the azimuthal angle of the metasurface can be achieved. Figure 2.4(a) shows an ultra-compact array of nanowaveguides composed of cylindrical holes [64]. The nanowaveguides were milled in a thin silver film and filled with a dielectric material. Each nanowaveguide introduces a specific phase change determined by the radius of the hole. By choosing the spatial distribution of the nanowaveguide radii, a total phase change of 2π can be achieved. When a conventional beam transmits the metasurface, a far-field vortex beam with a TC of l=1 is obtained. Apart from the far-field vortex beams, metallic metasurfaces have also been used to create near-field vortices. Figure 2.4(b) shows a metasurface formed by nanocavities embedded in a gold thin film. A surface plasmon vortex can be generated when the metasurface is pumped by linearly polarized light [65].

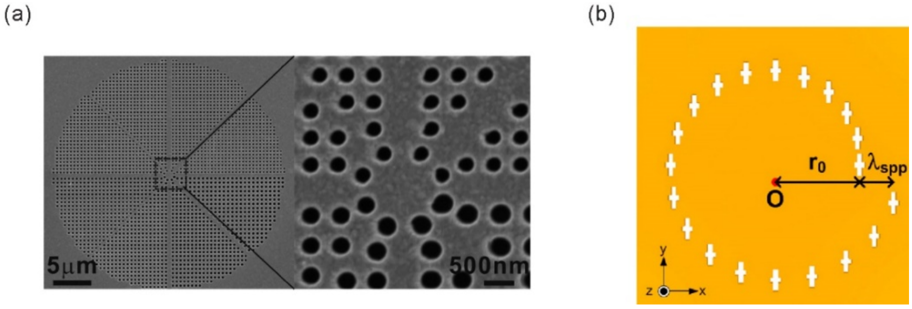

Figure 2.4 Spiral phase plates based on metasurfaces for the generation of optical vortex beams. a) Nanowaveguide array milled in a thin silver film [64]. (b) Nanocavities are arranged as an Archimedes spiral inscribed in a gold thin film [65].

The metallic metasurfaces for OAM generation at optical frequency introduce high ohmic loss and absorption [66]. As a result, the transmission efficiency is low. This limitation can be overcome by replacing metals with all-dielectric resonators. Dielectric metasurfaces consist of interfaces patterned with a distribution of high-index dielectric light scattering particles [67]. Figure 2.5(a) shows a dielectric metasurface composed of silicon nanodisks [68]. The transmission efficiency of this device exceeds 70%. A Gaussian beam is converted to a vortex beam with a TC of l=1. The required spatial distribution of transmitted phases for OAM generation is achieved by varying the lattice periodicity in the array. Recently, dielectric metasurfaces based on silicon cross-shaped resonators [69] and cylindrical pillars [70] have been proposed to provide desired spatially varying phase shifts to the incident light. These metasurfaces are insensitive to the polarization of the incident light and can generate OAM modes in mid-infrared and THz regions.

OAM modes can also be generated by holograms that resemble diffraction gratings. The required diffraction grating can be displayed on a holographic film or a spatial light modulator (SLM) [8]. However, the methods employ bulk optics and have a low spatial resolution. Recently, metasurface grating with subwavelength structures has been explored to work as holograms. A device comprising a bilaterally symmetric grating with an aperture was proposed, as shown in Figure 2.5(b) [71]. The device is encoded with a phase profile that has regularly distributed singularities. By employing a gradually varying aperture, optical vortex beams are generated with controllable OAM values continuously varying over a rational range. An all-dielectric metasurface grating has also been demonstrated for the simultaneous generation of multi-channel OAM beams with the TCs from l=-3 to +3 [72]. The encoded fringes are produced by off-axis interference between vortex beams and a Gaussian beam. When a vortex beam coaxially interferes with a Gaussian beam, spiral fringers can be created. The spiral fringers have also been encoded onto metasurfaces for OAM generation [73].

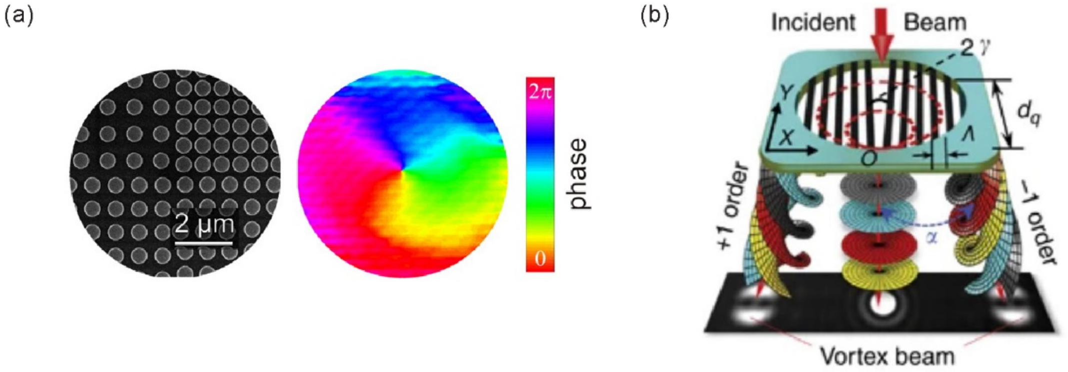

Figure 2.5 Generation of optical vortex beams by (a) Silicon nanodisks with high refractive index [68]. (b) Metasurface fork grating hologram with an open circular aperture [71].

2.3.1.2 Geometric phase plates

When the light changes its initial polarization state to a final polarization state along different paths on the Poincaré sphere, there will be a phase difference between the two final polarization states [74, 75]. The phase difference is the geometric phase, which can be used to construct the required spiral phase distribution for OAM generation. In 2002, space-variant subwavelength dielectric gratings utilizing the geometric phase were proposed to generate vortex beams in the mid-infrared region [76]. Figure 2.6 shows the geometry of the subwavelength gratings. Since the grating period is smaller than the incident wavelength, each groove acts as a polarizer where the transmission axis varies across the profile of the beam. The device was fabricated by using a photolithographic process, and the fabrication resolution is limited. So, the operating frequency is in the mid-infrared range. Later, a q-plate based on birefringent liquid crystals was introduced to produce OAM modes [77]. The device introduces the geometric phase by an azimuthal pattern of the liquid crystal molecular director around a central point. q presents the constant angular rotation velocity of the anisotropy of the device. This work illustrates that the input polarization controls the wavefront helicity of generated vortex beams due to the spin-orbit interaction, which simplifies the generation of OAM modes.

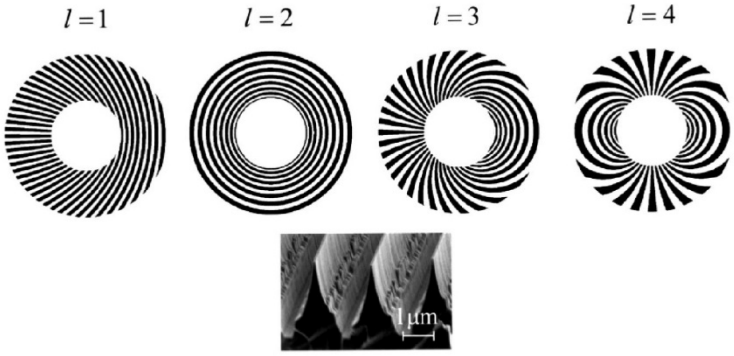

Figure 2.6 Geometry of the subwavelength gratings for generating four topological charges [76].

Metasurfaces with subwavelength structures are proposed to reduce the size of geometric phase plates. A metasurface based on V-shaped nanoantennas arrays was proposed to generate optical vortex beams, as shown in Figure 2.7(a). There are eight regions arranged to generate a phase shift that varies azimuthally from 0 to 2π. A Gaussian beam passing through the metasurface can produce the optical vortex with a TC of l=1 [78]. Another geometric phase metasurface was demonstrated based on a space-variant array of plasmonic gold nano-antennas. The device operates at a visible wavelength and can convert the circularly polarized light to optical vortex beams with the TCs of l=±2 [79]. Apart from using nanoantennas, space-variant nanoslits on a thin gold film were used to generate optical vortex beams. The device can generate an optical vortex with a TC of up to l=10 in the visible domain [80]. The mentioned metasurfaces device can only generate the optical vortex beams while lacking the ability to separate the coupled SAM-OAM modes of light. A metasurface fork grating was proposed to achieve the generation and splitting of OAM modes. Figure 2.7(b) shows that the metasurface consists of spatially variant nanoslits on an ultrathin metal film [81]. The device can generate optical vortices with various OAM states and splits these optical vortex beams into different diffraction orders according to their SAM states. In addition to using metallic nanostructures, geometric phase metasurfaces can be achieved by using dielectric scatters. The dielectric metasurface can achieve high conversion efficiency for the visible wavelength. A metasurface based on titanium dioxide with an efficiency of 60% has been demonstrated when the wavelength is 532nm [82].

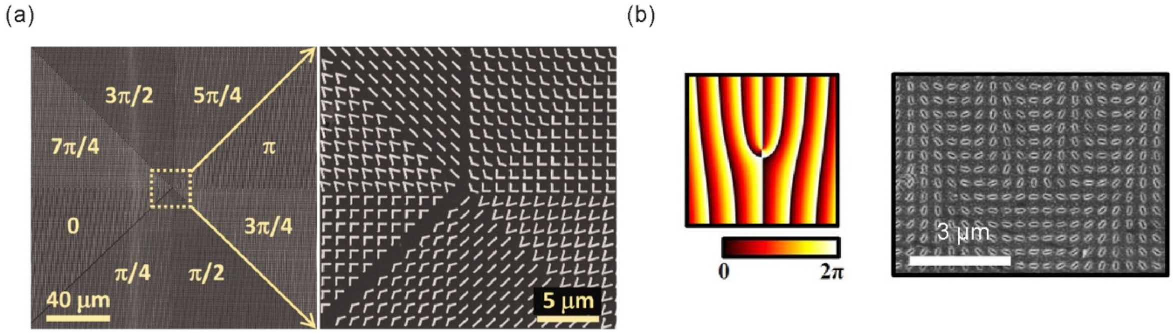

Figure 2.7 Geometric phase metasurfaces for generating optical vortex beams. (a) A plasmonic interface consists of eight regions, each occupied by one constituent antenna [78]. (b) A metasurface hologram generates optical vortex beams and splits the beams simultaneously [81].

These devices based on the geometric phase can only permit the conversion of left-handed circularly polarized (LHCP) and right-handed circularly polarized (RHCP) beams into modes with opposite OAM states. A possible approach to generate arbitrary OAM states is combining a geometric phase plate and a dynamic phase plate. Figure 2.8(a) shows the combination of two discrete plates. For RHCP incident light, the output beam has the TC of l=0. For LHCP incident light, the output beam has the TC of l=2 [83]. The combination of dynamic and geometric phase plates has been implemented on a metasurface recently. Figure 2.8(b) shows the metalens. The LHCP beam is converted to the OAM mode with the TC of l=3, while the RHCP beam is converted to the mode with l=4. Besides, arbitrary generation of OAM states has also been demonstrated by using orthogonal elliptical polarization states [84].

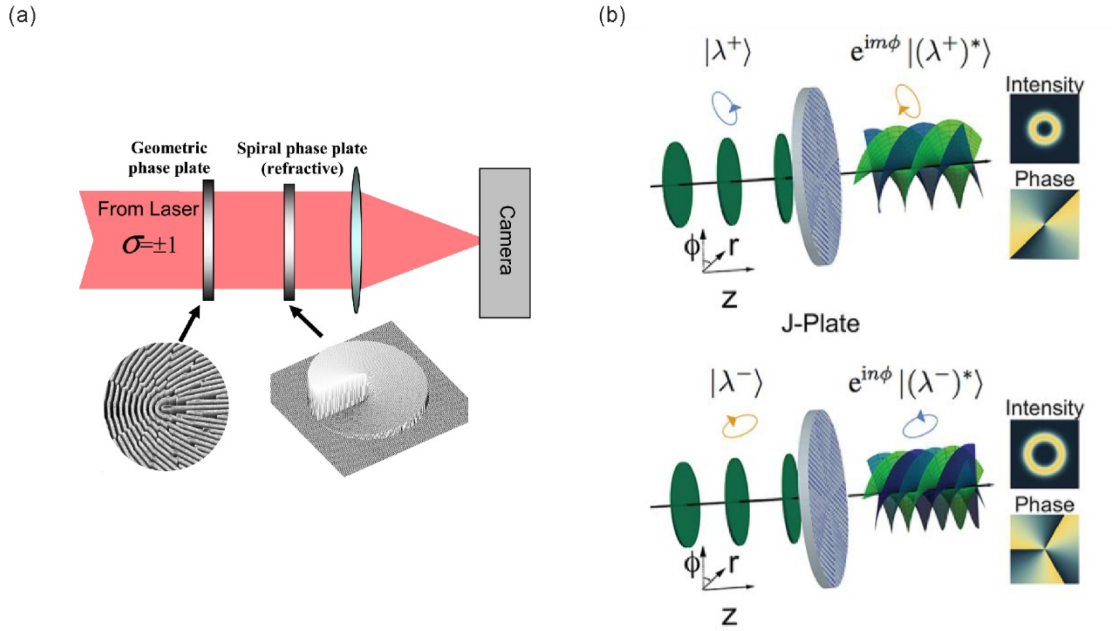

Figure 2.8 Arbitrary spin-to-orbital angular momentum conversion. (a) Schematic illustration of the independent spin-orbit conversion based on a geometric phase plate and a dynamic phase plate [83]. (b) Illustration of a hybrid metasurface plate for arbitrary OAM generation [84].

2.3.2 Active generation methods

2.3.2.1 Free space OAM lasers

Optical vortex beams can be directly generated from a laser. An approach based on the superposition of two orthogonal modes has been proposed [85]. However, this method requires sophisticated alignment procedures of intra-cavity absorbers and apertures for controlling the transverse modes. Techniques such as inserting Dove prism [86], spiral phase elements [87] inside laser cavities have been proposed to simplify the generation process. Figure 2.9(a) shows the laser using a spatial phase element for obtaining a pure and stable optical vortex beam. The spiral phase elements are used to discriminate and select a single high order LG mode [87]. Many approaches for mode selection inside laser cavity have been implemented, for example, using phase-only [88], amplitude-only [89] and phase-amplitude combination optical elements [90]. However, all these techniques require custom optics. It is challenging to achieve an on-demand selection of arbitrary laser mode. A digital laser using intra-cavity digital holograms was proposed to overcome the limitation. Figure 2.9(b) shows the schematic of the digital laser [91]. Holograms are implemented on a reflective SLM to form a holographic mirror. The phase and amplitude of the holographic mirror can be controlled simply by writing a computer-generated hologram.

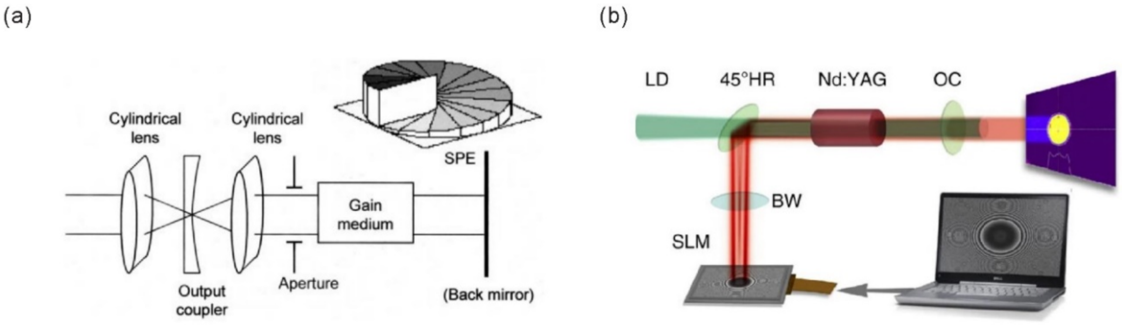

Figure 2.9 Generation of OAM modes based on free-space lasers. (a) Laser resonator configuration based on a spatial phase element (SPE) [87]. (b) Schematic of the digital laser based on a spatial light modulator [91].

Recently, subwavelength nanostructures based on spin-orbit interaction have been used inside laser cavities for optical vortex generation. Figure 2.10(a) shows that a geometric phase metasurface is used inside a laser cavity. The metasurface based on silicon nanoantennas is combined with an Nd: YAG laser. The SAM of the incident light can control the TCs of generated OAM modes. For the LHCP incident light, the generated TC is l=1. On the contrary, the generated TC is l=-1 for the RHCP incident light [92]. This laser can only convert the LHCP and RHCP states into opposite OAM states. Breaking the symmetry of the spin and orbital states for arbitrary OAM generation at the source is still challenging. A laser with an intracavity metasurface provides a promising solution. Figure 2.10(b) shows the intracavity implementation. The J plate can convert any two orthogonal polarization states of the incident light into helical modes with any arbitrary values of OAM. The laser was demonstrated to produce simultaneously two vortex beams with TCs being l=100 and 10, respectively [93].

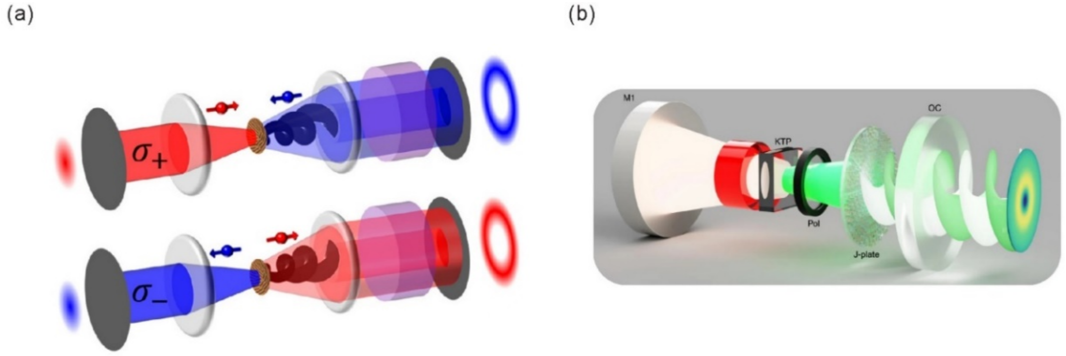

Figure 2.10 Generation of OAM states using subwavelength nanostructures involves spin-orbit interaction inside laser cavities. (a) Illustration of a laser cavity based on a geometric phase plate. The TCs of the generated OAM beams can be controlled by the SAM of the incident light [92]. (b) Illustration of laser cavity based on a metasurface (J-plate) for generating an arbitrary OAM state [93].

2.3.2.2 Integrated OAM lasers

Photonic integration has attracted great attention recently due to advantages of reliability, miniaturization and scalability compared with bulk optics [5]. Recent advances in the fields of nanofabrication make the integrated OAM generator possible. A compact integrated OAM emitter was proposed based on a microring resonator [94]. Figure 2.11(a) shows the emitter with angular grating patterned along the inner wall of a microring resonator. The gating can extract light confined in WGMs with high OAM into free-space beams with controlled amounts of OAM. The amount of the OAM is determined by the difference between the azimuthal order of the WGM and the number of grating elements. This work is significant progress to achieving an integrated OAM generator. However, the emission efficiency is low as most of the emitted power leaks to the substrate. A vortex beam emitter was proposed to improve emission efficiency using a metal mirror underneath the silicon microring. The mirror reflects the propagating components emitting down to the substrate back to air. The emission efficiency of the emitter was up to 37% [95]. The mentioned devices can only operate in a narrow bandwidth as the high-quality factor of the WGMs. Recently, an ultra-broadband multiplexed OAM emitter was proposed [96]. Figure 2.11(b) shows that the emitter has a circular shape containing subwavelength structures and is connected to two single-mode waveguides. The subwavelength structures enable joint phase control of the optical path and local resonances. The operating bandwidth is across the entire telecommunication band from 1450 to 1650nm.

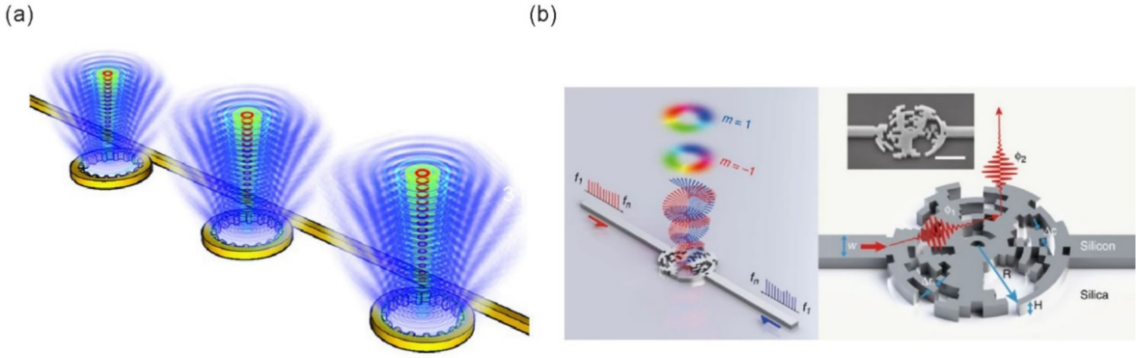

Figure 2.11 Integrated optical vortex beam emitters. (a) Schematic of integrated optical vortex emitters based on silicon waveguides. The angular grating patterns scatter OAM light into the free space [94]. (b) Schematic of a broadband OAM emitter that can be used for OAM multiplexing and demultiplexing [96].

The mentioned integrated OAM emitters are passive devices and require external laser sources. The external sources would increase the complexity and decrease the stability of emitters. There is an increasing demand for the realization of vortex lasing based on an integrated chip. One type of vortex laser has been proposed by adding a micro-SPP at the output port of a vertical-cavity surface-emitting laser, as shown in Figure 2.12(a) [97]. The SPP can impart a helical phase term to a Gaussian beam. The SPP is fabricated in a 1000 nm thick silicon nitride film and patterned using a focused ion beam etching technique. Another approach for eliminating the required external laser is using a microlaser that simultaneously generates light and the OAM mode. Figure 2.12(b) shows an OAM microlaser on an InP substrate [98]. A microring laser is used to provide a unidirectional WGM by introducing complex refractive-index modulations to form an exceptional point. The microlaser has been demonstrated to produce a single-mode OAM vortex lasing with the ability to define the TC precisely. The device is optically pumped, which limits its applications in telecommunications. Recently, an integrated electrically pumped OAM laser operating at telecom wavelengths has been demonstrated [99]. Figure 2.12(c) shows the structure of the laser. It contains a microring-based vortex emitter with a distributed feedback laser fabricated on an InGaAsP/InP epitaxial wafer. Light from the distributed feedback laser is unidirectionally coupled into the optical vortex beam emitter. The OAM-carrying beam will be emitted vertically once the light is in resonance within the microring.

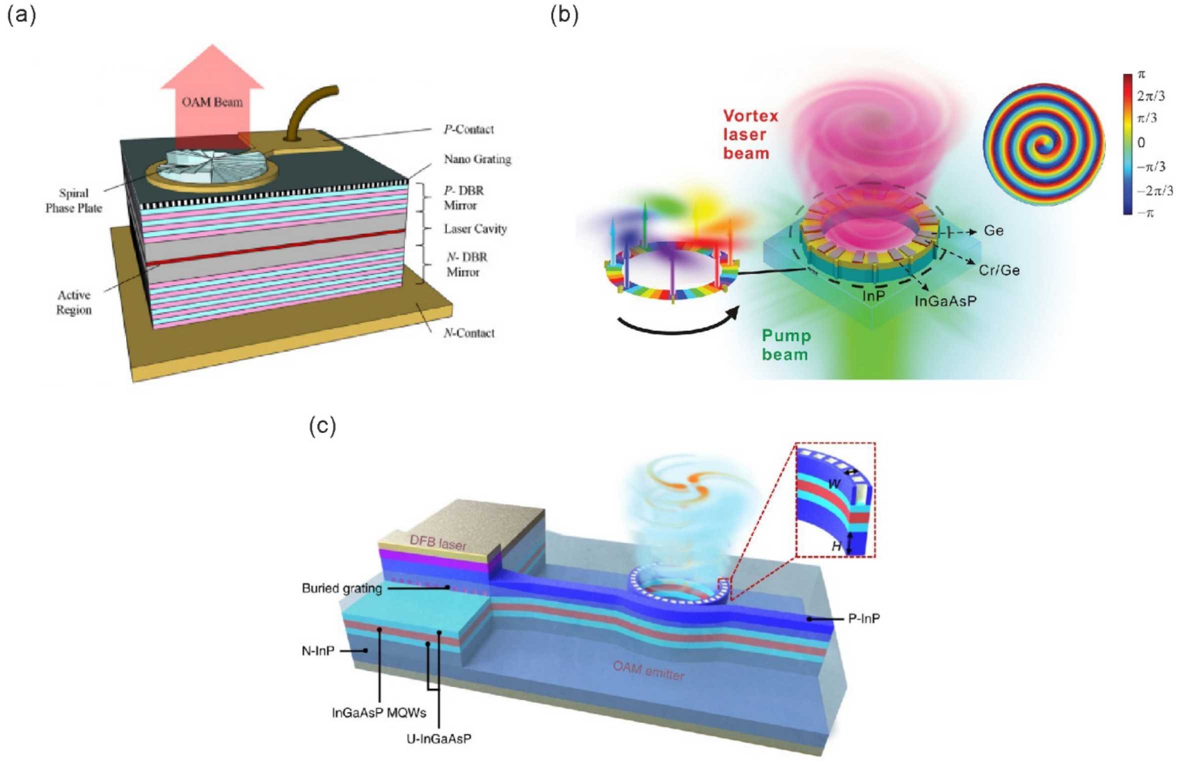

Figure 2.12 Integrated optical vortex beam lasers. (a) Schematic of the vertical-cavity surface-emitting laser with an integrated spiral phase plate at the output port [97]. (b) Schematic of an OAM microlaser on an InGaAsP/InP platform. The on-top Ge and Cr/Ge introduce different loss and gain modulations. So they form an exceptional point operation that allows for one-way light circulation in the microring cavity. It emits a vortex laser beam under optical pumping [98]. (c) Integrated OAM laser with shallow-etched distributed feedback laser and deeply etched vortex emitter on InGaAsP/InP wafer [99]. The OAM laser is electrically pumped.

The optical vortex beams generated by the mentioned integrated lasers remain static. The tunability of OAM modes is desired for the sensing and information-processing systems. In general, the switching of OAM generated by free-space bulk optical components is around a millisecond [100]. Fast electrical switching of OAM modes was proposed using ultra-compact integrated vortex emitters [101]. The emitter is tuned using electrically contacted thermo-optical control. On-off-keying and OAM modes switching are achieved at rates of 10 µs and 20 µs, respectively. Recently, ultrafast control of vortex microlasers was demonstrated, as shown in Figure 2.13(a) [102]. The vortex microlaser is based on a perovskite metasurface. By exploiting both mode symmetry and far-field properties, the vortex beam lasing can be switched to linearly polarized beam lasing with a switching time of 1 to 1.5 picoseconds. Dynamic tuning of TC has also been achieved based on a vortex microlaser, as shown in Figure 2.13(b) [103]. Using the properties of total momentum conservation, spin-orbit interaction, and optical non-Hermitian symmetry breaking, an OAM vortex microlaser provides variable TC at a single telecommunication wavelength. Tunable OAM states ranging in l=-2, -1, 0 ,1 ,2 was demonstrated. Apart from the tunable TC, tailorable chirality of the OAM (clockwise or counterclockwise vortices) is also highly desired. An OAM laser with optically controllable chirality of the emission has been proposed [104]. The device is based on optically breaking time-reversal symmetry in a semiconductor microcavity. By exploiting the spin-orbit coupling of photons confined in planar microcavities, the chirality of the emitted vortex beam can be controlled by tunning the polarization of the pump.

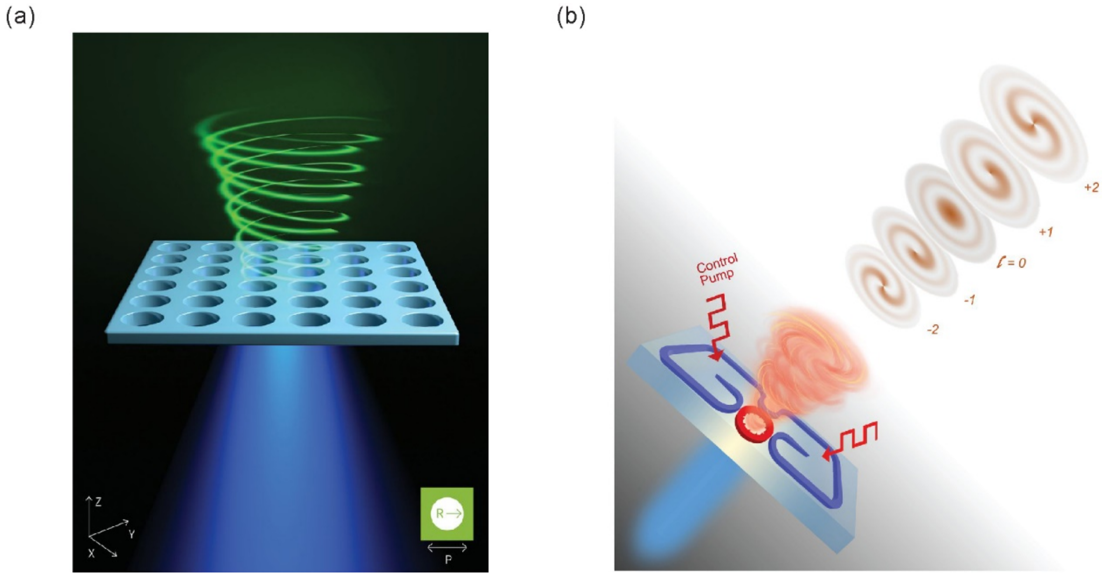

Figure 2.13 Generation of tunable OAM modes. (a) Schematic of the designed perovskite metasurface for ultrafast controlling vortex beams. The metasurface is pumped by blue laser light, producing a green vortex beam in the vertical direction [102]. (b) Schematic of non–Hermitian controlled vortex microlaser. It can emit a vortex beam with a tunable topological charge at a single telecommunication wavelength [103].

2.4 Vector vortex beams

In the previous sections, applications and generation methods of OAM of vortex beams have been described. The SOP provides another degree of freedom for applications based on the optical vortex beam. The solution to the paraxial wave equation in section 2.1 has a spatially homogeneous state of polarization, such as linear, elliptical and circular polarizations [105]. The polarization pattern does not depend on the spatial location in the vortex beam. A vortex beam can possess SOPs varying with the location with respect to the beam axis. Such a vortex beam is called the vector vortex (VV) beam [3, 10, 105]. It was discovered that a radial polarized VV beam exhibits an intriguing property of tight focusing [106]. Since then, there has been an increasing interest in studying VV beams. The spatially inhomogeneous polarization of vector vortex beam has benefited optical sensing. The tight focusing property of a radially polarized beam can be used for determining the three-dimensional orientation of a molecular [107] and for high-precision positioning sensing [108]. Recently, VV beams have been used to determine a moving particle's velocity and motion direction without using an additional reference light [109]. The polarization degree of freedom can be further explored to monitor universal motion vectors in the natural world. Besides the sensing applications, microscopy techniques have utilized the tight focusing property to enhance the resolution limited by the diffractive property of light [110, 111]. Optical trapping efficiency [112, 113], laser machining efficiency [114, 115] and optical communication's transmission date rate and stability [116-118] can be improved by the unique polarization states of VV beams.

The VV beams can be generated as coaxial superpositions of scalar fields with orthogonal polarization states in the LG basis as [119]

$$U(\boldsymbol{r}) = LG_{p_1}^{l_1} e^{i\delta_1} \hat{\boldsymbol{e}}_{\boldsymbol{L}} + LG_{p_2}^{l_2} e^{i\delta_2} \hat{\mathbf{e}}_{\boldsymbol{R}} \tag{2.10}$$

where the unitary vectors $\hat{\boldsymbol{e}}_{\boldsymbol{L}}$ and $\hat{\boldsymbol{e}}_{\boldsymbol{R}}$ represent the left and right circular polarization states with corresponding amplitudes $LG_{p_1}^{l_1}$ and $LG_{p_2}^{l_2}$, respectively. δ represents the wave phase.

Figure 2.14 shows the vector beams produced based on Eq. (2.10). The parameters are l_1=-1, l_2=1, p_1=0, p_2=0, δ_1=0, δ_2=0 in Figure 2.14(a), l_1=-1, l_2=1, p_1=0, p_2=0, δ_1=π, δ_2=0 in Figure 2.14(b) and l_1=-2, l_2=2, p_1=0, p_2=0, δ_1=0, δ_2=0 in Figure 2.14(c). The distribution of field intensity is shown in colour maps. All the intensity distributions are doughnut-shaped because the LG modes are the basis for generating the desired vector beams. The polarization is presented with white lines. In each plot, the polarization states vary across the beam profile. It can be observed that the different sets of the parameters (l_1, l_2, p_1, p_2, δ_1 and δ_2) lead to different space-variant polarization states. As the combination of the parameters is infinite, the number of vector vortex beams formed using Eq. (2.10) would be infinite.

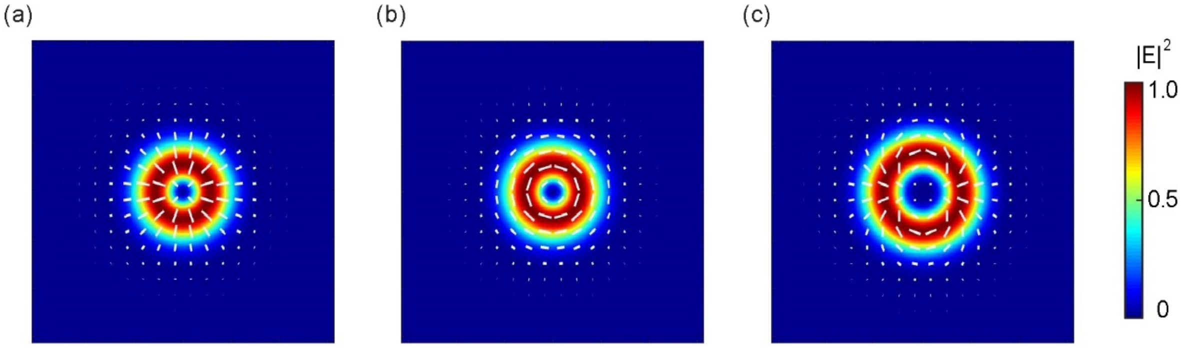

Figure 2.14 Distributions of intensity and polarization states of vector vortex beams generated with the parameters (a) l_1=-1, l_2=1, p_1=0, p_2=0, δ_1=0, δ_2=0. (b) l_1=-1, l_2=1, p_1=0, p_2=0, δ_1=π, δ_2=0 and (c) l_1=-2, l_2=2, p_1=0, p_2=0, δ_1=0, δ_2=0.

Figure 2.14(a)(b) show that SOPs follow radial and azimuthal direction at any point on the beam, respectively. They are named as the radial and azimuthal polarization states, respectively. The two polarization states are two special examples of the well-known cylindrical vector beams (CVBs), whose state of polarization possesses rotational symmetry [10].

Poincaré, in 1892 proposed to describe a polarization state of light as a point on the surface of a unit sphere known as the Poincaré sphere. The geometry characterization provides a simple way to represent any polarization state. However, the Poincaré sphere is limited to the homogeneous plane wave. In 2011, a higher-order Poincaré (HOP) sphere was proposed to describe the spatially inhomogeneous SOPs of VV beams [120]. This geometric representation provides an intuitive interpretation of SOPs and is useful for complex polarization problems. The north and south poles of the HOP sphere represent the opposite spin states and orbital states. Equatorial points represent linearly polarized VV beams. Intermediate points between the poles and equator represent the elliptically polarized VV beam. Any state on the HOP sphere can be realized by a superposition of any two orthogonal states. A mathematical expression that describes all the states of polarization as a two dimensional Jones vector for a given l value can be given by [120]

$$\left|\psi_l\right\rangle = \psi_L^l \left|L_l\right\rangle + \psi_R^l \left|R_l\right\rangle \tag{2.11}$$

where ψ_L^l is the coefficient for the left circular polarized vortex beam, which has an amplitude of $\left|\psi_L^l\right|$ and a phase of arg(ψ_L^l). ψ_R^l is that for the right circular polarized vortex beam. L_l And R_l are the orthogonal circular polarization basis, which can be expressed as

$$\left|L_l\right\rangle = \exp(-il\phi)(\boldsymbol{x} + i\boldsymbol{y}) / \sqrt{2} \tag{2.12}$$

$$\left|R_l\right\rangle = \exp(il\phi)(\boldsymbol{x} - i\boldsymbol{y}) / \sqrt{2} \tag{2.13}$$

The SOP described by Eq. (2.11) can be mapped onto the surface of a HOP sphere through the Stokes parameters (SPs) as the sphere’s Cartesian coordinates. Normalized high-order SPs in the circular basis are given by

$$S_0^l = \left|\psi_R^l\right|^2 + \left|\psi_L^l\right|^2 \tag{2.14}$$

$$S_1^l = 2\,\mathrm{Re}\left[(\psi_L^l)^*(\psi_R^l)\right] = 2\left|\psi_R^l\right|\left|\psi_L^l\right|\cos\phi \tag{2.15}$$

$$S_2^l = 2\,\mathrm{Im}\left[(\psi_L^l)^*(\psi_R^l)\right] = 2\left|\psi_R^l\right|\left|\psi_L^l\right|\sin\phi \tag{2.16}$$

$$S_3^l = \left|\psi_R^l\right|^2 - \left|\psi_L^l\right|^2 \tag{2.17}$$

where $\phi = \arg\left(\psi_R^l\right) - \arg\left(\psi_L^l\right)$ and $\left(S_0^l\right)^2 = \left(S_1^l\right)^2 + \left(S_2^l\right)^2 + \left(S_3^l\right)^2$. The total intensity S_0^l is set as $S_0^l = 1$ for a fully polarized beam. The value of l represents the order of the HOP sphere.

Figure 2.15 illustrates the +1st-order HOP sphere when l=+1. The handednesses of the optical vortex and circular polarization at each pole are opposite, according to Eqs (2.12)(2.13). The equator presents the CVBs, including the radial and azimuthal polarization states. Intermediate points between the poles and the equator represent elliptically polarized CVBs.

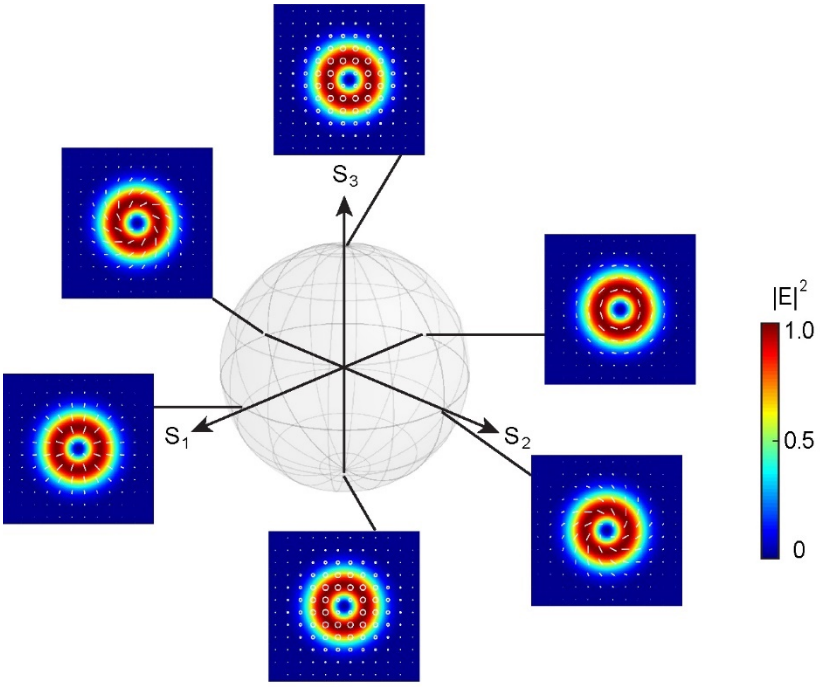

Figure 2.15 Higher-order Poincaré sphere representation for l=+1.

Figure 2.16 illustrates the -1st-order HOP sphere when l= -1. The handednesses of the optical vortex and circular polarization at each pole are the same, according to Eqs (2.12)(2.13). The equator presents the π-vector beams, including the π-radial and π-azimuthal polarization states. Intermediate points between the poles and the equator represent elliptically polarized π-vector beams.

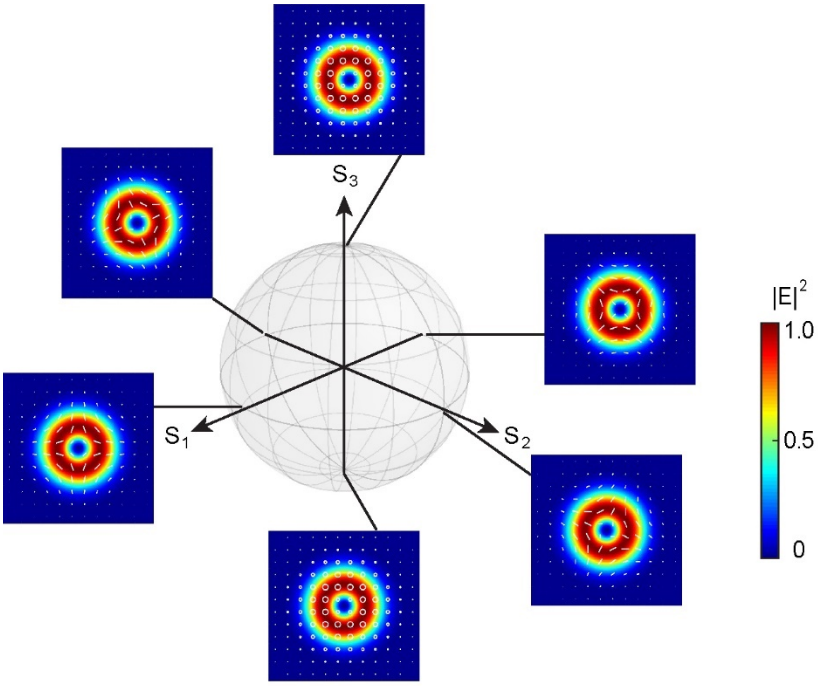

Figure 2.16 Higher-order Poincaré sphere representation for l=-1.

According to Eqs. (2.11)(2.12)(2.13), the modes located at the poles of a HOP sphere carry the same TC differing only in their signs. When the TCs are different in Eqs. (2.12)(2.13), Eq. (2.11) will represent a hybrid-order Poincaré sphere [121]. This sphere is a more general form that can present complex polarization states of VV beams.

2.5 Generation methods

Various approaches have been reported to create VV beams. They can be classified into intracavity and extracavity methods. The former involves laser resonators or optical fibres. The extracavity methods include interferometric methods, direction conversion and photonic chips.

2.5.1 Intracavity methods

2.5.1.1 Laser resonators

The intracavity generation technique is based on a customized intracavity device to force the laser to oscillate in the desired polarization modes [10]. A calcite crystal was used inside a laser to generate azimuthally polarized light [122]. This element has different refractive indices for the azimuthally and radially polarized light, causing differences in the transverse dimensions of the two modes. A conical Brewster prism [123] was applied for the generation of a radially polarized laser beam. The radial polarized light will pass through the prism without loss, while the azimuthally polarized light will suffer a significant loss. Figure 2.17(a) shows a schematic of the laser. The polarization selection devices are based on bulk optics, which increases the complexity of the laser systems. In order to achieve a simpler and compact laser design for CVBs generation, mirrors for polarization selection were fabricated based on micro-nano fabrication technology [124-126]. Figure 2.17(b) shows the laser configuration.

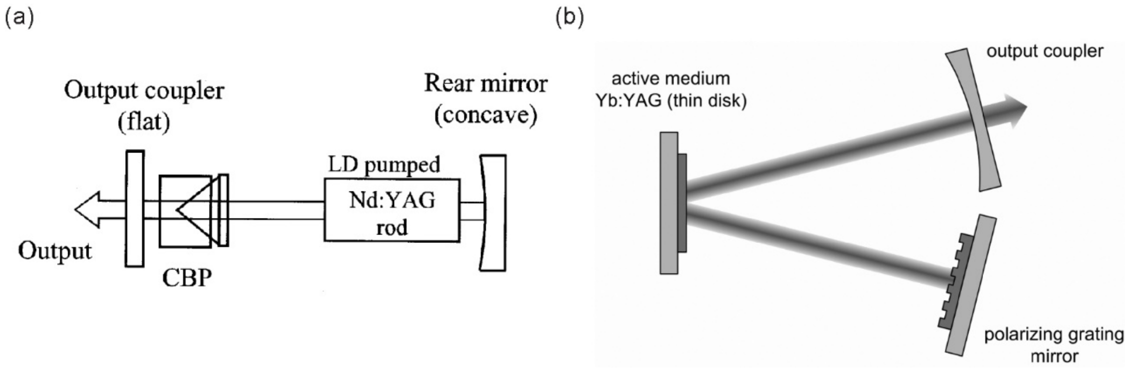

Figure 2.17 Generation of vector vortex beams with customized intracavity devices. (a) Illustration of a laser that generates radially polarized beam by using a conical Brewster prism (CBP) [123]. (b) A thin-disk laser resonator is used to generate radially polarized radiation based on a multilayer polarizing grating mirror [124].

The methods mentioned above use customized and additional elements, which increase the complexity of the lasers. A laser was demonstrated to produce radially or azimuthally polarized beams without using special optical elements. This method is based on the different focusing between radially and azimuthally polarized light in thermally stressed isotropic laser rods [127, 128]. Later, an ultimately simple method for the generation of the radially polarized laser beam was proposed. Figure 2.18 shows the schematic of the laser resonator. A c-cut Nd: YVO_4 crystal was used as the laser medium. This crystal possesses cylindrically symmetric birefringence that can distinguish a radially polarized beam from an azimuthally polarized one. By simply adjusting the distance between two cavity mirrors, only the extraordinary ray became stable for the oscillation, resulting in the generation of a radially polarized beam without using any additional optical element [129].

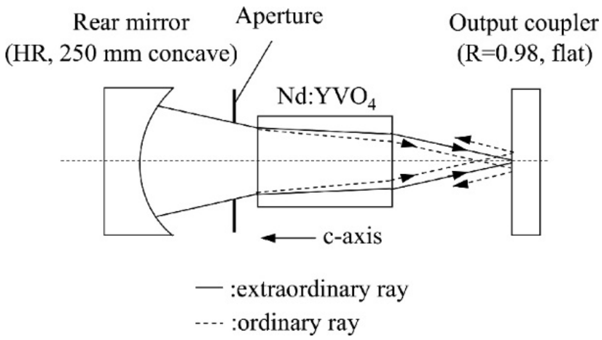

Figure 2.18 Schematic of a simple laser resonator for generating a radially polarized beam. It is shown that the ordinary and extraordinary rays take different optical paths in the Nd: YVO$_4$ rod because of the different refractive indices [129].

The lasers mentioned above can only generate azimuthal or radial polarization states depending on the customized designs. The two polarization states are two specific points on the equator of a HOP sphere, according to section 2.4. The laser to create an arbitrary HOP sphere beam on demand is highly desired. Recently, the controlled generation of HOP sphere beams from a laser was demonstrated [130]. Figure 2.19 shows the schematic of the HOP sphere laser. The desired polarization states are generated by the superposition of LHCP and RHCP vortex beams. The intensity ratio and phase contrast between the two uniform polarized vortex beams are controlled by the relative angles between the wave-plate and q-plate. The wave-plate is used to select a pure SAM state by transmitting linearly polarized light. The q-plate acts as a SAM-OAM converter. By exploiting different q-plates, polarization states on the +1st- and +10th-order Poincaré spheres were demonstrated.

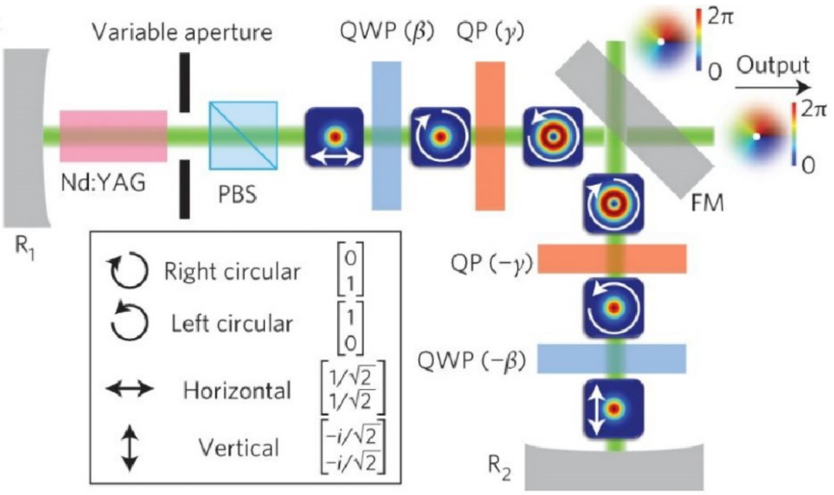

Figure 2.19 Illustration of a laser for the controlled generation of higher-order Poincaré sphere beams by the intracavity coupling of SAM to OAM [130].

2.5.1.2 Optical fibres

Among the active generation methods, fibre lasers have attracted much attention considering their potential advantages in high efficiency, high power, flexibility and compactness [105]. For a fibre laser, the critical point is to find an appropriate mechanism to control and select the desired vectorial mode in the laser cavity. Intracavity devices such as dual conical prism [131], spatial variable retarder [132] and calcite crystal [133] have been utilized to select the desired polarization. However, these devices are based on bulk optical elements, increasing the complexity of the systems. A fully integrated all-fibre laser generating CVBs has been demonstrated [134, 135]. Figure 2.20 shows the schematic of the design of the fibre laser. A lateral offset splicing is used in the laser cavity for efficient coupling from the fundamental mode to the desired high-order cylindrically polarized modes. Radially and azimuthally polarized modes can be switched by simply adjusting the polarization controller built in the fibre laser cavity.

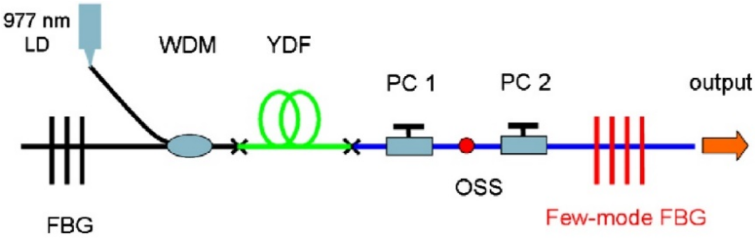

Figure 2.20 Schematic illustration of the fibre laser for generation cylindrical vector beams based on an offset splicing spot (OSS) [134].

Apart from using the lateral offset splicing spot, desired polarization states can be converted within fibres by using a mode-selective converter [136], photonic lantern [137] and fibre grating [138]. However, those methods can only generate specific cylindrical vector modes. It is desirable to produce controllable polarization states on a HOP sphere. Recently, an all-fibre system was proposed to generate arbitrary VV beams on the FOPS [139]. Figure 2.21 shows the experimental setup. The system cascades a photonic lantern and a two-segment few-mode fibre with different stresses. During the process of mode switching, the states of the two-segment few-mode fibres are fixed. All CV modes on FOPS can be generated by adjusting the polarization of the fundamental mode, which implies that this system has the potential for fast switching with an electronic polarization controller.

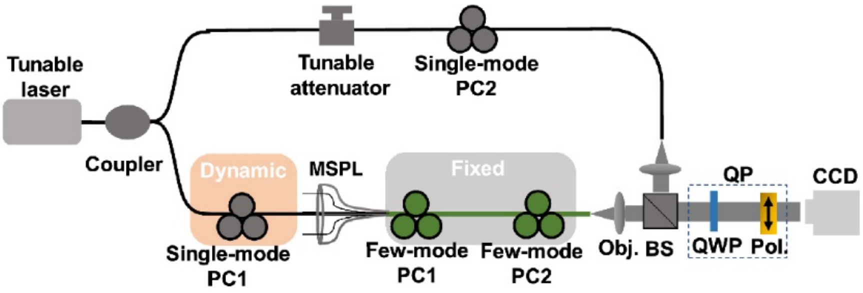

Figure 2.21 Experimental setup to generate arbitrary cylindrical vector beams on the first-order Poincaré sphere in fibre [139].

2.5.2 Extracavity methods

Extracavity methods have been used to convert the homogeneous polarization into spatially inhomogeneous polarization based on the devices with spatially variant polarization properties. The methods contain the interferometric combination of orthogonally polarized beams, direct conversion using polarization-sensitive optical elements and photonic chips.

2.5.2.1 Interferometric methods

Interferometric methods generate VV beams based on the combination of orthogonally polarized beams. Mach-Zehnder interferometer configurations have been exploited to produce radially polarized beams [140]. Orthogonally polarized beams with tailored intensity and phase profiles are linearly combined. The generated polarization state cannot be easily tailored due to the customized spiral phase delay plate. A more flexible way is to use an SLM to generate various VV beams. A Wollaston prism splits an incoming laser beam into two orthogonally polarized beams. The two beams are modulated by binary holograms displayed at the SLM and were then superposed in one diffraction direction. Azimuthally and radially polarized beams have been produced [141]. However, the diffraction efficiency is low due to the binary phase structures. A nematic liquid crystal SLM was introduced to increase mode conversion efficiency [142]. Figure 2.22 shows the schematic of the setup. Two incident beams are diffracted from two adjacent holograms that are displayed at the same SLM. It provides great flexibility to control the spatial amplitude distribution and phase of the diffracted beams. The versatility of this new approach allows the creation of arbitrary vector beams with high diffraction efficiency.

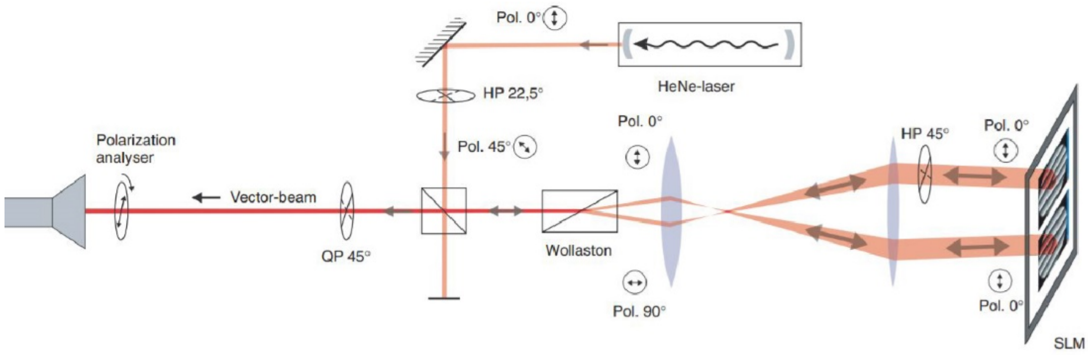

Figure 2.22 Interferometric method generates arbitrary vector beam modes by diffracting a Gaussian laser beam from a spatial light modulator [142].

Interferometric approaches have also been proposed to generate arbitrary cylindrical vector beams on the HOP sphere [143]. Two orthogonal circular polarized lights with opposite TCs are collinearly superposed. Each light's amplitude and phase factors can be modified by using cascaded Glan laser polarizers and half-wave plates, respectively. The mentioned interferometric methods can only produce a single VV beam at a time. Recently, simultaneous generation of multiple vector beams using a single SLM has been demonstrated [144], as shown in Figure 2.23. On the SLM, a set of holograms were multiplexed to generate two sets of scalar fields. One set of fields travels along with path A, and another travels along path B. The phase and amplitude, and shape of each set of fields can be digitally manipulated independently. Multiple vector beams can be produced simultaneously once the two sets of fields are combined. Simultaneous generation of sixteen CVBs has been demonstrated.

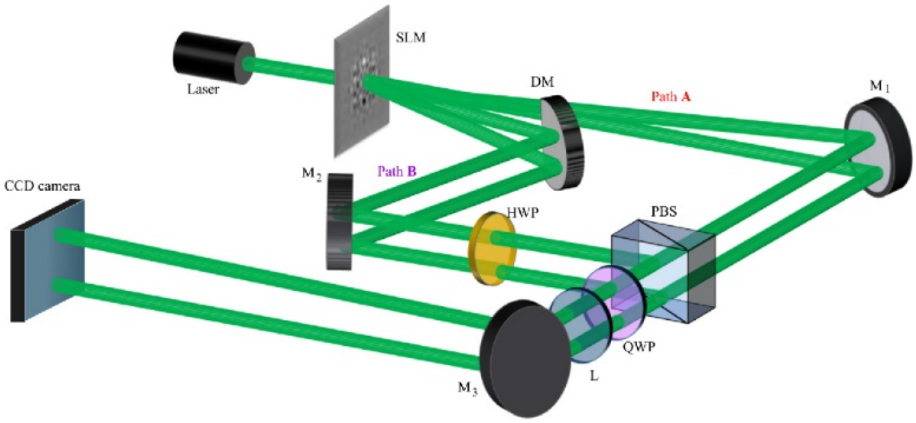

Figure 2.23 Schematic representation of an interferometric method to generate multiple cylindrical vector beams based on a spatial light modulator [144].

A compact and simple VV beam generator based on the interferometric method is desired, which possesses advantages of miniaturization and reliability. A generator has been proposed by integrating commonly used optical elements [145]. It can convert the input beam carrying OAM into a VV beam. However, a lot of optical elements are required by this device, which increases the complexity of the generator. Recently, a simple and compact method has been proposed based on a two-element interferometer [146]. A beam displacer and a cube beamsplitter were utilized. The device can transform a homogeneously polarized vortex beam into a cylindrical vector beam.

2.5.2.2 Direction conversion

The direct conversion is based on vector beams generators which can convert a Gaussian beam to a vector beam. An azimuthally polarized beam was converted from a circularly polarized light based on space-variant polarization control. The control is achieved using subwavelength metal stripe gratings with its local subwavelength groove orientation continuously varying [147]. However, this device lacks the flexibility to produce different VV beams. Liquid crystals that can be dynamically controlled have been exploited to generate radially and azimuthally polarized beams [148]. In 2006, q-plates were proposed based on birefringent liquid crystals. The plates have an azimuthal pattern of the liquid crystal molecular director around a central point. The polarization pattern of the output beam can be easily changed by adjusting the polarization state of the incident light [77]. Q-plates have been utilized extensively due to their simple operation for generating and controlling VV beams [149, 150]. Figure 2.24 shows a setup to generate tunable VV beams by a q-plate [151]. The polarization of the generated VV beams depends on the input laser beam’s polarization states which can be controlled by rotating the plates in the QHQH set. The TC of the q-plate can be electrically controlled.

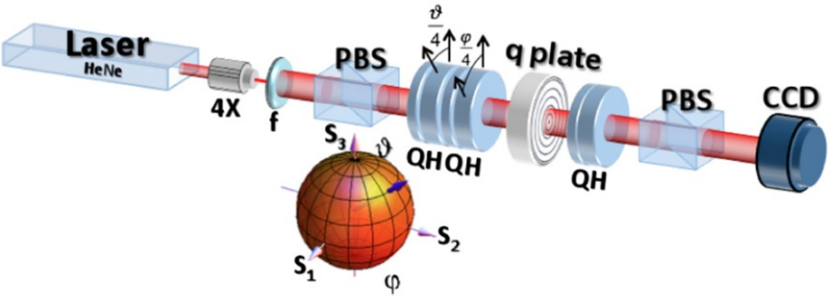

Figure 2.24 Setup to generate and analyze different polarization generated by a q-plate. The polarization state of the input laser beam was prepared by rotating the two half-wave plates in the QHQH set [151].

Alternative to the liquid crystal-based q-plate, compact metasurfaces have been utilized to achieve the direct generation of VV beams. A metasurface has been proposed to generate radially and azimuthally polarized beams [152]. Switching between the two polarization states can be achieved by controlling the handedness of incident circular polarization. The device is fabricated by femtosecond laser writing of self-assembled nanostructures in silica glass. Dielectric metasurfaces with silicon elliptical posts with different sizes and orientations have also been demonstrated to generate VV beams. Generation and focusing of radially and azimuthally polarized beams can be performed based on a single device [153]. The vortex beams generated by the mentioned metasurfaces are limited. Two cascaded metasurfaces are proposed to generate any cylindrical VV beams. Figure 2.25 shows the experimental setup. The first metasurface is used to switch the sign of the TC associated to vortex beams by controlling the handedness of the incident polarization. The second metasurface can manipulate the local polarization orientation of the vector beam [154].

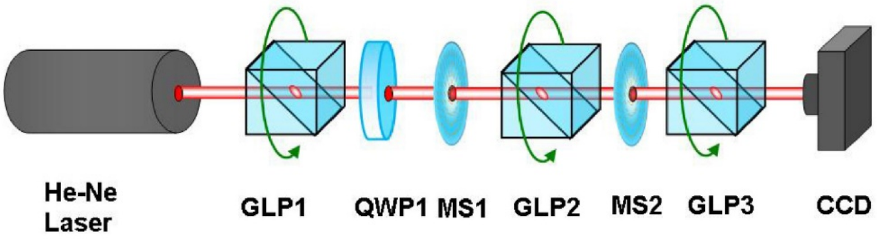

Figure 2.25 Experimental setup for generating arbitrary CVV beams based on two cascaded metasurfaces [154].

The applications of metasurfaces have also been extended for generating broadband VV beams. Nanostructured holograms have been proposed to generate radially polarized vortex beams in a wavelength range from 633 to 850 nm. The device can be viewed as a hologram with each of its apertures filled with nanoscale structures only to transmit the desired state of polarization [155]. Another metasurface was demonstrated to generate vector vortex beams from 1000 to 2500 nm. It consists of two concentric rings in gold film, and each ring is composed of subwavelength rectangular apertures serving as a localized spatial polarizer. Generation of VV beams with polarization order varying from -3 to +3 has been demonstrated [156].

2.5.2.3 Photonic chips

Integrated photonic devices with advantages of compactness and reliability are attracting much attention for generating VV beams. The optical vortex beam emitter [94] and microlasers [98] have been explored to generate radially polarized vortex beams. The grating elements are located at the sidewall of the microring and can only interact with the radial polarized component in the microring. Apart from the gratings at the sidewall, azimuthally distributed grating on the ring waveguide is also proposed to generate radial polarized OAM beams [157]. However, all the generated polarization states cannot be changed. The tunability of polarization states has been studied by using a microring-based vortex beam emitter [158]. By changing the geometry of the ring waveguide, the spin-orbit interaction can be engineered. As a result, the power ratio between the left and right circularly polarized beams can be tuned. Recently, antenna-decorated microdisk resonators have been proposed to generate OAM beams with a pure circular polarization state. The design is shown in Figure 2.26(a) [159]. The plasmonic antennas emit both the LHCP and RHCP beams. By setting the antennas to be V or Λ shapes, pure left- or right-handed polarization can be generated.

The polarization states generated by the mentioned integrated approaches are not adjustable once the devices are fabricated. An integrated device was demonstrated to generate switchable radially and azimuthally polarized vortex beams. The device is shown in Figure 2.26(b) [160]. It contains a microring resonator with shallow-etched periodic angular grating placed on top of the ring waveguide. The radiated vortex beam's polarization is determined by the SOP of the local optical field being scattered at each grating element. Switching the injected light from the TE to TM mode can change the radially polarized vortex beam to the azimuthally polarized beam. The wavelengths of the generated radially and azimuthally polarized VV beams are different due to the different resonant wavelengths for TE and TM modes in the microring. The radial and azimuthal polarization are only two specific points on a HOP sphere. So far, there is still no work to generate HOP sphere beams via a single integrated device.

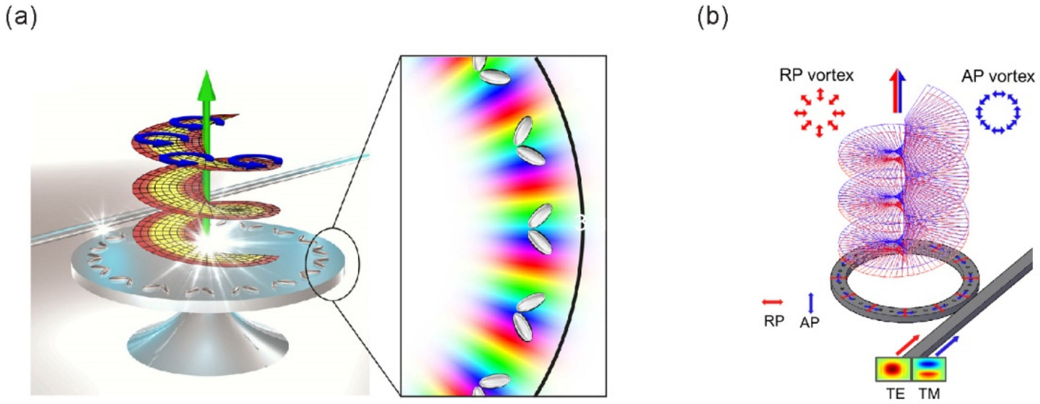

Figure 2.26 Integrated vector vortex beam emitters. (a) A microdisk resonator is decorated with antennas to generate OAM beams with a pure circular polarization state [159]. (b) A microring resonator with shallow-etched periodic angular grating placed on top of the ring waveguide to generate switchable radially and azimuthally polarized vortex beams [160].

Much progress has been made in the emission of VV beams from a chip surface into free space. A VV beam emitter embedded in a photonic chip was studied, as shown in Figure 2.27. This device was fabricated by using femtosecond laser direct writing. This device consists of a coupled structure, including a single-mode waveguide and a doughnut-shaped waveguide. Gaussian beams in the single-mode waveguide are evanescently coupled to the adjacent OAM waveguide and converted into VV beams. The generated VV beam inside the device is useful for further transmission, manipulation without any additional interconnection [161].

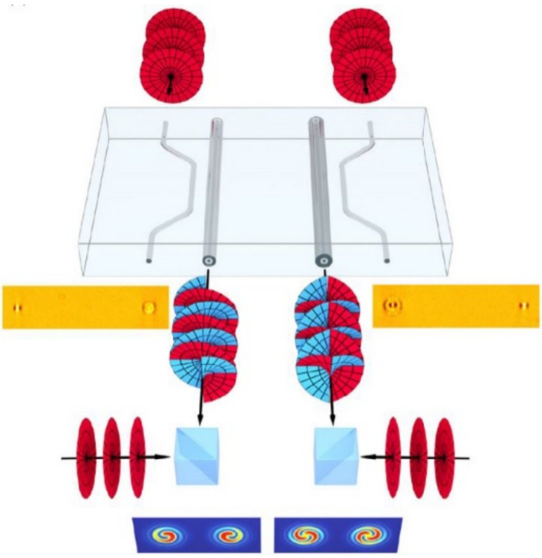

Figure 2.27 A vector vortex beam emitter embedded in a photonic chip. The device, consisting of a standard single-mode waveguide and an OAM waveguide, is employed to generate different order vortex beams based on phase matching [161].

2.6 Conclusion

In this chapter, the OAM and SOP of optical vortex beams are described. The two properties of an optical vortex beam have been exploited for various applications, including optical sensing, optical communication, manipulation and imaging. Although numerous applications have benefited from the vortex beams, the development of this field is advancing more potential applications. For example, vortex beams could be explored for improving the performance of current LiDAR technologies. The unique properties of vortex beams, unbounded OAM states and spatially variant SOPs, could provide two new degrees of freedom for obtaining more object's information and enhancing resolution [4, 26, 109]. Creating the desired vortex beam is the first crucial step for these fascinating applications. Various methods for generating desired OAM and polarization states have been proposed, including intracavity and extracavity techniques. Each technique is developed with the desired features of tunability, compactness, simplicity. Particularly, the integrated photonic devices are attracting increasing attention with the advantage of compactness and reliability.

For the OAM generation, current integrated devices mainly radiate light in the near-infrared regime. The spectral range is restricted by the transmission window of the integrated photonic platforms. THz waves, with unique properties such as low photon energy and high penetrability, can be used in a wide range of applications, such as sensing, imagining and communication [162-165]. Recently, LiDAR systems using THz waves have been proposed to work in dust clouds and atmospheric turbulence where the absorption of infrared light is high [166]. However, an integrated

THz light source that allows for both the generation and tuning of the OAM is not yet available. For the generation of the VV beam, current integrated devices can only generate specific points on a HOP sphere. The controlled arbitrary HOP sphere beams would improve the performance of communications and objects' motion sensing [109, 119]. However, there is still no integrated device that can generate arbitrary HOP sphere beams. The following chapters will describe our proposed solutions to address the challenges of the integrated vortex beam emitters.

Chapter 3 Integrated vortex beam emitter in the THz frequency range

In the previous chapter, OAM and its generating methods have been described. Integrated OAM generators have attracted increasing attention. These compact devices can generate OAM at the stage of light emission, eliminating the need for any subsequent light-conversion element. However, most of these emitters radiate light in the near-infrared regime. There is still no integrated THz vortex beam emitter that allows for both the generation and tuning of OAM. Recent advances in THz sensing and wireless communication have made the development of a compact, surface-emitting THz vortex beam source highly desirable [165-168]. For example, the integrated THz vortex beam emitter providing tunable OAM modes can be combined with LiDAR systems to improve the spatial resolution [26].

In this chapter, an integrated THz vortex beam emitter is proposed. The design is based on a $LiNbO_3$ microring, a Si microdisk, and an Au second-order top grating. Two infrared pumps in the $LiNbO_3$ microring are converted into a freely propagating THz beam via a difference-frequency generation (DFG) process. The emitted THz beam carries a TC that can be tuned by changing the wavelengths of the incident light. Three devices are evaluated in a test frequency range from 9 THz to 13.5 THz, and the TC can vary from −2 to 4. Most results in this chapter have been published by the journal “APL Photonics”.

3.1 Introduction

3.1.1 THz generation based on the difference-frequency generation process

Before introducing the integrated THz vortex source based on a DFG process, the theory of DFG and its integrated implementations are covered first. A simple illustration of DFG is shown in Figure 3.1 [169].

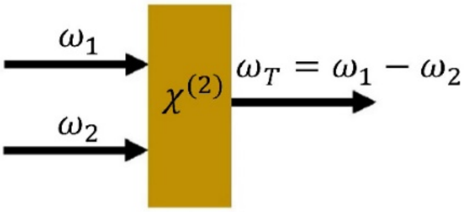

Figure 3.1 Schematic diagram of the difference frequency generation process.

DFG process is a second-order nonlinear optical process based on a nonlinear crystal. The following part shows the derivation of the expression of a generated THz wave based on DFG [169, 170]. The optical input field consists of two distinct frequency components, which can be expressed as

$$\begin{aligned} E(z,t) &= E_1 e^{-i\omega_1 t} + E_2 e^{-i\omega_2 t} + c.c. \\ &= A_1 e^{(ik_1 z - i\omega_1 t)} + A_2^{(ik_2 z - i\omega_2 t)} + c.c. \end{aligned} \tag{3.1}$$

where $A_{1,2}$ are amplitudes of optical input fields, $k_{1,2}$ are the wavenumbers, $\omega_{1,2}$ are the angular frequencies of the two input fields, ‘c.c.’ denotes complex conjugate.

The two laser fields can cause the nonlinear polarization of the medium. For a fixed propagation direction, the amplitude of the nonlinear polarization describing the DFG process can be expressed as

$$\begin{aligned} P^{(2)}(z,t) &= 2\varepsilon_0 \chi^{(2)} E_1 E_2^* e^{-i(\omega_1-\omega_2)t} + c.c. \\ &= 2\varepsilon_0 \chi^{(2)} A_1 A_2^* e^{i(k_1-k_2)z} e^{-i(\omega_1-\omega_2)t} + c.c. \end{aligned} \tag{3.2}$$

where ε_0 is the permittivity of free space, $\chi^{(2)}$ is the second-order nonlinear optical susceptibility. The $*$ denotes the conjugated complex value.

The time-varying polarization acts as a source for generating the desired THz wave. The wave equation for the DFG process can be deduced from Maxwell’s equations which are

$$\nabla \cdot \boldsymbol{D} = \rho \tag{3.3}$$

$$\nabla \cdot \boldsymbol{B} = 0 \tag{3.4}$$

$$\nabla \times \boldsymbol{E} = -\frac{\partial \boldsymbol{B}}{\partial t} \tag{3.5}$$

$$\nabla \times \boldsymbol{H} = \boldsymbol{J} + \frac{\partial \boldsymbol{D}}{\partial t} \tag{3.6}$$

where the electric quantities $\boldsymbol{D}$ and $\boldsymbol{E}$ are the electric displacement field and the electric field, respectively. $\boldsymbol{B}$ and $\boldsymbol{H}$ are the magnetic flux density and the magnetic field, respectively. ρ is the free charge density, and $\boldsymbol{J}$ is the free current density.

We assume that the material is nonmagnetic, so

$$\boldsymbol{B} = \mu_0 \boldsymbol{H} \tag{3.7}$$

where μ_0 is the vacuum permeability.

Assuming there is no free charges and no free currents in the nonmagnetic material, we take the curl of $\nabla \times \boldsymbol{E}$ and obtain the equation

$$\nabla^2 \boldsymbol{E} + \mu_0 \frac{\partial^2 \boldsymbol{D}}{\partial t^2} = 0 \tag{3.8}$$

D and ***E*** are related by

$$\boldsymbol{D} = \varepsilon_r \varepsilon_0 \boldsymbol{E} + \boldsymbol{P}^{(2)} \tag{3.9}$$

where ε_r is the relative permittivity of the material. So Eq. (3.8) can be rewritten as

$$\nabla^2 \boldsymbol{E} - \frac{\varepsilon_r}{c^2} \frac{\partial^2 \boldsymbol{E}}{\partial t^2} = \frac{1}{\varepsilon_0 c^2} \frac{\partial^2 \boldsymbol{P}^{(2)}}{\partial t^2} \tag{3.10}$$

where $1/(\varepsilon_0 c^2)$ is used to replace μ_0.

We assume that a linearly polarized THz wave propagates in the z-direction. So Eq. (3.10) can be written as

$$\frac{\partial^2 E_T}{\partial z^2} - \frac{\varepsilon_r}{c^2} \frac{\partial^2 E_T}{\partial t^2} = \frac{1}{\varepsilon_0 c^2} \frac{\partial^2 P^{(2)}}{\partial t^2} \tag{3.11}$$

where $E_T = A_T \exp(ik_T z - i\omega_T t) + c.c.$ is the THz field with $k_T = n_T \omega_T / c.$ $n_T = \sqrt{\varepsilon_r}$ is the refractive index at the THz wavelength.

Eq. (3.11) can be rewritten as

$$\frac{\partial^2 A_T}{\partial z^2} + 2ik_T \frac{\partial A_T}{\partial z} = -\frac{2\chi^{(2)} \omega_T^2}{c^2} A_1 A_2^* e^{i(k_1 - k_2 - k_T)z} \tag{3.12}$$

The amplitude A_T varies slowly, so the first term in Eq. (3.12) can be neglected. The wave equation is reduced to

$$\frac{dA_T}{dz} = \frac{i\chi^{(2)} \omega_T}{n_T c} A_1 A_2^* e^{i\Delta kz} \tag{3.13}$$

where $\Delta k = k_1 - k_2 - k_T$ is the momentum mismatch.

Under the approximation that the nonlinear conversion process does not deplete the pumps, the integration of Eq. (3.13) for a propagation distance *L* is

$$A_T = \frac{i\chi^{(2)}\omega_T}{n_T c} A_1 A_2^* \frac{e^{i\Delta kL}-1}{i\Delta k} \tag{3.14}$$

In order to achieve the miniaturised THz sources based on the DFG process, various nonlinear waveguides such as GaAs/GaP waveguides [171] and $LiNbO_3$ waveguides [172] have been investigated. Figure 3.2 (a) shows a $LiNbO_3$ embedded waveguide structure for THz generation. The pump waveguide consists of a standard Ti-diffused channel waveguide in a $LiNbO_3$ film. The single-mode THz waveguide core is the $LiNbO_3$ film. The cladding layers of the THz waveguide are the quartz substrate and a high-density polyethylene ridge, which also provides lateral confinement. This structure provides a long interaction length and well-confined collinear propagation of pumps and THz waves [172]. In order to achieve better confinement of generated THz, metallic waveguides have been studied [173]. However, the metallic part of waveguides would introduce extra propagation loss for the THz wave. Thus, there would exist a trade-off between modal confinement and propagation loss. Micro-resonators with high-quality factors have been reported for efficient THz generation based on the DFG process. A THz source based on Au/AlAs/GaAs/AlAs/Au microcylinder has been developed [174]. Two near-IR pump modes are excited by InAs quantum dots embedded in a resonator. The tunability of this source is limited. Then, tunable and compact THz emitters were proposed based on nonlinear microring resonators and microdisk resonators. Figure 3.2(b) shows a THz emitter based on a nonlinear microdisk and a THz disk resonator [175, 176]. The nonlinear microdisk is used to confine infrared pumps and generate THz waves. The THz disk resonator is used for confining the generated THz wave. The frequency of generated THz wave is tunable with the input frequencies.

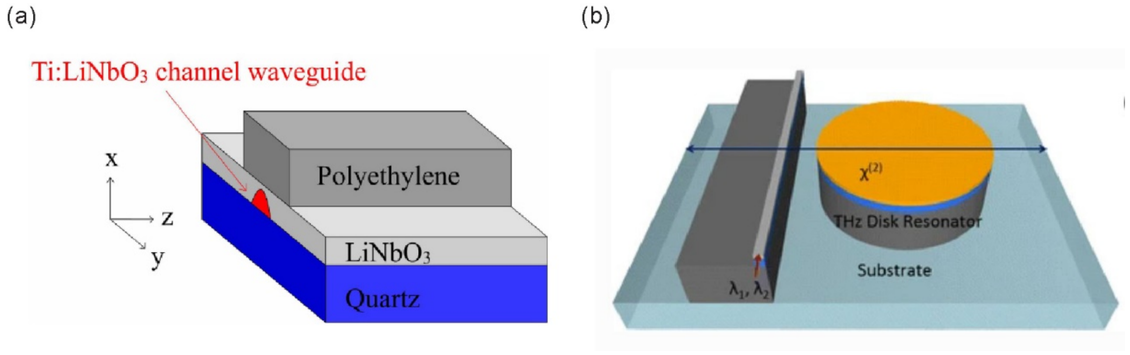

Figure 3.2 Generation of THz waves in waveguides via the DFG process. (a) Schematic of $LiNbO_3$ embedded waveguide for THz generation [172]. (b) Schematic of the THz emitter consisting of nonlinear and THz microdisk resonators [175].

In the mentioned methods, the generated THz waves propagate in the THz waveguides and suffer from the loss due to the absorption and momentum mismatch. This problem can be avoided by extracting the generated THz wave from the whole length of the waveguides. Cherenkov phase-matching scheme was proposed to enable the extraction [177]. Figure 3.3(a) shows the proposed device. Two optical modes are guided in the folded silicon waveguide. DFG process takes place in the nonlinear cladding material and generates THz waves. A high-index lens, placed on top of the waveguide, couples the THz radiation to free space under a defined emission angle. An alternative method to outcouple THz radiation is to use a surface grating on top of the waveguide [178, 179]. Figure 3.3(b) shows a surface-emitting THz source based on intracavity DFG [179]. The THz wave is generated by the two mid-infrared pumps in the nonlinear active region. A second-order grating is utilized for THz emission.

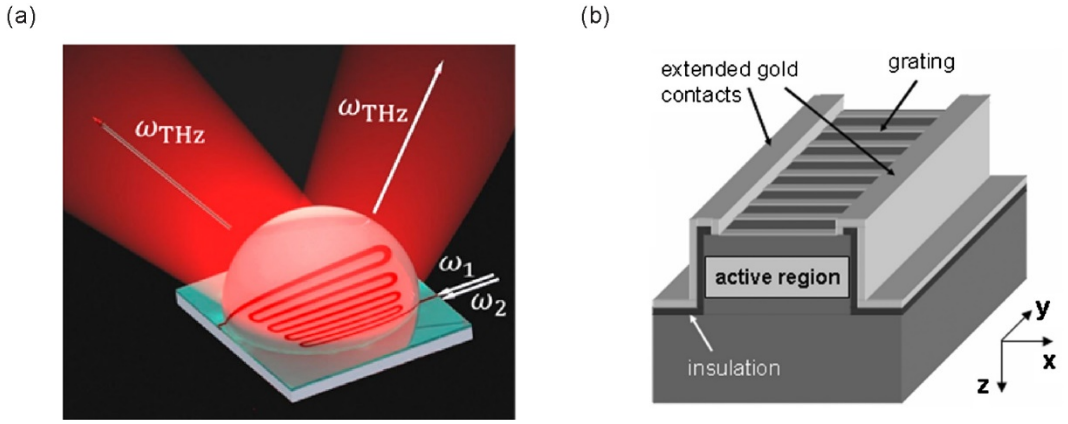

Figure 3.3 Radiating generated THz waves in waveguides. (a) A high-index lens, placed on top of the waveguides, couples the THz radiation to free space under a defined emission angle [177]. (b) Surface-emitting terahertz quantum cascade laser source with gold grating on top [179].

3.1.2 Theory of microring resonator

The integrated THz emitter is based on a nonlinear microring resonator for THz wave generation. The fundamentals of microring will be introduced in this part. A basic configuration of a single microring resonator consists of a microring evanescently coupled to a bus waveguide, as shown in Figure 3.4. When the wave in the loop builds up a round trip phase shift that equals an integer times 2π, the waves interfere constructively, and the microring is in resonance. The condition determining the resonant wavelengths is that the round-trip optical path length is equal to an integral number of wavelengths [180],

$$m\lambda_{res} = n_{eff} 2\pi R \tag{3.15}$$

where *m* is the azimuthal mode number, λ_{res} is the resonant wavelength, *R* is the radius of the ring, and n_{eff} is the effective index of the optical mode in the ring waveguide.

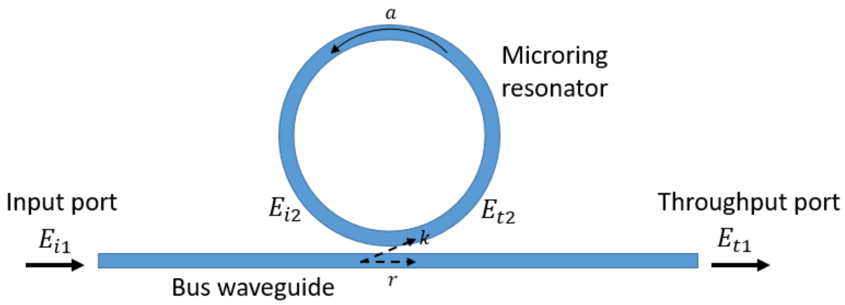

Figure 3.4 Schematic of a single ring resonator with one waveguide.

The transfer function of this microring can be analysed using coupled-mode theory (CMT) either in the time [181-183] or space approach [180, 184-186]. Here we analyse the resonator in the space approach.

We assume that the coupling is lossless, and only a single unidirectional mode in the resonator is excited, and only single polarization is considered. The coupling region, where many important properties of the ring resonator are determined, could be described as a four-port network. The fields at the ports are related as

$$\begin{pmatrix} E_{t1} \\ E_{t2} \end{pmatrix} = \begin{pmatrix} r & k \\ -k^* & r^* \end{pmatrix} \begin{pmatrix} E_{i1} \\ E_{i2} \end{pmatrix} \tag{3.16}$$

where *E* is the amplitude of the electric field, *r* is the effective field transmission coefficient, *k* is the effective field coupling coefficient. * denotes the conjugated complex value.

The coupling region is lossless, therefore

$$\left|k^2\right| + \left|r^2\right| = 1 \tag{3.17}$$

The electric field in the ring could be expressed as

$$E_{i2} = a \cdot e^{j\theta} E_{t2} \tag{3.18}$$

where a and $\theta = \omega L / c$ are both real numbers representing the loss coefficient of the ring and the phase shift per round-trip, respectively. *L* is the circumference of the ring, and *c* is the phase velocity of ring mode ($c = c_0 / n_{eff}$), and ω is the angular frequency.

By combining Eqs. (3.16)-(3.18), we could obtain

$$E_{t1} = E_{i1} \frac{-a + r \cdot e^{-j\theta}}{-ar^* + e^{-j\theta}} \tag{3.19}$$

$$E_{i2} = E_{i1} \frac{-ak^*}{-ar^* + e^{-j\theta}} \tag{3.20}$$

$$E_{t2} = E_{i1} \frac{-k^*}{1 - ar^* e^{j\theta}} \tag{3.21}$$

So the transmission power P_{t1} and circulating power P_{i2} can be expressed as

$$P_{t1} = P_{i1} \cdot \frac{a^2 + |r|^2 - 2a|r| \cdot \cos(\theta + \varphi_t)}{1 + a^2|r|^2 - 2a|r| \cdot \cos(\theta + \varphi_t)} \tag{3.22}$$

where $r = |r|e^{j\varphi_t}$, $|r|$ represents the magnitude of the field transmission coefficient, φ_t represents the phase change of field in the coupling region.

The intensity transmission of the microring T can be expressed as

$$T = \frac{a^2 + |r|^2 - 2a|r| \cdot \cos(\theta + \varphi_t)}{1 + a^2|r|^2 - 2a|r| \cdot \cos(\theta + \varphi_t)} \tag{3.23}$$

The transmission spectrum of a microring is shown in Figure 3.5. The radius of the microring is 10 µm. Field transmission coefficient $|r|$ is 0.9, and loss coefficient a is 0.9.

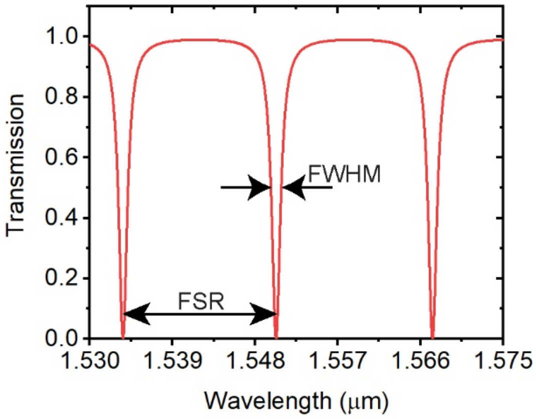

Figure 3.5 The transmission spectrum of a single ring resonator with a radius of 10 µm. Field transmission coefficient $|r|$ is 0.9, and loss coefficient a is 0.9.

The spacing between two consecutive resonances is the free spectral range (FSR) of the resonator. The FSR is equal to the wavelength change required for the round-phase of the resonator to undergo a 2π shift. Based on Eq. (3.15), the round-trip phase of the microring is

$$\phi_r = n_{eff}(2\pi/\lambda)2\pi R \tag{3.24}$$

We take the derivative with respect to the wavelength to get

$$\frac{d\phi_r}{d\lambda} = \left(\frac{dn_{eff}}{d\lambda} - \frac{n_{eff}}{\lambda}\right)\frac{2\pi}{\lambda}2\pi R$$

$$= -n_g \frac{2\pi}{\lambda^2} 2\pi R \tag{3.25}$$

where n_g is the group index of the microring waveguide.

So the FSR can be expressed as

$$\left|\Delta\lambda_{FSR}\right| = \frac{2\pi}{\left|d\phi_r / d\lambda\right|} = \frac{\lambda^2}{n_g 2\pi R} \tag{3.26}$$

The next important parameter is the resonance width, defined as the full width at the half maximum of the resonance lineshape. The FWHM can be expressed as

$$FWHM = \frac{(1-ra)\lambda_{res}^2}{\pi n_g L\sqrt{ra}} \tag{3.27}$$

where $L=2\pi R$.The FWHM can be used to calculate the quality factor (Q-factor), which represents the ability of a resonator to store energy. The Q-factor can be expressed as the ratio of the resonant wavelength to the bandwidth

$$Q = \frac{\lambda_{res}}{FWHM} = \frac{\pi n_g L\sqrt{ra}}{(1-ra)\lambda_{res}} \tag{3.28}$$

The Q-factor can also be regarded as the stored energy divided by the power lost per optical cycle.

3.2 Design of the vortex beam emitter

In this section, the proposed integrated THz vortex beam emitter will be presented. Figure 3.6 illustrates the microstructures of the emitter. The emitter is a waveguide-coupled, multi-layered microdisk that converts two infrared waveguide modes into free-space THz light through the nonlinear process of DFG. $LiNbO_3$ is chosen as the waveguide material because of its high nonlinear coefficient [172, 187-189] and increasing importance in integrated photonic circuits [190, 191]. The waveguides have two segments, a straight bus waveguide and a microring resonator. They are in the same plane and have the same rectangular cross-section that is 1 µm in width and 800 nm in height. The microring has a bend radius, defined as being from the inner boundary of the waveguide, of 18.68 µm, and a gap with the straight waveguide of 200 nm. The $LiNbO_3$ waveguides are embedded in a SiO_2 cladding layer, a common configuration of lithium niobate on insulator (LNOI) platforms [190, 191]. The thickness of the cladding layer is 4.6 µm in total and 2 µm beneath the $LiNbO_3$ waveguides. The bottom of the SiO_2 layer is fully covered by an unstructured Au base film, which has a thickness of 1 µm. A Si microdisk and an Au angular grating, which are concentric to the $LiNbO_3$ microring, are on top of the SiO_2 layer. The Si microdisk has a radius of 22 µm and a thickness of 3 µm. The Au angular grating on top of it has 8 periodic elements, an outer radius of 22 µm, and a thickness of 1 µm. Each of the 8 notches has a depth of 10 µm, an open angle of 200°, and a flat base with a width of 4 µm.

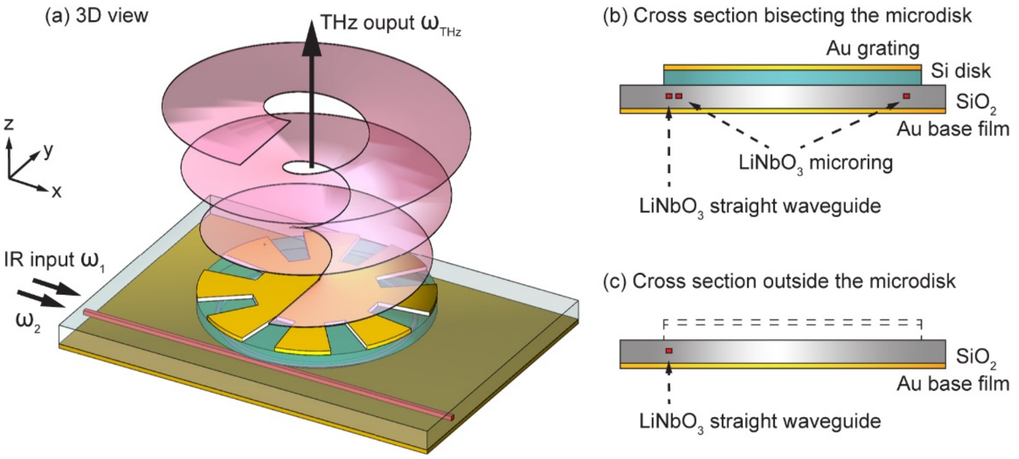

Figure 3.6 Schematic of the proposed THz light source. (a) Two infrared pump waves with angular frequencies ω_1 and ω_2 are coupled into a $LiNbO_3$ microring resonator via a $LiNbO_3$ bus waveguide. Both the microring and the bus waveguide are embedded in a SiO_2 cladding film, which is on top of a planar Au base film. A Si microdisk and an Au circular grating are on top of the microring, and these three components are concentric. The device converts the two waveguide-confined pump waves into a freely propagating THz wave. The THz wave is radiated outwards from the Au grating output-coupler, carrying a tuneable topological charge. (b) Device cross-section bisecting the microdisk. (c) Device cross-section outside the microdisk, with the edges of the Si microdisk and the Au grating shown in dashed lines.

The THz emitter is pumped by two infrared light beams with angular frequencies of ω_1 and ω_2. The infrared light is evanescently coupled from the straight waveguide into the ring waveguide, where it forms WGM resonances. Due to the resonance enhancement, the microring has an enhanced nonlinear efficiency [180, 192] in the generation of the THz light ω_{THz}, where $\omega_{THz} = \omega_1 - \omega_2$. It is worth noting that the microring configuration can be used to enhance many different nonlinear processes, among which difference-frequency generation is the only second-order nonlinear process that generates THz light. As shown below, similar to the pump light circulating along the $LiNbO_3$ microring, the THz light can form a WGM that traces the circumference of the Si microdisk. The THz light is further confined by the Au angular grating at the top, and the unstructured Au base film at the bottom, and leaky radiation from this subwavelength-thick cavity forms the output beam. As the unstructured Au base film, a closed-end of the leaky cavity, blocks any emission downwards, only the radiation above the emitter is studied.

A key aspect of the design in the generation of TC is the Au top grating. Top gratings have been used on a variety of light sources, such as light-emitting diodes [193], vertical-cavity surface-emitting lasers [194] and quantum cascade lasers [195, 196]. These gratings can control both the local optical density of states and the flow of light and are adopted mainly for improving the efficiency and the directionality of light emission. More recently, second-order surface gratings with rotational symmetry have been used to create vortex beams in linear light emitters [94, 98, 101, 104, 197, 198]. In contrast to these recent works, which are all in the near-infrared regime, this work adopts a different type of surface grating for use in the THz regime: it is metallic and covers a large area of the top surface of the light emitter. This approach benefits from the low ohmic loss in metals in the THz regime as compared to the near-infrared regime. It can also suppress direct light emission (i.e. emission that bypasses any interactions with a top grating) that can hinder the generation of pure vortex modes.

The performance of the device was numerically evaluated by using a commercial FDTD (finite-difference time-domain) solver (Lumerical FDTD Solutions). For linear properties, the permittivity of the materials, including $LiNbO_3$, SiO_2, Si and Au, was fitted based on experimental values [199, 200]. The fitting covered the whole range from the infrared to the THz and satisfied the Kramers-Kronig relations as required by the FDTD method. The representative values of all the materials used in the numerical simulation are presented in Table 3.1.

Table 3.1 Representative permittivity values of all the materials used in the numerical simulation. Both $LiNbO_3$ and SiO_2 are absorptive at λ_{THz}, which is a limiting factor for the output efficiency.

Material	λ_1 (1488.56 nm)	λ_2 (1582.75 nm)	λ_{THz} (25.0 µm)
$LiNbO_3$	$3.54+i4.47\times10^{-4}$	$3.53+i5.38\times10^{-4}$	$-2.40+i1.38$
SiO_2	$2.13+i2.55\times10^{-4}$	$2.13+i3.08\times10^{-4}$	$7.37+i2.11$
Si	$12.11+i1.02\times10^{-4}$	$12.06+i6.71\times10^{-5}$	$11.70+i6.09\times10^{-4}$
Au	$-103.30+i6.68$	$-118.79+i8.03$	$-17934.8+i15706.9$

$LiNbO_3$ was the only nonlinear material in the device, and its nonlinear coefficient [172, 187-189] was set as d_{33} = 170 pm/V. The two input infrared waves had equal power and were launched 40 µm away from the 200 nm gap (i.e. the location where the microring and the straight waveguide were the closest). Both waves were polarized in the same direction (TM polarization, magnetic field parallel to the substrate) in the z-cut $LiNbO_3$ waveguides in order to access this coefficient. Although this polarisation configuration forbids birefringence phase matching, quasi-phase matching could be used in future works to boost nonlinear efficiency (e.g. via decorating the microring with nanostructures).

3.3 Input properties of the device

Figure 3.7 shows the properties of the device at the pump wavelengths, i.e. in the infrared regime. To maximise the nonlinear conversion efficiency, the cross-section of the waveguide is designed to create a TM mode profile with most of the energy confined inside the waveguide (Figure 3.7(a)). Figure 3.7(b) shows light transmission through the straight waveguide after passing by the microring resonator. A series of sharp dips are observed in the transmission spectrum, each corresponding to the formation of a whispering gallery resonance mode in the microring. The quality factor of the resonances is ~2.2×10^3 at λ_1 = 1488.56 nm, with the material loss attributed as the main limiting factor. The average transmission is -8.3 dB at λ_1 and λ_2, and the average coupling efficiency is 85% under the assumption of zero scattering loss at the coupling section [180]. The wavelengths of the two input light beams are set at these resonances in order to benefit from the resonance enhancement of nonlinear effects in the microring.

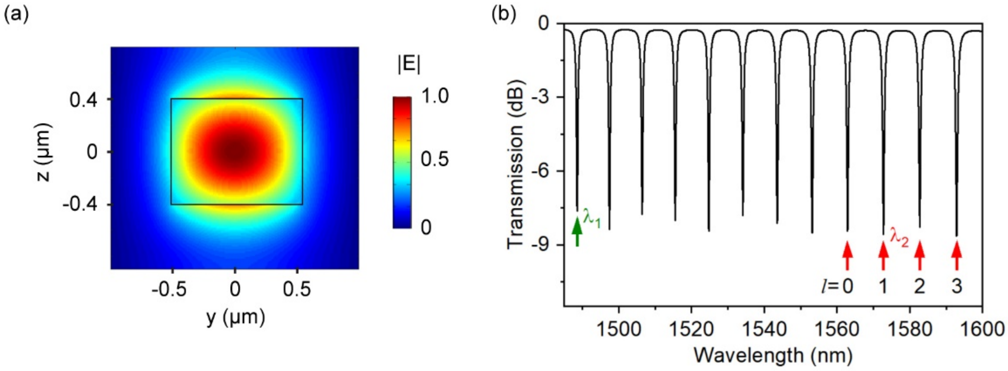

Figure 3.7 Properties of the straight waveguide at input wavelengths. (a) Electric field profile of the waveguide mode in the $LiNbO_3$ waveguide (black rectangle) and the SiO_2 layer. The field magnitude is normalised against its maximum value. The map shows the distribution at wavelength λ_1 = 1488.56 nm and remains almost unchanged over the entire spectral range of panel (b). (b) Transmission spectrum of the waveguide. One of the input wavelengths is fixed (λ_1, green arrow), while the other input wavelength λ_2 is tuned (red arrows) in order to change the topological charge of the radiated THz light.

3.4 Generation of topological charges

3.4.1 Angular phase-matching condition

The input light is confined by the $LiNbO_3$ waveguide and the SiO_2 embedding layer, which dictate the input properties of the device. In contrast, the THz light generated inside the $LiNbO_3$ microring has a much longer wavelength (~25 μm in free space) and penetrates into the Si microdisk. As shown in Figure 3.8, a Si microdisk with proper dimensions supports a WGM for the THz light. The conservation of orbital momentum [192, 201] in DFG requires the confined THz light to obey the condition of

$$m_{THz} = m_1 - m_2 \tag{3.29}$$

where m_{THz} is the azimuthal order of the generated THz light, and m_1 and m_2 are those of the pump light.

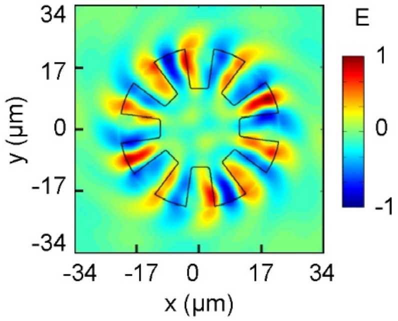

Figure 3.8 The z component of the THz electric field in the middle plane of the Si microdisk.

The Au grating on top of the Si microdisk out-couples the confined THz light into free space when an angular phase-matching condition is satisfied. The following part shows the derivation of the angular phase matching condition [94, 202]. For a small section of the microdisk, the waveguide is approximately straight. The phase-matching condition of the grating is

$$\beta_{rad} = \beta_{WGM} - g\frac{2\pi}{\Lambda} \tag{3.30}$$

where $\beta_{rad} = k sin(\theta)$ is the propagation constant for the radiating wave over the microdisk, $k = 2\pi/\lambda$ is the light wavevector in the vacuum and θ is the angle relative to the surface normal of the chip. $\beta_{WGM} = k \cdot n_{eff}$ is the propagation constant for the mode in the microdisk, n_{eff} is the effective refractive index of the mode in the microdisk. g is the diffraction order, and Λ is the grating period.

When the light goes along the microdisk starting at $\phi = 0$, Eq. (3.30) becomes

$$\beta_{rad} R\phi = \beta_{WGM} R\phi - g\frac{2\pi R}{\Lambda}\phi \tag{3.31}$$

Here we use $\nu = \beta R$ to present angular propagation constant. So Eq. (3.31) can be expressed as

$$\nu_{rad} = \nu_{WGM} - gq \tag{3.32}$$

where ν_{rad} is the angular propagation constant for the radiating wave over the microdisk. ν_{WGM} is the angular propagation constant for the mode in the microdisk. $q = 2\pi R/\Lambda$ is the number of grating elements.

The radiated light has an azimuthal phase dependence of exp $(i\nu_{rad}\phi)$. So ν_{rad} is corresponding to the radiated OAM order. For convenience, we use l to present ν_{rad}. $\nu_{WGM} = 2\pi R n_{eff}/\lambda$ is the azimuthal order (m_{THz}) of the THz wave in the microdisk. Therefore, Eq. (3.32) can be written as

$$l = m_{THZ} - gq \tag{3.33}$$

Since β_{rad} is one component of the wavevector $\boldsymbol{k}_{rad} = \beta_{rad}\hat{\boldsymbol{\phi}}+k_{\rho}\hat{\boldsymbol{\rho}}+k_{z}\hat{\boldsymbol{z}}$, the magnitude of the angular propagation constant is restricted by

$$\left|v_{rad}\right| \leq \left|k_{rad}R\right| = \left|\frac{2\pi R}{\lambda}\right| \tag{3.34}$$

Eq (3.34) means that

$$\left|l\right| = \left|m_{THz} - gq\right| \leq \left|\frac{2\pi R}{\lambda}\right| \tag{3.35}$$

So the possible *g* can be expressed as

$$\frac{m_{THz}}{q} - \frac{\Lambda}{\lambda} \leq g \leq \frac{m_{THz}}{q} + \frac{\Lambda}{\lambda} \tag{3.36}$$

In the device, m_{THz} is 10, *q* is 8, λ is around 25 µm, Λ is around 13.35 µm. *g* is in the order of 0.70 to 1.80. The only possible value for integer g is 1. Therefore, the angular phase matching condition Eq. (3.33) can be rewritten as [94]

$$l = m_{THz} - q \tag{3.37}$$

Substituting Eq. (3.29) into Eq. (3.37) leads to

$$l = m_1 - m_2 - q \tag{3.38}$$

Eq. (3.38) provides the basis for controlling the TC l in this work. For a given device where *q* is fixed, l can be tuned by adjusting the value of m_1–m_2. As indicated in Figure 3.7, this work chooses to demonstrate the tuning of l by fixing m_1 (i.e. fixing λ_1) and changing m_2 (i.e. changing λ_2).

3.4.2 Output properties of the device

To numerically verify the analysis above, Figure 3.9 shows the output properties of the device, with it functioning at $l = 2$. The input light waves are set at two microring resonances, with wavelengths of λ_1 = 1488.56 nm and λ_2 = 1582.75 nm. They generate a THz wave at ω_{THz} = 11.99 THz (wavelength λ_{THz} = 25.0 µm) based on the energy conservation in the nonlinear process. They also have $m_1 - m_2$ = 10, the number of FSRs between them in Figure 3.7. As predicted by Eq. (3.29), this value is also the azimuthal order of the WGM for the generated THz light. This prediction is confirmed by the results in Figure 3.8, where the near-field distribution in the Si microdisk shows ten cycles along the circumference of the microdisk. Figure 3.9(a) and Figure 3.9(b) show the intensity and phase of the THz light in the far-field, respectively. Every point on these two maps has a radial distance of one meter from the centre of the microdisk. Typical features of vortex beams are clearly revealed in the two figures: the intensity has a shape of a doughnut, and the phase has azimuthal dependence. Because of the side-pumping configuration, the intensity distribution in Figure 3.9(a) deviates from having perfect rotational symmetry, but the deviation is very small. Along a circle enclosing the centre of the map in Figure 3.9(b), the total phase evolves by twice of 2π, confirming that l = 2.

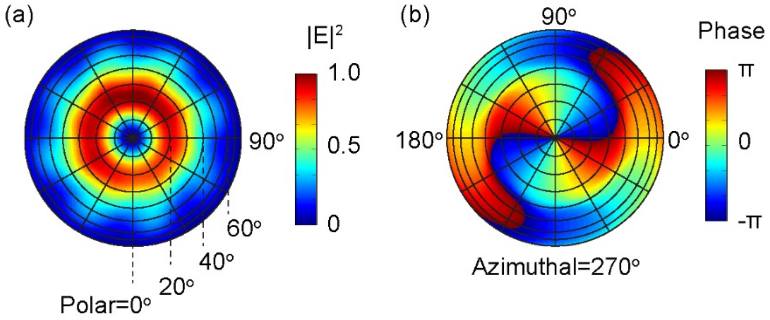

Figure 3.9 THz generation with topological charge l = 2. (a) The intensity and (b) phase of the THz radiation in the far-field, covering the whole upper hemisphere with the polar angle ranging from 0° to 90° and the azimuthal angle from 0° to 360°. The origin of the polar coordinates is at the centre of the Si microdisk. The in-plane directions of +x (i.e. the light propagation direction in the straight waveguide) and +y correspond to azimuthal angles of 0° to 90°, respectively.

For further verification of Eq. (3.38), Figure 3.10 compares four different operation modes of the emitter. As indicated in Figure 3.7, λ_1 is fixed at λ_1 = 1488.56 nm, while λ_2 chooses the value of 1562.89 nm, 1572.76 nm, 1582.75 nm and 1592.89 nm in Figure 3.10(a), (b), (c) and (d), respectively. The TC is predicted to range from 0 to 3 based on Eq. (3.38) , and it is confirmed by the results in Figure 3.10. For each value of l, the azimuthal components of the radiated THz field are plotted at three different planes. The inter-plane distance is $\lambda_{THz}/4$, where λ_{THz} varies with the value of l.

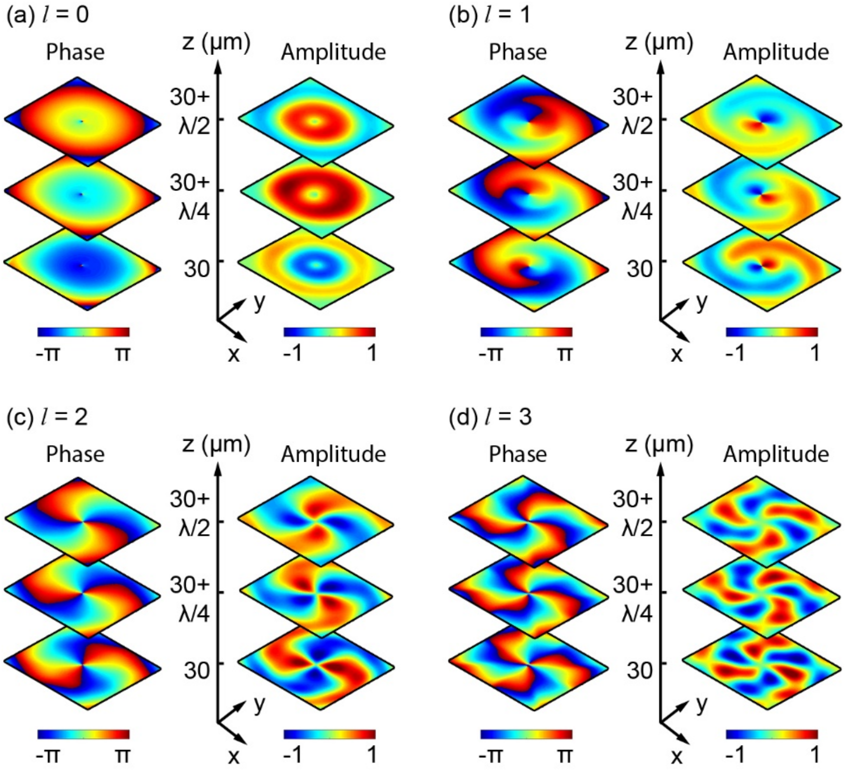

Figure 3.10 Azimuthal components of the emitted THz light with the device producing topological charges of (a) 0, (b) 1, (c) 2 and (d) 3. For each operation mode, the left and the right columns show the phase and the amplitude of the field, respectively. Each map occupies an area of 40 μm × 40 μm. The distance between adjacent maps is $\lambda_{THz}/4$, and the lowest plane is 30 μm above the centre of the microdisk. The amplitude in each map is normalised against the maximal value of the corresponding set of three maps.

A profound contrast is observed between the non-vortex beam (Figure 3.10(a)) and the vortex beams (Figure 3.10(b)-(d)): both the phase and the amplitude are twisted in the latter, while no such feature is discernible in the former. The small features very close to the centre of the phase maps of Figure 3.10(a) are attributed to numerical errors, as the local field intensity is almost zero. It is worth noting that the doughnut-shaped amplitude profile seen in Figure 3.10(a) does not imply the existence of a finite TC, and similar features have been reported previously in non-vortex beams produced by linear vortex beam emitters [197].

In contrast to Figure 3.10(a), the beams in Figure 3.10(b)-(d) all carry a finite value of TC l. The value of l is related to the twist of the fields and can be retrieved from the maps by using two different methods. The first method is to trace the rotation of the field in a xy plane: along a circle centred on the beam axis, the absolute value $|l|$ equals the cycle number of the phase or the amplitude, and the sign of l determines the direction (either clockwise or anti-clockwise) that the phase increases. The second method is to trace the rotation of the field along the z-direction: the field rotates by $2\pi/|l|$ for a distance of λ, and the sign of l determines the rotation direction for both the phase and the amplitude.

3.5 Output spectra of three different designs

Figure 3.11 shows the output spectra of the device in the frequency range from 9 THz to 13.5 THz.

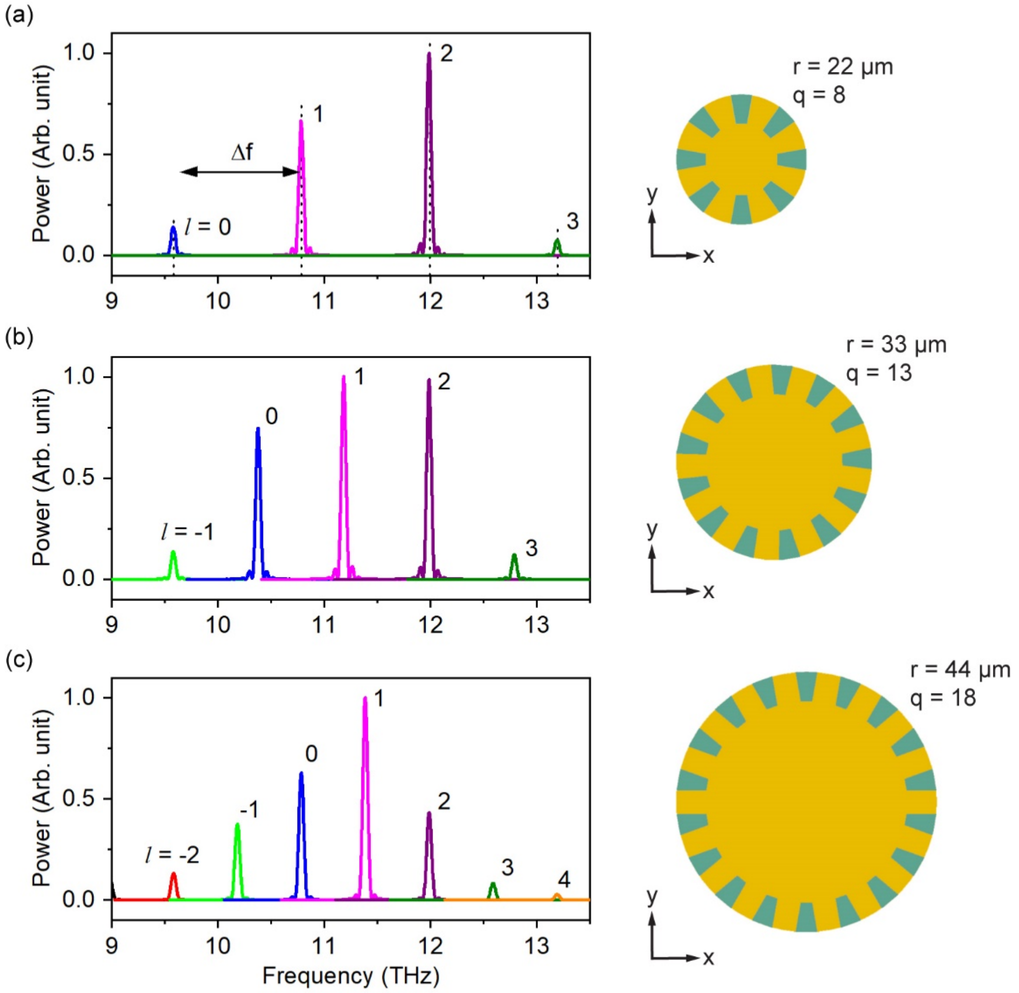

Figure 3.11 Influences of planar microstructures on the output spectra for three different designs. The diameter of the Si microdisk *r* and the number of grating elements *q* are (a) *r* = 22 μm, *q* = 8 (the design discussed in previous figures), (b) *r* = 33 μm, *q* = 13, and (c) *r* = 44 μm, *q* = 18. In panel (a), central peak positions calculated using energy conservation in the difference-frequency generation are indicated by vertical dashed lines. In panel (c), the peak of l= -3 is slightly outside the spectral range presented here, with its central frequency at 8.98 THz. In all the panels, a frequency shift *Δf* accompanies a unit change in the topological charge. The spectra in each panel are normalised against the highest output power of the corresponding design. For all the designs, the straight waveguide is along the x-direction.

As l changes from 0 to 3, the peak frequency changes by 3.61 THz, from 9.58 THz at l= 0 to 13.19 THz at l= 3. This change originates from the energy conservation in the DFG and follows the change of λ_2. The output power also depends on l. With both input light set at a test value of 10 W, the output reaches the highest value of 2.0 × 10^{-5} W at l= 2, and drops to 14% of this value at l = -1 and 8% at l= 3. This change in output power is directly related to the change in frequency, as the latter affects key characteristics such as light confinement of the microdisk and phase matching of the nonlinear process. All the peaks show a finite width, and some have small but discernible side bands. These features are artefacts associated with the FDTD method; both the peak width and the sidebands become smaller with increasing the simulation time (i.e. with waves better approximating perfect, monochromatic waves).

For this design architecture, a change in output frequency always accompanies a change in the TC due to the DFG. Nevertheless, the magnitude of the frequency change can be controlled by modifying the planar size of the design. As long as the pump wavelengths (λ_1 and λ_2, both ~1.5 µm in the current design) are significantly larger than the FSR (~10 nm in the current design), the frequency change Δf that accompanies a unit change in l (i.e. Δl = ±1) is approximately

$$\Delta f \approx c \times FSR / (\lambda_1 \times \lambda_1) \approx c \times FSR / \lambda^2 \tag{3.39}$$

where c is the speed of light, and λ is the average of λ_1 and λ_2. For a microring resonator, the FSR is inversely proportional to the round trip length along the microring [180]. If the radius r is significantly larger than the width of the waveguide, the FSR can be approximated as

$$FSR = \lambda^2 / (n_g \times 2 \times \pi \times r) \tag{3.40}$$

where n_g is the group velocity. This leads to the conclusion that by adjusting the radius of the microring, Δf can be controlled as

$$\Delta f \approx c / (n_g \times 2 \times \pi \times r) \tag{3.41}$$

The value of Δf scales inversely with the radius of the microring r.

To numerically verify this conclusion, the planar dimensions of the emitter are modified and the output spectra are shown in Figure 3.11. From the current design (Figure 3.11(a)), the radii of the microring, defined from the middle of the waveguide, and the Si microdisk are increased by 50% in Figure 3.11(b), reaching 28.77 µm and 33 µm, respectively. For the third design in Figure 3.11(c), the increase is 100%, and the radii of the microring and the Si microdisk are 38.36 µm and 44 µm, respectively. In order to create similar values of l in the same frequency range for the three designs, the element number of the Au grating is increased from q =8 in Figure 3.11(a) to 13 and 18 in Figure 3.11(b) and (c), respectively. All the other dimensions are the same for these three designs.

Figure 3.11 compares the three designs in the same frequency range from 9 THz to 13.5 THz. The number of peaks is 4, 5 and 7 in Figure 3.11(a), (b), (c), respectively, increasing with the planar size of the emitter. The frequency difference between adjacent peaks Δf shows the opposite trend of change, which is 1.20 THz, 0.80 THz and 0.60 THz in Figure 3.11(a), (b), (c), respectively. To compare these values with results obtained from Eq. (3.41), the group velocity n_g is calculated at a representative wavelength of 1550 nm. The value shows a very small variation with the design, and it is 2.07, 2.06 and 2.09 for the designs in Figure 3.11(a), (b), (c), respectively. The analytical values of Δf obtained from Eq. (3.41) are consequently 1.20 THz, 0.80 THz and 0.60 THz for the three designs, matching very well with the values obtained directly from Figure 3.11.

3.6 Conclusion

To conclude, we have demonstrated a THz vortex beam emitter via numerical simulation. The emitter consists of a $LiNbO_3$ microring for DFG, a Si microdisk for near-field confinement of the generated THz, and an Au second-order top grating for the creation of TC. The device is pumped by two infrared light beams from a coupling waveguide and emits THz light vertically into free space. The value of the TC can be tuned by changing the wavelengths of the incident light and ranges from -2 to 4 in the simulated frequency range from 9 THz to 13.5 THz for one of the three designs. The output spectra, in particular the frequency change that is associated with the change in TC, can be adjusted by tuning the planar dimensions of the emitter. As a proof-of-principle demonstration, this work concentrates on the TC and the frequency shift, while parameters such as conversion efficiency, including its balance among multiple output spectra peaks, could be further improved by exploring the vertical dimensions (e.g. via creating high-quality THz WGMs) [203]. The emitter has a planar dimension that is comparable to its functional wavelengths and has the capability to impart a tunable TC on a freely propagating THz light beam. These features can prove useful in a range of emerging THz applications, such as THz sensing and wireless communications.

.

Chapter 4 Coherent generation of arbitrary first-order Poincaré sphere beams on a Si chip

In the previous chapter, an integrated THz vortex beam emitter is demonstrated based on microring resonators. It provides a compact method allowing for both the generation and tuning of OAM in the THz range. This chapter explores the controlled generation of SOPs of VV beams, which could be utilized for sensing and communications. For example, the spatially variant polarization of VV beams provides a new degree of freedom for detecting targets' motion vectors, which is useful for LiDAR applications [109]. In this chapter, we present the first on-chip light emitter that allows for the controllable generation of all points on a first-order Poincaré sphere (FOPS).

The FOPS beam generator consists of a Si microring resonator with azimuthally distributed cylindrical holes etched on top of the ring waveguide. The confined waves in the microring can be converted into freely propagating output light. By matching the WGMs with the nanoholes, the fundamental TE and TM modes in the microring can produce radial and azimuthal polarization patterns, respectively. The two orthogonal polarization patterns can be the basis for the FOPS. Tuning the phase contrast and the intensity ratio of these two coherent inputs allows for generating an arbitrary point on the FOPS. Most results in this chapter have been published by the journal "Optics Express".

4.1 Design schematic of the FOPS beam emitter

Figure 4.1 schematically illustrates the FOPS beam emitter. The device utilizes a silicon-on-insulator (SOI) platform, a common choice for on-chip light sources and photonic integrated circuits [6, 180]. It consists of a Si microring resonator and a Si bus waveguide embedded inside a 4.3-μm thick layer of SiO_2, with the bottom of these two embedded components 2 μm above the Si substrate. Both components have a square cross-section with a side length of 300 nm. The microring has a bend radius, defined as being from the inner boundary of the waveguide, of 5 μm, and a gap with the straight waveguide of 300 nm. The top of the microring is decorated with 35 shallow, cylindrical holes that distribute uniformly along the centre of the waveguide. These holes have a depth of 100 nm and a diameter of 100 nm. They function as the grating elements for light out-coupling, converting confined waveguide modes to freely propagating output light.

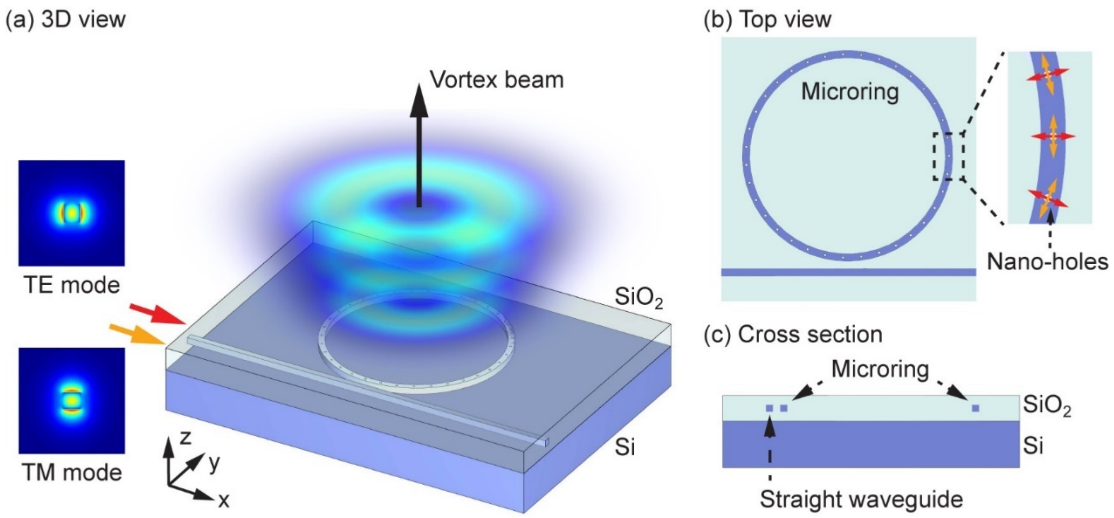

Figure 4.1 Schematic of the FOPS beam emitter. (a) The emitter consists of a Si microring resonator evanescently coupled to a straight bus waveguide. Driven by the fundamental TE and TM modes fed into the bus waveguide, the microring radiates light into free space in the vertical direction. The polarization state of the output light is modulated by tuning the phase contrast and the intensity ratio of the two input modes, and it can sweep over the whole FOPS. (b) The microring is decorated on top with 35 uniformly distributed, shallow nano-holes that function as an angular grating for light out-coupling. The inset is a zoomed-in view of a section of the microring. The TE and TM input modes, which have the same wavelength, produce radially and azimuthally polarized components in the output beam. (c) Cross-sectional view of the device at the plane bisecting the microring.

The performance of the FOPS beam emitter was numerically evaluated by using a commercial FDTD solver (Lumerical FDTD Solutions). A free-space wavelength range from 1658 nm to 1722 nm was simulated. The device was assumed to have zero light absorption in the whole range. The permittivity of Si and SiO$_2$ was obtained by fitting experimental measurement [200], and the values were 12.03 and 2.08, respectively, at the emitter working wavelength of $\lambda = 1685.59$ nm. The device was driven by the fundamental TE and TM modes of the bus waveguide, which were launched 6 µm away from the 300 nm gap (i.e. the location where the microring and the straight waveguide were the closest). In the following discussions, the phase contrast between the two coherent input modes always refers to this specific input plane. Nevertheless, as the TE and TM modes have almost identical effective indices (1.846068 versus 1.846072) due to the square shape of the cross-section, the phase contrast in the straight waveguide is almost invariant as the two modes propagate forward, and the location of the input plane has no significant influence on the device characteristics.

4.2 Input properties of the light emitter

Figure 4.2 shows the transmission spectra of the fundamental TE and TM modes propagating in the bus waveguide. Both spectra contain a series of sharp resonance dips, each corresponding to a WGM in the microring. In both spectra, the two closely spaced resonance dips between 1680 nm and 1700 nm form a resonance doublet. These doublets are characteristics of mode splitting caused by the coupling between counter-propagating WGMs inside the ring [101]. Both the singlet and doublet resonances occur at similar wavelengths for the two input modes. This similarity originates from the highly symmetric shape of the waveguide cross-section (a square), as well as the uniformity of the embedding environment (i.e. both the straight and circular waveguides are fully covered with a SiO_2 layer). The differences between these two spectra are attributed to the asymmetry introduced by the microring-waveguide coupling region and the nano-hole top grating.

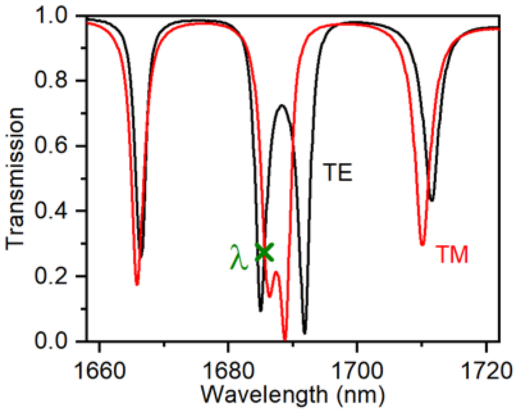

Figure 4.2 Transmission spectra of the TE and TM modes in the bus waveguide. The emitter working wavelength is λ=1685.59 nm (green cross).

As will be discussed in detail below, the FOPS beam generation requires both the TE WGM and the TM WGM to have an azimuthal order of 35, the same as the number of the grating elements (i.e. the nano-holes). This condition is satisfied only in the resonance doublet. To simplify the analysis, we further require the TE and TM inputs to have similar waveguide transmission at the device's working wavelength. The wavelength is consequently chosen as λ = 1685.59 nm, a wavelength in the resonance doublet where the TE and TM transmission is approximately equal to 0.28.

Figure 4.3 shows the electric near field at this wavelength for the two inputs. The results confirm that both inputs generate a WGM in the microring, and the WGM has an azimuthal order of the target value of 35. Despite this similarity in azimuthal order, the two WGMs are distinct in the details of field distribution. Most relevant to the light out-coupling is the field strength along the circumference passing the middle of the microring (i.e. the centres of the nano-holes). For the TE input, the field strength is almost zero for the azimuthal component. In contrast, for the TM input, it is the radial component that has nearly zero strength. This contrast between the azimuthal and radial components underpins our technique of arbitrary FOPS beam generation.

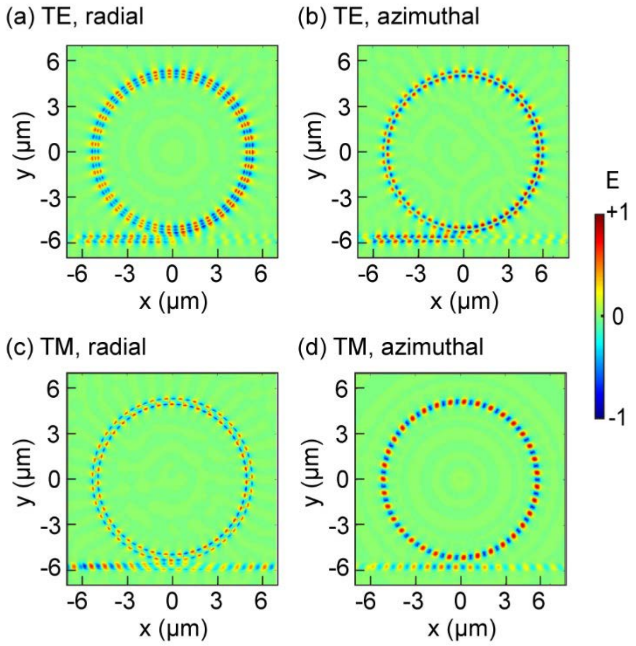

Figure 4.3 Near-field properties of the FOPS beam emitter. (a) The radial and (b) the azimuthal component of the electric field in the microring, with the microring driven only by the TE input mode. (c,d) Corresponding field components under the TM input. All four maps show the same xy plane that passes through the middle height of the nano-holes.

4.3 Vortex beam generation using a single input mode

Due to their different near-field distributions inside the microring, the TE and TM inputs generate two freely propagating light beams with distinct features. Figure 4.4 shows the intensity and phase distributions of these two output beams analyzed at a radial distance of one meter from the device centre.

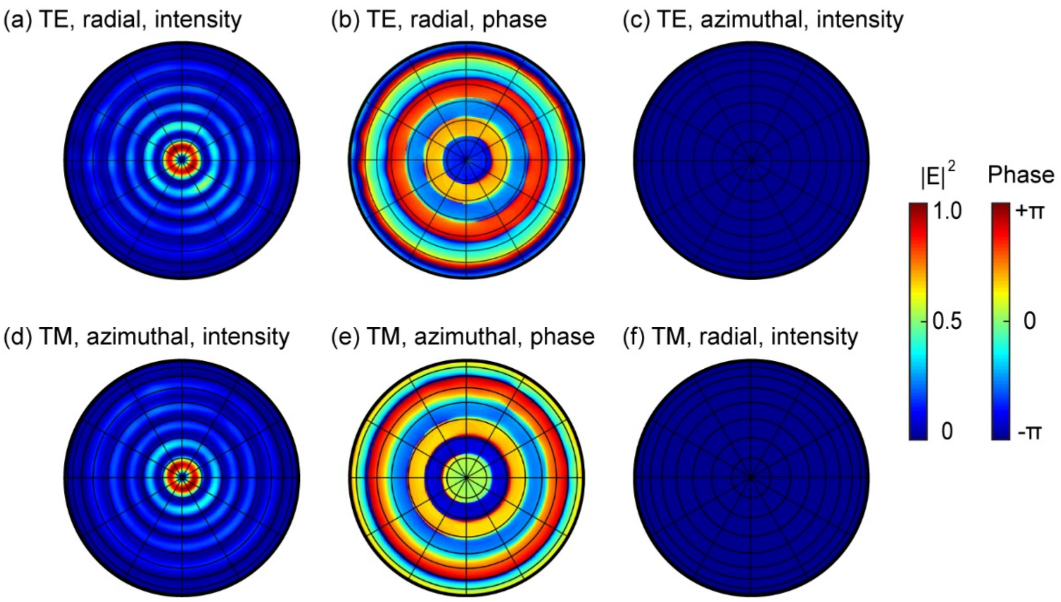

Figure 4.4 Far-field radiation polar maps with the device driven by a single waveguide mode. (a-c) The intensity and phase distributions under the TE mode excitation. At the same intensity scale, (a) the radial component is clearly visible, while (c) the azimuthal component is indiscernible. (b) The phase of the dominant component (i.e. the radial component). (d-f) The corresponding intensity and phase distributions under the TM mode excitation. The phase is still for the dominant component, which is now the azimuthal component.

In the analysis, the radially (E_{RAD}) and azimuthally (E_{AZ}) polarized components are extracted [204] using the Jones vectors as below,

$$E = E_{RAD} + E_{AZ} = \sum_l \psi^l_{RAD} \exp(il\theta) \begin{bmatrix} \cos\theta \\ \sin\theta \end{bmatrix} + \sum_l \psi^l_{AZ} \exp(il\theta) \begin{bmatrix} -\sin\theta \\ \cos\theta \end{bmatrix} \tag{4.1}$$

where θ is the azimuthal angle and *i* is the imaginary unit number. l is the TC, and it is an integer (i.e. 0, ±1, ±2 etc.). ψ^l_{RAD} is the coefficient for the radial component, which has an amplitude of $|\psi^l_{RAD}|$ and a phase of ϕ^l_{RAD}, and ψ^l_{AZ} is that for the azimuthal component.

Figure 4.4(a)-(c) analyze the output generated by a single TE input beam. The field is predominantly radially polarized: while the radial component shows clearly a set of concentric rings in its intensity distribution [Figure 4.4(a)], the azimuthal component at the same intensity scale is not discernible [Figure 4.4(c)]. Further analysis leads to an intensity ratio between the radial and the azimuthal components $|\psi^l_{RAD}/\psi^l_{AZ}|^2$, which can be expressed alternatively as I^l_{RAD}/I^l_{AZ}, of 98.56:1.44. The rings in Figure 4.4(a) are slightly distorted and lack perfect rotational symmetry. This imperfection is attributed to the inhomogeneous field distribution inside the microring: the near-field amplitude has a noticeable decrease as the light traces the ring in the anti-clockwise direction from the microring-waveguide gap [Figure 4.3(a)], creating a small variation among the 35 nano-holes in their light scattering strength. For all the intensity rings in Figure 4.4(a), the phase stays constant [Figure 4.4(b)], implying that the vortex beam carries no TC. These results of Figure 4.4(a)-(c) lead to the conclusion that the output beam is a radially polarized cylindrical vector beam, which corresponds to a point on the equator of the FOPS.

Changing the input light from the TE mode to the TM mode profoundly changes the output [Figure 4.4(d)-(f)], and the azimuthally polarized component becomes the dominant component. The intensity ratio between the radial and the azimuthal components $|\psi_{RAD}^{l}/\psi_{AZ}^{l}|^2$ (equivalently I_{RAD}^{l}/I_{AZ}^{l}) now becomes 0.98:99.02. Despite this reverse in the dominant component, many key features in the output are retained: the intensity distribution consists of a set of concentric rings [Figure 4.4(d)], and the phase is invariant in each ring [Figure 4.4(e)]. We can draw a similar conclusion here that the output beam is now an azimuthally polarized cylindrical vector beam, which also corresponds to a point on the equator of the FOPS.

The phase distributions shown in Figure 4.4(b) and (e) indicate that, both ψ_{RAD}^{l} and ψ_{AZ}^{l} are dominated by the term of $l = 0$. For this reason, in the following discussions, we omit the annotation of l unless it may cause confusion; ψ_{RAD}^{l}, ψ_{AZ}^{l}, ϕ_{RAD}^{l}, ϕ_{AZ}^{l}, I_{RAD}^{l} and I_{AZ}^{l} are simply written as ψ_{RAD}, ψ_{AZ}, ϕ_{RAD}, ϕ_{AZ}, I_{RAD} and I_{AZ}, respectively.

The results in Figure 4.4 can be interpreted based on the near-field distribution inside the microring (Figure 4.3). Each nano-hole on the microring functions as a nano-antenna that radiates the wave confined inside the microring into free space. For highly symmetric configurations, such as the azimuthally polarized and radially polarized waveguide modes scattered by a cylindrical nano-hole, the symmetry has to be preserved in light scattering [98]. This constraint implies that radial and azimuthal polarization components dominate the output for TE and TM inputs, respectively.

Although its polarization varies with the input, the output beam has a TC l that stays invariant between the TE and TM input modes. Regardless of the input mode, the output beam is always formed by the constructive interference of light scattered by all the nano-holes. Its TC l can be calculated by using the angular phase-matching condition [94] presented in section 3.4.1

$$l = m - q \tag{4.2}$$

Here m is the azimuthal order of the resonance mode inside the microring (i.e. the cycle number of the WGM), and q is the number of the grating elements (i.e. the number of nano-holes). At the working wavelength of 1685.59 nm, the TC l is 0, as $m = q = 35$ (Figure 4.3). Based on the symmetry constraint specified above, along with the zero TC, we can conclude that TE and TM inputs produce radially and azimuthally polarized cylindrical vector beams, respectively. This analytical conclusion fits with the numerical results in Figure 4.4.

4.4 Vortex beam generation using two input modes

4.4.1 Stokes parameters for the FOPS

With two specific points (i.e. polarization states) on the FOPS equator produced, we discuss in the following sections the method to reach an arbitrary point on the FOPS. For any HOP sphere, the most common method of using two coherent beams to conduct such scans is to use circularly polarized light beams with opposite helicity (i.e. the two poles of the sphere) [93, 130, 139, 143, 146, 154, 205, 206]. As far as we know, this is the only method that has been used in FOPS analysis. In contrast, here we highlight the fact that such superposition can utilize any orthogonal set of polarization states (i.e. any antipodal points on a sphere). This includes the radial and azimuthal polarization states shown in Figure 4.4.

Figure 4.5 shows the generation of VV beams using both TE and TM input modes. According to section 4.3, TE and TM input modes can generate radially and azimuthally polarized vector beams, respectively. The input intensity of the TE and TM modes (I_{TE} and I_{TM}) dominates the output intensity I_{RAD} and I_{AZ}, respectively, and their phase contrast $\phi_{TM} - \phi_{TE}$ determines the value of $\phi_{AZ} - \phi_{RAD}$. When the input contains both the TE and TM modes, the output polarization state is the coherent interference of the azimuthally and radially polarized components. This implies that I_{TE}, I_{TM}, ϕ_{TE} and ϕ_{TM} all influence the output.

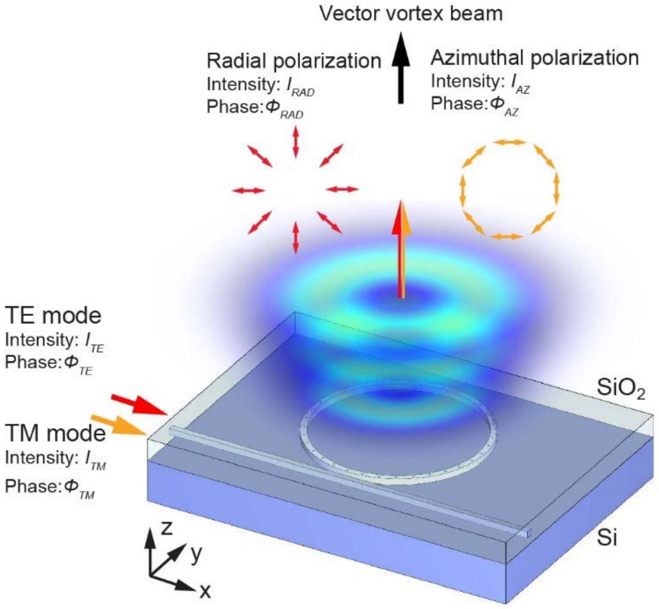

Figure 4.5 Illustration of the vector vortex beam generation using TE and TM input modes.

By using the radial and azimuthal polarizations as the basis (i.e. a set of orthonormal eigenstates) for the FOPS, the higher-order Stokes parameters (SPs) are expressed as

$$S_0 = \left|\psi_{RAD}\right|^2 + \left|\psi_{AZ}\right|^2 = I_{RAD} + I_{AZ} \tag{4.3}$$

$$S_1 = \left|\psi_{RAD}\right|^2 - \left|\psi_{AZ}\right|^2 = I_{RAD} - I_{AZ} \tag{4.4}$$

$$S_2 = 2\left|\psi_{RAD}\right|\left|\psi_{AZ}\right|\cos(\phi_{AZ} - \phi_{RAD}) = 2\sqrt{I_{RAD}I_{AZ}}\cos(\phi_{AZ} - \phi_{RAD}) \tag{4.5}$$

$$S_3 = 2\left|\psi_{RAD}\right|\left|\psi_{AZ}\right|\sin(\phi_{AZ} - \phi_{RAD}) = 2\sqrt{I_{RAD}I_{AZ}}\sin(\phi_{AZ} - \phi_{RAD}) \tag{4.6}$$

It is worth noting that these expressions are derived based on the SPs of a conventional Poincaré sphere using the linear polarization basis [207]; they are consequently different from the SPs of a FOPS using the circular polarization basis. It is always true that $|S_1|^2 + |S_2|^2 + |S_3|^2 = |S_0|^2$. For simplicity, we set the total intensity S_0 as unity value in the following analysis, as all the beams are fully polarized. This implies that every point on the FOPS can be identified using a unique set of S_1, S_2 and S_3.

The analysis above shows the relationship between the output polarization states and the input parameters (I_{TE}, I_{TM}, ϕ_{TE} and ϕ_{TM}). The sections below will numerically evaluate the relationship.

4.4.2 Longitudinal scan on the FOPS

Figure 4.6 shows the evolution of the output beam as the phase contrast of the two inputs $\phi_{TM} - \phi_{TE}$ scans a full cycle of 360°. During the phase scan, the intensity ratio of the two inputs I_{TE}/I_{TM} is set as a constant of 2.53. This value is identified by matching the total output intensity in Figure 4.4(a) and (d), and is very close to creating the condition that the TE input and the TM input generate an equal amount of total output power. This ratio is not unity as might be predicted intuitively from Figure 4.2, and it originates from the different field distributions of the two modes inside the waveguide [Figure 4.3].

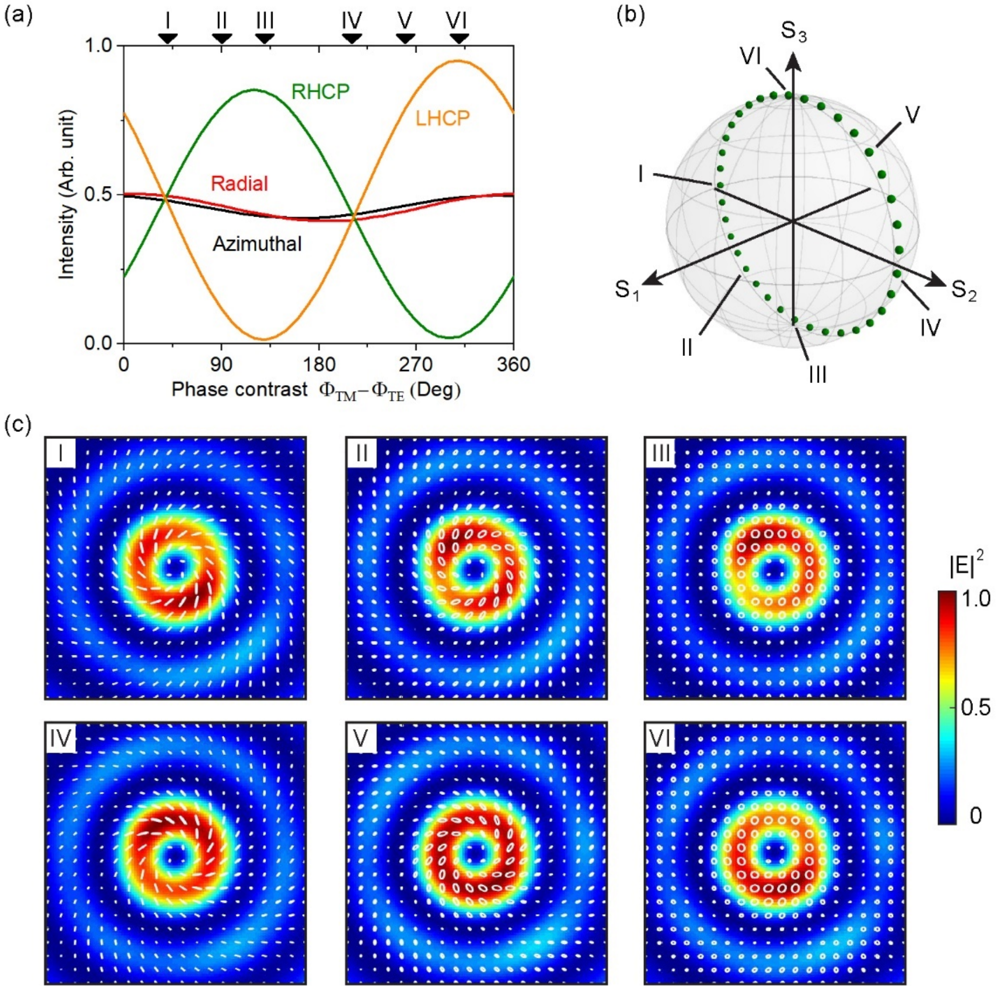

Figure 4.6 Phase-controlled polarization evolution on the FOPS. (a) The output light is decomposed into radially and azimuthally polarized components, and alternatively into left-handed circularly polarized (LHCP) and right-handed circularly polarized (RHCP) components, as the input phase contrast $\phi_{TM} - \phi_{TE}$ changes from 0 to 360°. Six representative $\phi_{TM} - \phi_{TE}$ values (40°, 90°, 130°, 210°, 260° and 310°) are specified using numbers I to VI. (b) Polarization evolution on the FOPS beam (green dots) in the scan of the input phase contrast, with the six representative values specified. (c) The distributions of field intensity (colour maps) and polarization (white ellipses and lines) for the six representative states. Each map corresponds to an area of 14 µm × 14 µm in the plane 20 µm above the top surface of the emitter. The intensity of each map is normalized against its respective maximum.

At every phase contrast $\phi_{TM} - \phi_{TE}$, the output field is decomposed into the radially and azimuthally polarized components following Eq (4.1), as well as into the left-handed and right-handed circularly polarized components (i.e. the two poles of the FOPS, here as E_L and E_R). The second type of decomposition is expressed as [94, 204]

$$E = E_L + E_R = \psi_L^{-1} \exp(-i\theta) \frac{1}{\sqrt{2}} \begin{bmatrix} 1 \\ +i \end{bmatrix} + \psi_R^{+1} \exp(i\theta)) \frac{1}{\sqrt{2}} \begin{bmatrix} 1 \\ -i \end{bmatrix} \tag{4.7}$$

where ψ_L^{-1} and ψ_R^{+1} are the coefficients for the left-handed circularly polarized (LHCP) and right-handed circularly polarized (RHCP) components, respectively. It is worth highlighting that the two circular components have finite and opposite TCs (i.e. -1 and +1), which is different from the linear components.

Figure 4.6(a) shows the results of these two types of decomposition. As the TE and TM input modes generate predominantly radially and azimuthally polarized output light, respectively, the total output intensity is shared roughly equally between the radial and the azimuthal components throughout the 360° phase scan. Meanwhile, as the output is neither purely radial nor purely azimuthal for a single input mode (as discussed above, I_{RAD}/I_{AZ} is 98.56:1.44 and 0.98:99.02 for purely TE and TM input, respectively), a low level of intensity interference exists in the output. It induces a small fluctuation in I_{RAD}, I_{AZ} and I_{RAD}+I_{AZ} in scanning $\phi_{TM} - \phi_{TE}$. In comparison to the linear basis, decomposing the output into circular polarizations shows a much bigger dependence on $\phi_{TM} - \phi_{TE}$: the ouput oscillates between almost purely left-handed (at $I_{RHCP} \approx 0$) to almost purely right-handed (at $I_{LHCP} \approx 0$).

The characteristics of I_{RAD}, I_{AZ}, I_{RHCP} and I_{LHCP} identified above lead to these two features related to the FOPS: (1) $S_1 = I_{RAD} - I_{AZ} \approx 0$ as $\phi_{TM} - \phi_{TE}$ scans by 360°; (2) the two poles of the FOPS, which correspond to two pure circular polarization states, are reached in the scan. Based on these two features, we can predict that, the output polarization produced by a full 360° scan of $\phi_{TM} - \phi_{TE}$ traces the great circle normal to the S_1 axis. This prediction is confirmed in the more detailed analysis shown in Figure 4.6(b) and (c).

At each $\phi_{TM} - \phi_{TE}$, the intensity distribution of the output light is similar to Figure 4.4(a) and (d): it is a set of concentric rings, with most intensity concentrated in the smallest ring. As opposed to Figure 4.6(a), which is based on the analysis of the total output intensity, we concentrate on the smallest ring for Figure 4.6(b) and (c). Figure 4.6(c) shows both the intensity and the polarization distributions of this ring, with $\phi_{TM} - \phi_{TE}$ taking six representative values of 40°, 90°, 130°, 210°, 260° and 310°. The doughnut-shaped intensity distribution lacks perfect rotational symmetry, similar to the results shown in Figure 4.4, and this imperfection is also present in the polarization distribution. To link these polarization maps with points on the FOPS, for each map, we compute the averaged polarization state along the circle that centres on the beam axis and passes the maximal intensity. This averaged polarization state is then identified on the FOPS in Figure 4.6(b). This exercise is conducted for 36 values of $\phi_{TM} - \phi_{TE}$, from 0° to 360° at a step of 10°. Consistent with our prediction above, the polarization traces a great circle on the FOPS that is normal to the S_1 axis.

The great circle intersects with the equator at two points as seen in Figure 4.6(b). As every point on the equator contains an equal amount of the polarization states at the two poles [120], these two points can be identified as the two points in Figure 4.6(a) where the LHCP and the RHCP lines intersect. They correspond to $\phi_{TM} - \phi_{TE}$ of 38° and 212°. These two values are important to the FOPS beam generation, and are to be used for the numerical simulation shown in Figure 4.7.

Before concluding the analysis on the phase-based (i.e. tuning $\phi_{TM} - \phi_{TE}$) scan and starting that on the intensity-based (i.e. tuning I_{TM}/I_{TE}) scan (Figure 4.7), it is worth analyzing briefly the imperfection seen in Figure 4.6. In an ideal, perfect device that allows for the most straightforward control over the output polarization, as $\phi_{TM} - \phi_{TE}$ changes steadily from 0° to 360°, the point on the FOPS would move longitudinally at a constant speed on a great circle. The device analyzed here slightly deviates from this ideal scenario, and the degree of deviation can be roughly gauged using a particular phase difference. As a numerical indication, here we use the two points where the great circle intersects the FOPS equator, which are discussed above. In the perfect device, the phase difference between these two points is 180°. The discussion above shows that these two points correspond to $\phi_{TM} - \phi_{TE}$ of 38° and 212° in Figure 4.6(a), which have a difference of 174°. As benchmarked against the ideal device with regard to this parameter, our device drifts by a small value of 6°, or 3.3% in relative magnitude.

4.4.3 Latitudinal scan along the FOPS equator

In addition to the longitudinal scan on the FOPS shown in Figure 4.6, it is also possible to conduct a horizontal scan along its equator (Figure 4.7). Based on Eqs. (4.4)-(4.6), such polarization evolution can be achieved by adjusting S_1 and S_2, while maintaining $S_3 = 0$. The constraint on S_3 leads to two possible values of $\phi_{TM} - \phi_{TE}$, which are 38° and 212° as discussed above. Further analysis based on Eqs. (4.4)-(4.6) show that the value of $\arctan\left(\left|\psi_{AZ}/\psi_{RAD}\right|\right)$, or expressed equivalently as $\arctan\left(\sqrt{I_{AZ}/I_{RAD}}\right)$, is associated with the azimuthal position of the corresponding polarization state on the FOPS equator. This observation implies that the latitudinal scan can be achieved by tuning the input intensity ratio I_{TM}/I_{TE}, as it is proportional to the output ratio I_{AZ}/I_{RAD}. Figure 4.7 analyzes this intensity-controlled FOPS scan.

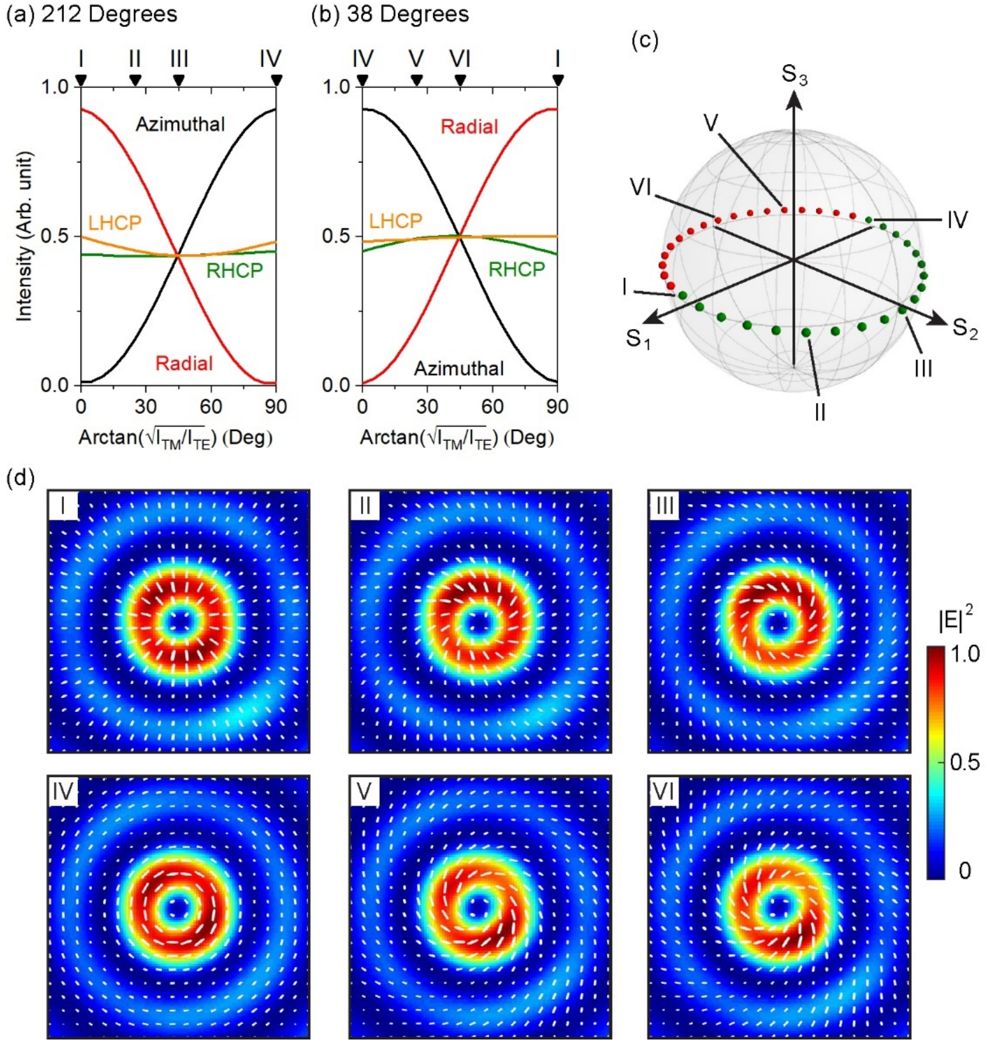

Figure 4.7 Intensity-controlled polarized evolution on the FOPS. (a,b) Intensity decomposition using the linear basis (for the Azimuthal and Radial curves) and the circular polarization basis (for the RHCP and LHCP curves), as arctan $(\sqrt{I_{TM}/I_{TE}})$ scans from 0° to 90°. The input phase contrast $\phi_{TM}-\phi_{TE}$ is (a) 212° and (b) 38°. (c) The scan of arctan $(\sqrt{I_{TM}/I_{TE}})$ shown in (a) and (b) produces polarization states that trace the equator. The green and red dots correspond to $\phi_{TM}-\phi_{TE}$ at 212° and 38°, respectively. (c) The intensity and polarization distribution for the six representative states from I to VI. All the six panels are produced following the same method described in Figure 4.6.

Figure 4.7(a) and (b) show the influence of the input intensity ratio on the four output components (azimuthal and radial components as a pair, and the two circular components as the other pair). Here the input variable is expressed as angle arctan$(\sqrt{I_{TM}/I_{TE}})$, which ranges from 0° to 90°. Figure 4.7(c) shows that, as arctan$(\sqrt{I_{TM}/I_{TE}})$ scans twice from 0° to 90°, with $\phi_{TM}-\phi_{TE}$ first at 212° [Figure 4.7(a)] and then at 38° [Figure 4.7(b)], the polarization of the output beam evolves along the FOPS equator and eventually completes a full great circle of 360°. The two boundary

$\arctan(\sqrt{I_{TM}/I_{TE}})$ values of 0° and 90° correspond to purely TE and purely TM inputs, respectively, which are first analyzed in Figure 4.4. Their polarization distributions shown in Figure 4.7(d) fit well with the results derived from Figure 4.4. Figure 4.7(d) also shows that, the four intermediate $\arctan(\sqrt{I_{TM}/I_{TE}})$ values (i.e. points II, III, V and VI) produce spiral polarizations. For these polarizations, the direction of twist is reversed once $\phi_{TM} - \phi_{TE}$ changes between the two values of 212° (points II and III) and 38° (points V and VI).

4.4.4 Equations for arbitrary FOPS beam generation

The longitudinal and latitudinal scans shown respectively in Figure 4.6 and Figure 4.7 can be generalized to create any polarization state on the FOPS. This arbitrary FOPS beam generation relies on adjusting both input parameters, the intensity ratio I_{TM}/I_{TE} and the phase contrast $\phi_{TM} - \phi_{TE}$, simultaneously. Based on Eqs. (4.3)-(4.6), further assuming that TE and TM inputs generate respectively pure radial and azimuthal polarizations, these two input parameters can be derived from the three SPs as below

$$\frac{I_{TM}}{I_{TE}} = \eta \left| \frac{\psi_{AZ}}{\psi_{RAD}} \right|^2 = \eta \frac{s_2^2 + s_3^2}{(s_1 + 1)^2} \tag{4.8}$$

$$\phi_{TM} - \phi_{TE} = \phi_{AZ} - \phi_{RAD} + \Omega = \arctan\frac{s_3}{s_2} + (1 - \frac{s_2}{|s_2|}) \times 90° + \Omega \tag{4.9}$$

Here, $\eta = 1/2.53$ is the coefficient addressing the difference in the out-coupling efficiency of the TE and TM input modes (i.e. the TE input has to be 2.53 times as strong as the TM input, for the radially polarized output and the azimuthally polarized output to be equal in intensity). $\Omega = 212°$ is one of the two angles used in the equator scan in Figure 4.7. The term of $(1 - S_2/|S_2|) \times 90°$ is incorporated to create a 180° phase flip, so a single phase coefficient Ω is sufficient here, as opposed to the use of two values (i.e. 212° and 38°) in Figure 4.7. This term takes the value of zero at the singularity point of $S_2 = 0$. A key conclusion can be drawn here based on Eqs. (4.8) and (4.9) that, there exists a one-to-one correspondence between a pair of I_{TM}/I_{TE} and $\phi_{TM} - \phi_{TE}$ values and a point on the FOPS.

Equations (4.8) and (4.9) are tested numerically using three sets of SPs that are chosen arbitrarily and listed in Table 4.1. The target SPs are inserted into the two equations to calculate the required input intensity ratio I_{TM}/I_{TE} and the phase contrast $\phi_{TM} - \phi_{TE}$. These two parameters are then used to conduct the numerical simulation, from which the output SPs are extracted. As seen in Table 4.1, the output SPs well reproduce the target values, with the maximal deviation as small as 0.09.

Table 4.1 Three points on the FOPS for testing the two equations on arbitrary FOPS beam generation. The two input parameters lead to output Stokes parameters that aim to replicate the target Stokes parameters. The term Intensity refers to the intensity ratio of I_{TM}/I_{TE}, and Phase to the phase contrast of $\phi_{TM} - \phi_{TE}$.

Test	Target			Coherent input		Output		
	S1	S2	S3	Intensity	Phase (°)	S1	S2	S3
I	0.707	0	0.707	0.068:1	302.00	0.661	0.004	0.749
II	-0.5	-0.707	0.5	1.186:1	356.73	-0.507	-0.653	0.561
III	0.577	0.577	-0.577	0.106:1	167.00	0.574	0.487	-0.655

Figure 4.8 shows the numerically simulated output at the three pairs of I_{TM}/I_{TE} and $\phi_{TM} - \phi_{TE}$, from which the output SPs listed in Table 4.1 are extracted. To provide a further comparison against the target polarization states and identify the source of the discrepancy, Figure 4.8(a) shows corresponding analytical results derived from an ideal device.

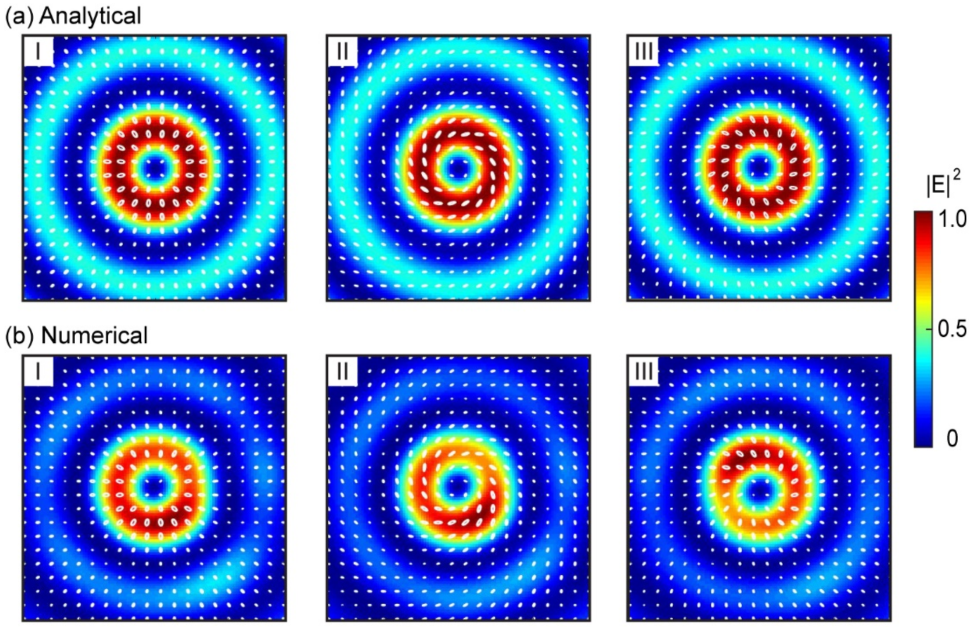

Figure 4.8 Intensity and polarization distributions for the three test FOPS points listed in Table 4.1 with (a) the analytical results compared against (b) the numerical results. All the panels are produced following the same method described in Figure 4.6.

In the ideal device, the 35 nano-holes are assumed to be 35 identical, infinitesimal electric dipoles [208]. Regardless of the input, these dipoles always oscillate in phase to satisfy the angular phase-matching condition specified in Eq. (4.2). Each dipole has a radial component and an azimuthal component, with their relative intensity and phase contrast determined by Eqs. (4.8) and (4.9). As the analytical calculation leads to the ideal output beams seen in Figure 4.8(a), we conclude here that the discrepancy between Figure 4.8(a) and (b) mainly comes from the deviation of the nano-holes from ideal electric dipoles. It is expected that nano-holes with smaller dimensions can better approximate the ideal electric dipoles, albeit at the expense of reduced output efficiency.

For future optimization of this design, as well as for designs that can be derived from this work, we would like to highlight the scope of Eqs. (4.8) and (4.9). The only assumption used in their derivation is that the two fundamental input modes generate pure radial and azimuthal polarizations. Consequently, we believe that these two equations can be applied on any FOPS beam emitter that shares the basic configuration of our device (i.e. any FOPS beam emitter with an angular grating-integrated microring). The matching between the target and the actual polarization states depends on the matching between the grating element and the ideal electric dipole. If the embedded angular grating can be well approximated by a loop of identical, ideal electric dipoles, Eqs. (4.8) and (4.9) can lead to output polarizations that well match the target. For any specific design, the only free parameters are the two coefficients η and Ω, which can be determined following the approach described in Figure 4.4 and Figure 4.6.

4.5 Conclusion

To conclude, we have proposed and numerically analyzed a Si microring resonator-based FOPS beam emitter. The microring is decorated on top with an angular grating of 35 nano-holes, and it evanescently couples to a Si bus waveguide. The nano-hole grating converts TE and TM waveguide modes into free space, as radially and azimuthally polarized cylindrical vector beams, respectively. By using these two linear polarizations as the basis, the SPs of the FOPS are derived. Based on these SPs, a method of producing arbitrary FOPS beams is established. The method utilizes simultaneous control over the relative phase and strength of the two input waveguide modes, and it is underpinned by the fact that there exists a one-to-one correspondence between a pair of these two input parameters and a point on the FOPS.

This work demonstrates that it is possible to produce any FOPS beam with high fidelity on a Si photonics platform. The equations derived from the specific design analyzed in detail here can be applied to any design of FOPS beam emitters, if it shares the generic feature of a microring resonator integrated with an angular grating of dipolar antennas.

Chapter 5 Positive and negative pull-back instabilities from mode splitting in a nano-optomechanical actuator

The vortex beam emitter proposed in Chapter 3 provides a compact solution to obtain tunable OAM modes in the THz frequency range. However, the wavelengths of the emitted OAM modes are predefined and can not be tuned. The wavelength of the emitted VV beam in Chapter 4 is predefined as well. The limitations are because the resonant wavelengths of the microring resonators are fixed. Flexible tunability of the wavelengths of vortex beams is highly desired for high-resolution sensing [21, 26, 209] and high-capacity optical communication [28, 32, 210, 211]. For example, the emitted wave with frequency modulation can enable LiDAR systems to detect the distance and velocity of a moving target simultaneously [7]. In this chapter, we proposed an all-optical wavelength tuning method based on microring resonators. The resonant wavelengths of the device can be tuned by adjusting the pumping wavelength. The approach of wavelength tuning may be combined with the proposed vortex beam emitters in Chapters 3 and 4 to achieve vortex beams with tunable wavelengths.

The device consists of two coupled free-standing waveguides in two identical microrings, fabricated in the silicon-on-insulator process. The coupling between the two microrings results in the symmetric (S-) and antisymmetric (AS-) resonances showing in the transmission spectrum of the device. Pumping the S- and AS-modes can induce attractive and repulsive optical gradient forces, respectively. The optical gradient forces deflect the suspended structures and tune the resonances of the device.

The optical gradient force is related to the pumping wavelength. At some specific pumping wavelengths, a small variation of the wavelengths would significantly change the deflection of the suspended waveguides and pull them back towards their initial positions. The phenomenon is named pull back instability (PBI) [212]. We theoretically and experimentally studied, for the first time, positive and negative pull-back instabilities originating from attractive and repulsive optical gradient forces, respectively. Measuring the wavelength difference between the self-reference S- and AS-resonances can decouple the wavelength tuning due to the optomechanical actuation from the tuning due to the thermo-optical effect. The positive pull-back instability originates from the attractive optical gradient force and results in a significant increase in wavelength difference between the S- and AS-resonances. In contrast, the negative pull-back instability originates from the repulsive optical gradient force and significantly decreases the wavelength difference. Most results in this chapter have been published by the journal "ACS Photonics".

5.1 Optomechanical device based on two coupled microresonators

The device provides a simple actuation scheme for tuning optical resonance, which is useful for optical information processing, such as optical filters. The device consists of two free-standing waveguides in two identical racetrack microrings and a bus waveguide, as shown in Figure 5.1. Each microring has a free-standing waveguide with a length of 50 μm. An air gap between the two suspended waveguides is 190 nm. The air gap between the suspended waveguide and the substrate is about 1.6 μm. The height and width of the suspended waveguides are 220 nm and 450 nm, respectively. Outside the released regions, the waveguides are rib waveguides and have the same cross-section with an overall height of 220 nm, a waveguide width of 450 nm, and an etch depth of 170 nm. The thickness of the Si slab layer is 50 nm. The rib waveguides are used to prevent hydrofluoric acid (HF) vapour etching of the SiO_2 layer outside the released region when releasing the suspended waveguides. The bending radius of the microrings is 30 μm, defined from the middle of the waveguides. The coupling gap between the bus waveguide and the left ring is 210 nm. The coupling length is 2.2 μm for the coupling between the bus waveguide and the left microring.

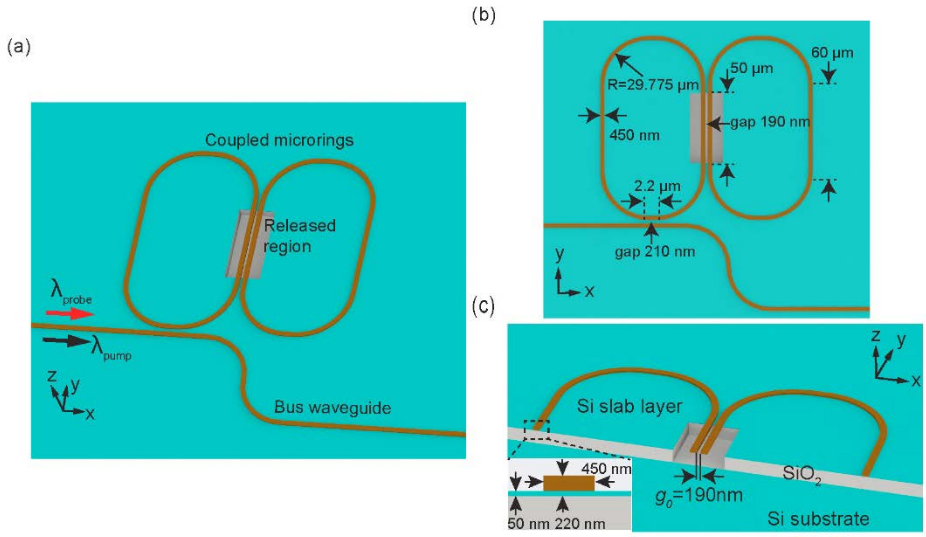

Figure 5.1 Schematic of the optomechanical device. (a) The device contains two laterally coupled microrings and a bus waveguide. Each microring has a free-standing waveguide. The pump light generates optical gradient forces. The probe light detects resonance shifts of the device. (b) Top view of the device. The dimensions of the device are specified. (c) The cross-sectional view of the device. The dimensions of the rib waveguide are shown in the inset.

5.2 Properties of the device

5.2.1 Coupling coefficients

The two microrings are coupled via two parallel waveguides. There are two types of couplers in the coupling region. One is between two suspended waveguides, and another is between two slab waveguides. In the coupling region, the evanescent mode of one waveguide overlaps with the mode of another waveguide. The light transfers back and forth between the two waveguides. The coupled waveguides can support two modes: S- and AS-modes [213]. Figure 5.2 show the S- and AS-modes in the suspended waveguides. The coupling coefficient of the coupling area can be calculated by the effective indices of the two modes [214, 215].

$$K = \frac{\pi}{\lambda}(n_{+} - n_{-}) \tag{5.1}$$

where n_+ and n_- are the effective indices of the S- and AS-modes, respectively. We use K_s and K_c to present coupling coefficients of coupled suspended waveguides and slab waveguides, respectively.

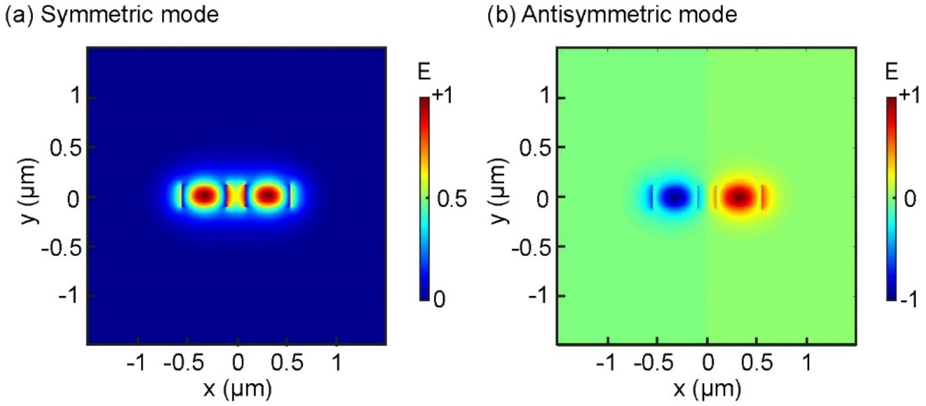

Figure 5.2 Colour map showing the x-component of the electric field for (a) symmetric and (b) antisymmetric modes of the coupled suspended waveguides.

The gap between the two coupled slab waveguides is constant as 190 nm. The effective indices of the S- and AS-modes at λ=1545nm are 2.402 and 2.359, respectively. Therefore, the coupling coefficient K_c is 0.087 rad/μm at λ=1545 nm. The gap between the two suspended waveguides varies when optical gradient forces deflect the waveguides. Figure 5.3 (a) shows the waveguide displacement of the couplers when each waveguide is deflected. The results are simulated using finite-element analysis (FEA) software COMSOL. In the simulation, the exerted forces on the two coupled waveguides are equal but opposite. Each force is uniformly distributed. The maximum displacement of x_{max}=10 nm is shown at the midpoint of each waveguide. Figure 5.3 (b) shows the effective indices of the S- and AS-modes in the suspended waveguides at different gaps. Based on the two effective indices and Eq. (5.1), the coupling coefficient varying with the gap can be obtained, as shown in Figure 5.3(c). The effective coupling coefficient K_{seff} can be obtained by averaging the total coefficient K_s along the whole length of the suspended waveguides (from 5 µm to 55µm in Figure 5.3(a)). Figure 5.3(d) shows the coupling coefficient as a function of the gap between the midpoints of the two suspended waveguides.

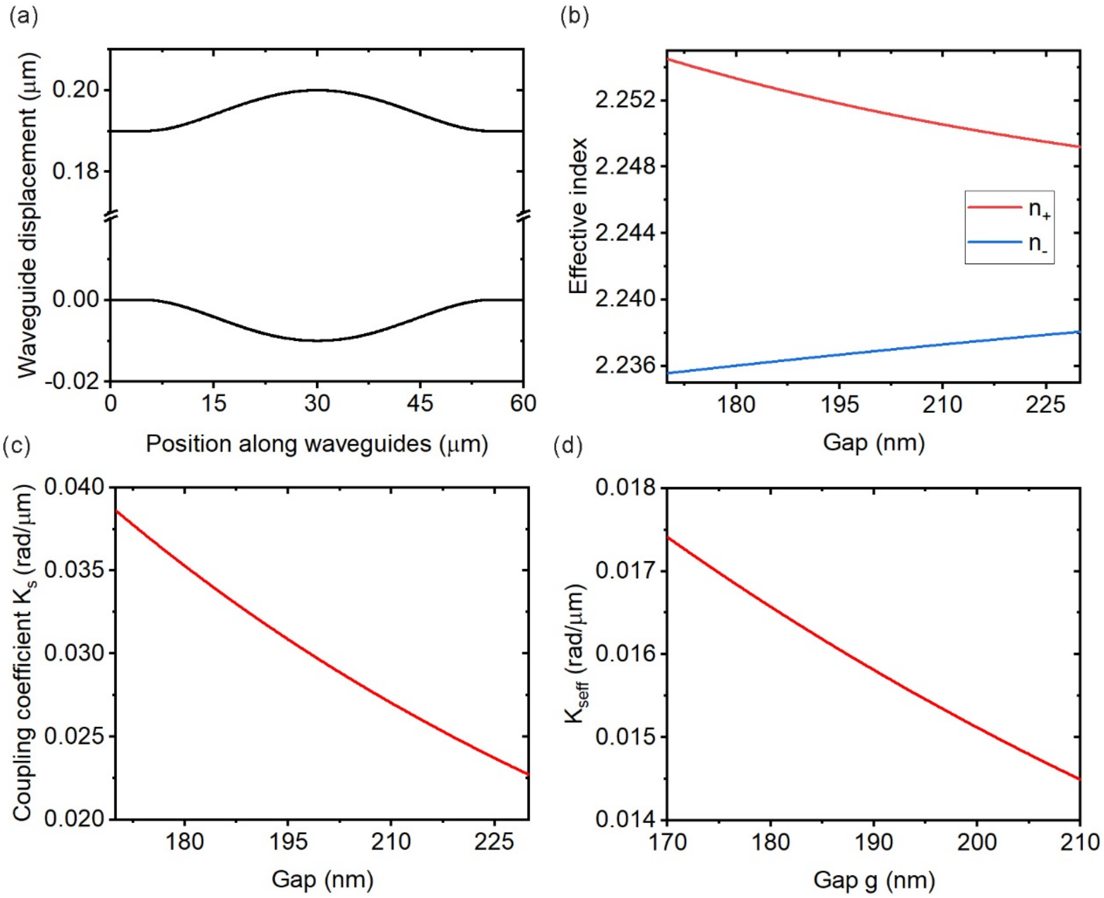

Figure 5.3 Calculation of the coupling coefficiency between the two suspended waveguides. (a) Displacement of each waveguide as a function of position along the waveguide. (b) The effective index of S- and AS-modes in coupled suspended waveguides as gap is varied. (c) The coupling coefficiency as a function of the gap. (d) The effective coupling coefficiency as a function of the gap *g*.

5.2.2 Transmission of the device

The transmission function of the device can be obtained from the device's transfer function that is calculated based on two coupling matrices [216]. One is the coupling matrix to represent the coupling between the bus waveguide and the left microring [217]. Another matrix represents the coupling between the two microrings and is calculated based on the CMT in space [182, 213].

The dotted rectangle shown in Figure 5.4 shows the coupling area containing the suspended waveguides and slab waveguides.

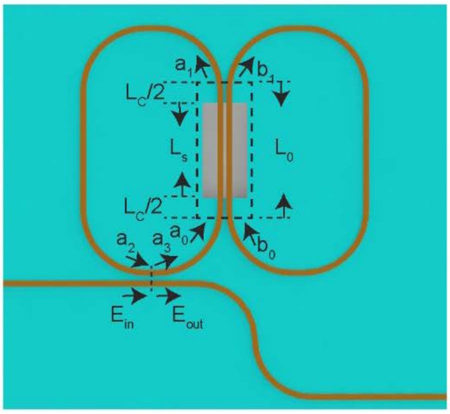

Figure 5.4 Structure of the optomechanical device based on two coupled microrings.

The coupling matrix is

$$\begin{bmatrix} a_1 \\ b_1 \end{bmatrix} = \exp(i\beta L_0 - \alpha L_0) \begin{bmatrix} \cos(KL_0) & i\sin(KL_0) \\ i\sin(KL_0) & \cos(KL_0) \end{bmatrix} \begin{bmatrix} a_0 \\ b_0 \end{bmatrix} \tag{5.2}$$

where a_1, b_1, a_0 and b_0 are the signals at the ports of the coupler. L_0 is the length of the coupling region. β is the effective wave propagation constant in the coupling area. α is the propagation loss.

$$KL_0 = K_{seff} L_s + K_c L_c \tag{5.3}$$

where k_{seff} and k_c are the coupling coefficients in the suspended waveguide and slab waveguide, respectively. L_s and L_c are the lengths of the suspended waveguide and slab waveguide, respectively.

In addition, the following relation between a_1, a_2, b_1 and b_0 exist,

$$a_2 = a_1 \exp(i\beta L_1 - \alpha L_1) \tag{5.4}$$

$$b_0 = b_1 \exp(i\beta L_2 - \alpha L_2) \tag{5.5}$$

The dashed line shown in Figure 5.4 shows the coupling area between the bus waveguide and the left microring. the coupling matrix can be expressed as

$$\begin{bmatrix} a_3 \\ E_t \end{bmatrix} = \begin{bmatrix} \tau & jk \\ jk & \tau \end{bmatrix} \begin{bmatrix} a_2 \\ E_{in} \end{bmatrix} \tag{5.6}$$

where *τ* is the effective field transmission coefficient and *k* the effective field coupling coefficient.

In addition, the following relation between a_0 and a_3 exists,

$$a_0 = a_3 \exp(i\beta L_3 - \alpha L_3) \tag{5.7}$$

Based on the above equations, the signal a_0 can be expressed as

$$a_0 = \frac{-jk\left[\cos(KL_0)\exp(i\beta L_0 - \alpha L_0) - \exp(-i\beta L_2 + \alpha L_2)\right]}{\det\left|A\right|} E_{in} \tag{5.8}$$

where $A = \begin{vmatrix} a_{11} & a_{12} \\ a_{21} & a_{22} \end{vmatrix}$

$$\begin{aligned}
a_{11} &= \tau\cos(KL_0)\exp\left[i\beta(L_0 + L_1) - \alpha(L_0 + L_1)\right] - \exp(-i\beta L_3 + \alpha L_3) \\
a_{12} &= i\tau\sin(KL_0)\exp\left[i\beta(L_0 + L_1) - \alpha(L_0 + L_1)\right] \\
a_{21} &= i\sin(KL_0)\exp\left[i\beta L_0 - \alpha L_0\right] \\
a_{22} &= \cos(KL_0)\exp(i\beta L_0 - \alpha L_0) - \exp(-i\beta L_2 + \alpha L_2)
\end{aligned}$$

By combining Eqs. (5.6)(5.7)(5.8), the field transmission through the bus waveguide can be expressed as

$$t = \frac{jka_0 \exp\left[-i\beta L_3 + \alpha L_3\right]}{\tau E_{in}} + \frac{1}{\tau} \tag{5.9}$$

The squared magnitude of the transmission with different gap *g* is shown in Figure 5.5(a). The value of k_{seff} corresponding to each gap can be obtained from Figure 5.3(d). According to the CMT [218], the left mode is the S-mode, whose resonant wavelength increases with K_{seff}. On the contrary, the right mode is AS-mode, whose resonant wavelength decreases with K_{seff}. Figure 5.5(b) shows the variation of the S- and AS-resonances when the gap *g* changes.

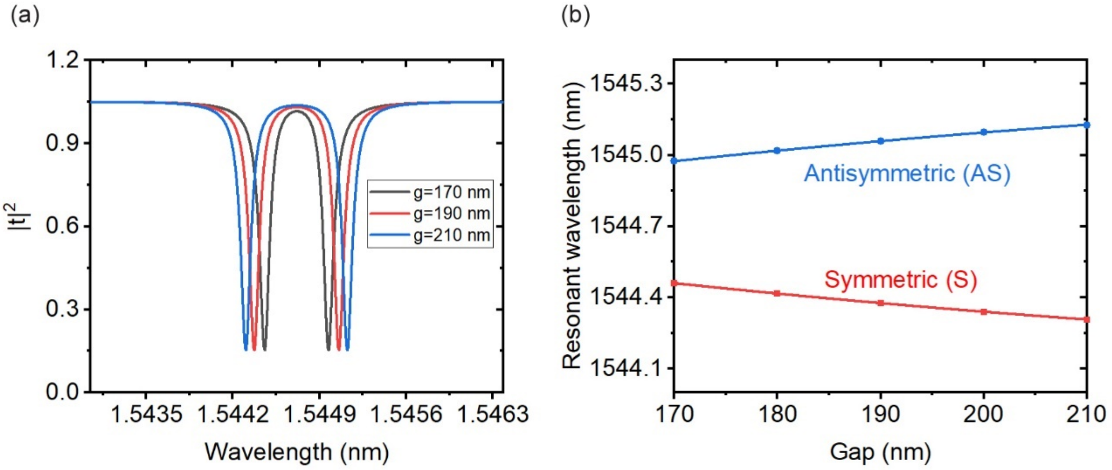

Figure 5.5 Transmission properties of the optomechanical device. (a) Transmission spectra with different gap g. (b) Variation of the two resonances (S- and AS-resonances) as the gap *g* changes.

5.2.3 Stored energy in the device

The energy stored in the device can be analysed by using the CMT in the time domain. Here, we treat the two coupled resonators as a resonator. The coupling of the mode in the bus waveguide and the mode in the resonator can be expressed as [181, 183]

$$\frac{da}{dt} = (j\omega_0 - 1/\tau_i - 1/\tau_c)a - jkS_{in} \tag{5.10}$$

$$S_{out} = S_{in} - jka \tag{5.11}$$

where *a* denotes the amplitude of the travelling mode in the resonator. ω_0 is the resonator frequency for the mode a. $1/\tau_i$ denotes the intrinsic loss of the resonator. $1/\tau_c$ is the decay rate of the coupling between the bus waveguide and the resonator. The waveguide/ring coupling coefficient and the power decay rate are related by $|k|^2 = 2/\tau_c$. S_{in} is the incident mode amplitude in the bus waveguide.

The amplitude of the travelling mode in the resonator can be expressed as

$$a = \frac{-jkS_{in}}{j(\omega-\omega_0)+1/\tau_i+1/\tau_c} \tag{5.12}$$

The transfer function can be given as

$$t = \frac{S_{out}}{S_{in}} = \frac{j2(\omega-\omega_0)/\omega_0 + 1/Q_i - 1/Q_c}{j2(\omega-\omega_0)/\omega_0 + 1/Q_i + 1/Q_c} \tag{5.13}$$

where $Q_i = w_0\tau_i/2$ is the intrinsic *Q* factor of the device, $Q_c = w_0\tau_c/2$ is the Q factor for the waveguide-resonator coupling. The quality factor can be obtained by fitting experimental data with Eq. (5.13). Figure 5.6(a) shows that the intrinsic quality factor Q_i is 35310, and the coupling quality factor Q_c is 28660. In Figure 5.6 (b), the intrinsic quality factor Q_i is 25120, the coupling quality factor Q_c is 25120.

The energy stored in the resonator can be represented by $|a|^2$,

$$|a|^2 = \frac{2/\tau_c}{(\omega-\omega_0)^2 + (1/\tau_i + 1/\tau_c)^2} P_{in} = \frac{2/\tau_c}{(\lambda-\lambda_0)^2 (2\pi c)^2 (\lambda_0)^{-2} + (1/\tau_i + 1/\tau_c)^2} P_{in} \quad (5.14)$$

where $|S_{in}|^2 = P_{in}$ is the pump power in the bus waveguide.

Figure 5.6(c)(d) shows the calculated results for the energy spectrum of the resonator around the resonant wavelengths of 1.54558 and 1.54621 μm, respectively. The pump power is 7.5 dBm.

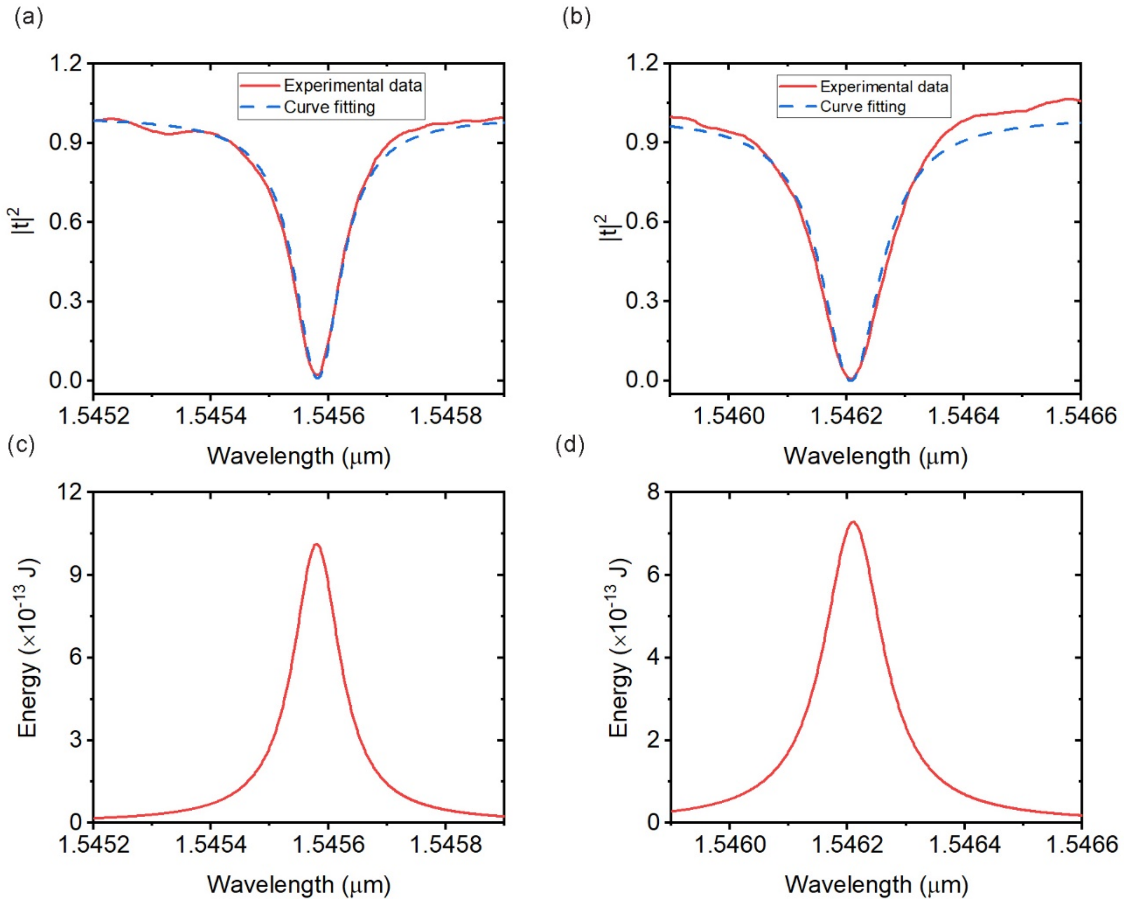

Figure 5.6 Calculation of stored energy in the optomechanical device when pump power is 7.5 dBm. (a) Curve fitting using Eq. (5.13) for one measured notch around 1.5458 μm. (b) Curve fitting using Eq. (5.13) for one measured notch around 1.5462 μm. (c) Calculated energy of the resonator when the pump is from 1.5452 μm to 1.5459 μm. (d) Calculated energy of the resonator when the pump is from 1.5459 μm to 1.5466 μm.

5.2.4 Thermal effect of the device

In this section, the heat dissipation characteristics of the optomechanical device will be studied by using COMSOL. At room temperature, the thermal conductivity of bulk Si is 148 W/(m·K). However, the thermal conductivity of a silicon layer is a function of thickness at room temperature [219]. Figure 5.7(a) shows the thermal conductivity for different thicknesses of a Si layer. In the designed device, Si layers with thicknesses of 50 nm and 220 nm are used. According to Figure 5.7(a), we choose the thermal conductivities as 44 W/(m·K) and 99 W/(m·K), respectively. The thermal conductivities of SiO_2 and air are 1.4 W/(m·K) and 0.026 W/(m·K), respectively. It can be seen that the Si material is a better thermal conductor than SiO_2 and air. The steady-state distribution of the temperature over a microring is shown in Figure 5.7(b).

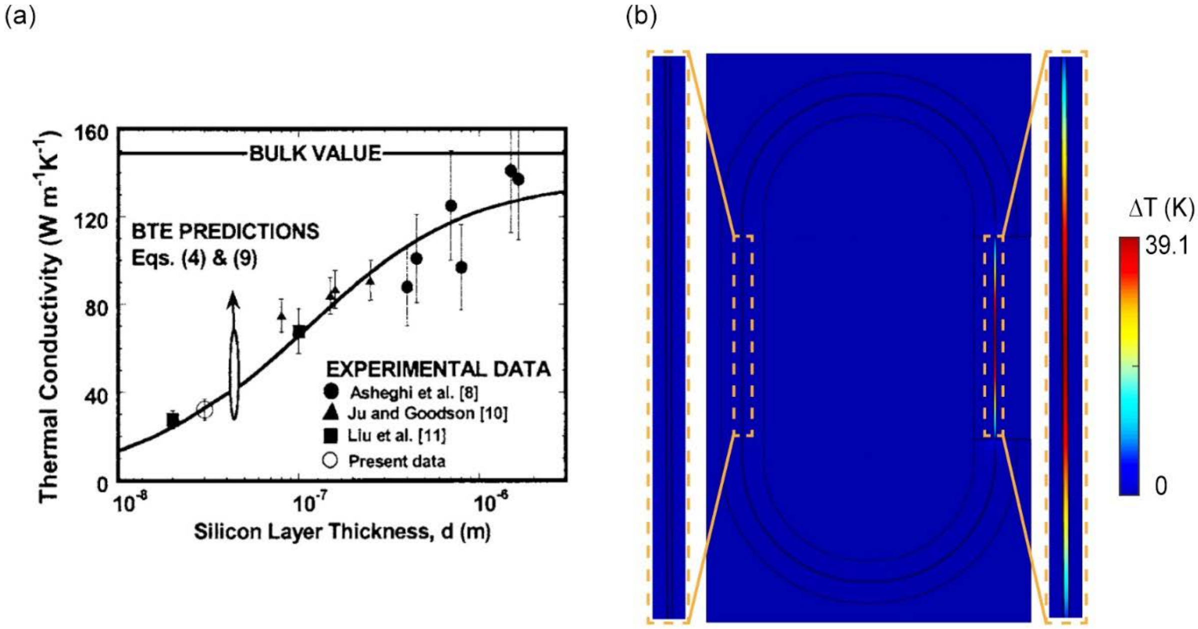

Figure 5.7 Thermal property of the optomechanical devices. (a) Thermal conductivity of silicon layers as a function of thickness [219]. (b) Steady-state distribution of the temperature change over a microring. The left inset is a zoomed-in view of the temperature change in the straight slab waveguide. The right inset shows the zoomed-in view of the temperature change in the suspended waveguide. A heat source with a uniform density of 10^{13} W/m^3 is used in the microring core.

In the simulation, we set a constant uniform heat source with a density of 10^{13} W/m^3 in the Si waveguides. The heat source represents the thermal effect of the optical absorption when the device is pumped. Only one microring is simulated, considering the memory requirement for the 3D simulation. The other microring will have the same temperature distribution because the two microrings are the same. It can be seen that the temperature change of the free-standing waveguide is larger than that of the slab waveguide. The average temperature change of the whole

Si microring is 4.72 K. The total heat flux is 6.19×10^{-4} W for the two Si microrings. Therefore, the thermal resistance of the coupled Si microrings is about 7625 K/W.

5.2.5 Mechanical spring constant of the suspended waveguides

The mechanical spring constants of the suspended waveguides are calculated by using 3D solid mechanical simulation of COMSOL. For simplicity, we assume that the force exerted on each waveguide is uniformly distributed. Figure 5.3(a) shows the deflection of the two suspended waveguides when applying 6.6 nN on each suspended waveguide. The forces on the two waveguides have equal magnitude but opposite directions. The maximum deflection of each waveguide x_{max} is 10 nm. Figure 5.8 shows the variation of x_{max} when the exerted forces are changing. It can be observed that x_{max} is proportional to the force. The mechanical spring constant of each waveguide is $k_{mech}=F/x_{max}$=0.66 N/m.

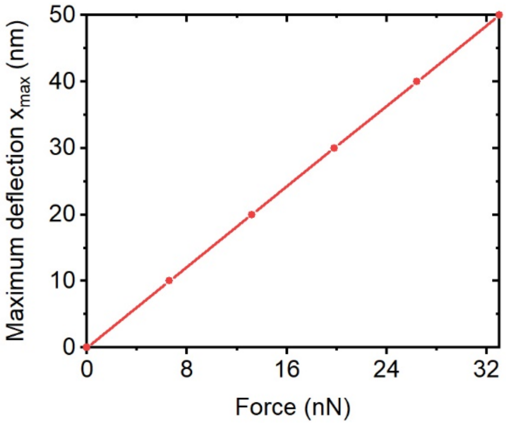

Figure 5.8 Maximum waveguide deflection versus the total force exerted on the waveguide.

5.3 Calculation of optical gradient forces and resonance shifts of the device

In this section, the wavelength tuning of the optomechanical device will be theoretically analyzed. The two microrings of the designed device are identical and coupled. The degeneracy of the resonator modes is broken, and the mode pairs (S- and AS-modes) appear [218, 220]. Figure 5.9 shows the variation of S- and AS-resonances with the air gap between the two suspended waveguides. The insets show the electric field profiles for the S- and AS-modes. The S- and AS-resonances depend on the gap of the two rings. The difference between the two resonant wavelengths is defined as the splitting width, which increases when the gap increases. Strictly speaking, the splitting width is the wavelength difference between the S- and AS-resonances with the same azimuthal order. Here, we use the splitting width to present the wavelength difference between two neighbouring modes without considering the requirement of the same azimuthal order. It is worth noting that the two neighbouring modes shown in Figure 5.9 have different azimuthal orders due to the strong coupling causing the splitting spanning more than one free spectral range of the device. The calculated resonances shown in Figure 5.9 are obtained from Figure 5.5.

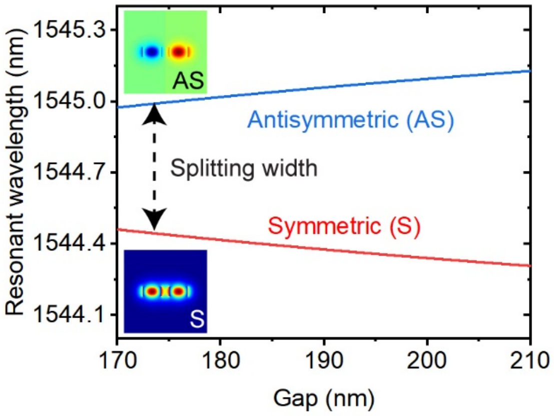

Figure 5.9 Simulated variation of the S- and AS-resonances as the air gap between two suspended waveguides is changed. The coupling between the two microrings is so strong that the wavelength splitting spans more than one free spectral range of the device. So the two neighbouring modes (S- and AS-modes) shown in the figure have different azimuthal orders. The insets show the electric field profiles for the S- and AS-modes.

The overlapping modes of the two coupled waveguides give rise to optical gradient forces. Each waveguide provides a strong field gradient in the near-field. A waveguide can be considered as a collection of individual microscopic dipolar subunits. The dipoles' positively and negatively charged sides will experience slightly different forces in the strongly varying electromagnetic field. Consequently, the waveguide is accelerated and displaced [221]. The optical gradient forces can be calculated by integrating the Maxwell stress tensor over a closed surface surrounding the waveguide [207, 221]. Alternatively, the optical gradient force can be derived from the change in the eigenmode frequency of the waveguide system when the two waveguides move [222]. The change in eigenmode frequency causes a change in the total system energy, which is equal to the work done by the beams. Therefore the optical gradient force can be expressed as

$$F=-\frac{dU}{dx}\Big|_{\boldsymbol{k}}=-\frac{1}{\omega}\frac{d\omega}{dx}\Big|_{\boldsymbol{k}}U \tag{5.15}$$

where x is the distance between the beams, U is the total system energy, and $\boldsymbol{k}$ is the wave vector, which is conserved.

Combining Eq. (5.14) and Eq. (5.15), the optical gradient forces can be expressed as [212]

$$F_{opt}^{\pm}=-\frac{\partial U^{\pm}}{\partial g}=\frac{2(\tau_e^{\pm})^{-1}P_{in}}{(\lambda_{in}-\lambda_r^{\pm})^2(2\pi c)^2(\lambda_r^{\pm})^{-3}+\lambda_r^{\pm}((\tau_i^{\pm})^{-1}+(\tau_e^{\pm})^{-1})^2}\frac{\partial\lambda_r^{\pm}}{\partial g} \tag{5.16}$$

where U is the optical energy stored in microrings, ∂g represents the variation of the gap when the two suspended waveguides bend. The gap is between the midpoints of the two suspended waveguides. P_{in} is the power of the control light in the bus waveguide, λ_{in} is the wavelength of the control light, λ_r is the resonant wavelength, τ_i is the decay rate due to the internal loss, τ_e is the decay rate due to the coupling between the microring and the bus waveguide, $\partial\lambda_r/\partial g$ is the optomechanical tuning efficiency. The superscript ± stands for either the S- (+) or AS- (-) optical mode.

The resonant wavelengths in Eq. (5.16) are given by

$$\lambda_r^{\pm}=\lambda_{r0}^{\pm}+\delta\lambda_{om}^{\pm}+\delta\lambda_{to}^{\pm} \tag{5.17}$$

where λ_{r0} is the unshifted resonant wavelength, $\delta\lambda_{om}$ is the resonance shift due to the optomechanical actuation. $\delta\lambda_{to}$ is the resonance shift induced by the thermo-optical effect. The resonance shift due to the optomechanical actuation can be written as

$$\delta\lambda_{om}^{\pm}=\Delta g\cdot\partial\lambda_r^{\pm}/\partial g \tag{5.18}$$

where Δg is the change of the gap due to the optical gradient force. The gap is between the midpoints of the two suspended waveguides. The resonance shift due to the thermo-optical effect can be expressed as [223-225]

$$\delta\lambda_{to}^{\pm}=\lambda_{r0}^{\pm}/n_g\cdot k_{th}\Delta T \tag{5.19}$$

where n_g is the group index, and $k_{th}=1.86\times10^{-4}\ \mathrm{K}^{-1}$ is the silicon thermo-optic coefficient. ΔT is the steady-state temperature change in the microrings. It can be expressed as [226, 227] $\Delta T=\Gamma_{abs}R_{th}U^{\pm}$, where Γ_{abs} is the total optical absorption rate, R_{th} is the thermal resistance of the microrings.

The optomechanical tuning coefficient $\partial\lambda_r/\partial g$ in Eq. (5.16) can be obtained from Figure 5.9. In the device, the initial gap is 190 nm, $\partial\lambda_r^{\pm}/\partial g=\mp3.8\times10^{-3}$. Based on Eq. (5.16), Pumping the S-mode can generate the attractive optical gradient force that pulls the two suspended waveguides towards each other. On the contrary, pumping the AS-mode can generate the repulsive optical gradient force that pushes the two waveguides away from each other.

The deflection of the two waveguides gives rise to a mechanical force $F_{mech}=k_{mech}\cdot\Delta g/2$. k_{mech} is the spring constant of a suspended waveguide. The mechanical spring constant is simulated to be 0.66 N/m in Section 5.2.5. Compared to the optical gradient forces, the mechanical force tends to pull the waveguides to their original positions. The optical force and the mechanical force balance each other at the equilibrium point,

$$F_{opt}(\Delta g)+k_{mech}\cdot\Delta g/2=0 \tag{5.20}$$

The balance between the mechanical forces and the optical gradient forces are numerically analyzed. The pump power in the simulation is P_{in}=7.5 dBm. The parameters for calculating the stored energy U are described in Section 5.2.3. For the S-mode, the resonant wavelength is λ_{r0}^{+}=1545.58 nm, the intrinsic Q factor of the coupled microrings is $Q_i=\omega_{r0}^{+}\tau_i/2$=35310, and the Q factor for the waveguide-resonator coupling is $Q_e=\omega_{r0}^{+}\tau_e/2$=28660. For the AS-mode, the resonant wavelength is λ_{r0}^{-} =1546.21 nm, the intrinsic Q factor of the coupled microrings is $Q_i=\omega_{r0}^{-}\tau_i/2$=25120, and the Q factor for the waveguide-resonator coupling is $Q_e=\omega_{r0}^{-}\tau_e/2$=25120. The thermal resistance between the coupled microrings and the surroundings is R_{th}=7625 K/W, described in 5.2.4. The optical absorption rate Γ_{abs} is estimated using the absorption limited quality factor $Q_{abs}=\omega/\Gamma_{abs}$ [226], where $Q_{abs}=10^6$ [228, 229].

Figure 5.10(a) shows the balance between the mechanical force and the attractive optical gradient force. The detuning Δ is defined as the difference between the pump laser wavelength and the unshifted S-resonance λ_{r0}^{+}=1545.58 nm. $\Delta=\lambda_{in}$-1545.58 nm. The gap change in Figure 5.10 means the change in the gap between the midpoints of the two suspended waveguides when the waveguides are deflected from their initial positions. The initial gap is 190 nm. When Δ increases, the equilibrium point changes from point a to point c, and the gap decreases with the pump laser wavelength. It is because the pump laser approaches the S-resonance(λ_{r}^{+}), more power is stored in the microrings, increasing the generated attractive force. At point c, the deflection is the largest. This means the pump laser wavelength is the same as the S-resonance λ_{r}^{+}. When Δ increases, the equilibrium point changes from point c to d. The gap significantly increases, and the suspended waveguides are pulled back towards the initial positions. This phenomenon is called PBI [212]. We name it positive PBI (pPBI) to distinguish it from the one caused by the repulsive optical gradient force.

Figure 5.10(b) shows the balance between the repulsive optical gradient force and the mechanical force. The detuning is defined as the difference between the pump laser wavelength and the unshifted AS-resonance λ_{r0}^{-}=1546.21 nm. $\Delta=\lambda_{in}$-1546.21 nm. It is observed that the gap increases with the pump laser wavelength when the equilibrium point changes from e to g. At point g, the gap is the largest. When Δ increases, the equilibrium point changes from g to h. The gap decreases significantly, and the two suspended waveguides are pulled back towards their initial positions. Here, we use negative PBI (nPBI) to describe the significant decrease of the gap.

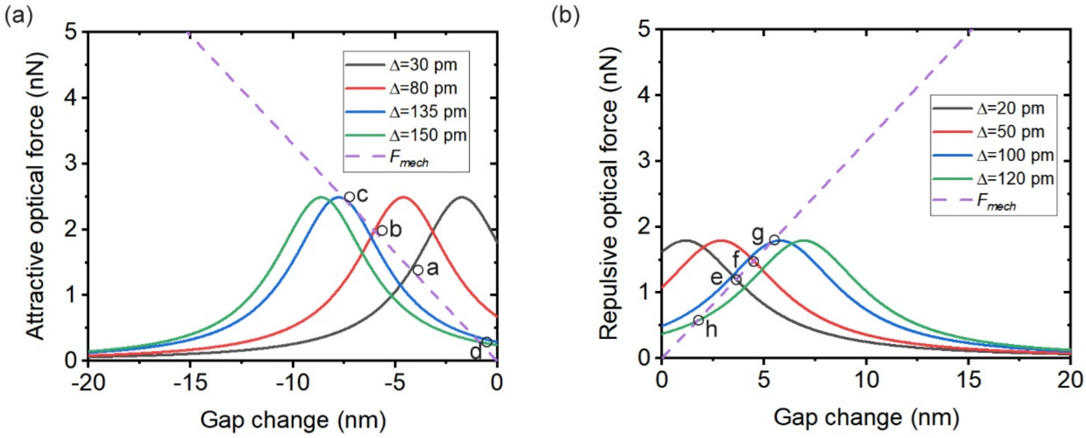

Figure 5.10 Calculation of optical gradient forces of the device. (a) Comparison of the simulated mechanical force and attractive optical gradient force. Δ= λ_{in}-1545.58 nm. 1545.58 nm is the measured S-resonance (λ_{r0}^{+}). (b) Comparison of the simulated mechanical force and repulsive optical gradient force. Δ= λ_{in}-1546.21 nm. 1546.21 nm is the measured AS-resonance (λ_{r0}^{-}).

Figure 5.11 presents the nonlinear variation of the gap as the pump wavelength increases from 1545.35 nm to 1546.45 nm. The range of the pump laser wavelength covers an S-resonance (λ_{r0}^{+}=1545.58 nm) and an AS-resonance (λ_{r0}^{-}=1546.21 nm). It is observed that there are four main changes (Indicated using Region I, II, III and IV) of the gap. Region I and II show that the gap changes when the S-mode is pumped. In Region I, The gap decreases when the pump wavelength increases. In region II, a small increase in the pump laser wavelength induces a significant increase in the gap, indicating the occurrence of pPBI. Region III and IV show that the gap changes when the AS-mode is pumped. In region III, the gap increases with the pump laser wavelength. In region IV, a significant decrease in the gap is caused by a small increase in the pump laser wavelength, showing the occurrence of the nPBI.

According to Figure 5.9, the variation of the gap shown in Figure 5.11 gives rise to changes in the splitting width. Figure 5.11 also shows the nonlinear changes of the splitting width when the pump wavelength increases.

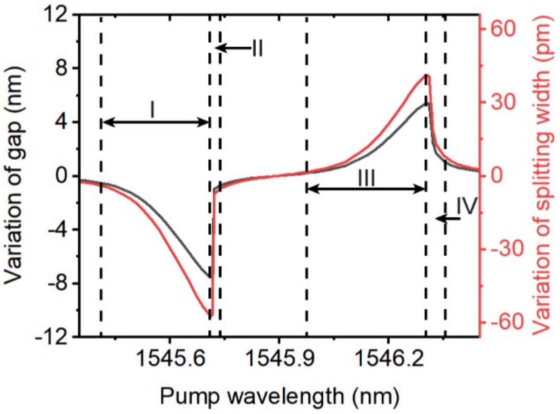

Figure 5.11 Simulated nonlinear variations of the air gap between the two suspended waveguides. The pump laser wavelength increases from 1545.35 nm to 1546.45 nm. The range (1545.35-1546.45 nm) covers an S-resonance (λ_{r0}^{+}=1545.58 nm) and an AS-resonance (λ_{r0}^{-}=1546.21 nm). The simulated nonlinear changes of the splitting width between the S- (λ_{r0}^{+}) and AS- (λ_{r0}^{-}) resonances are also presented.

5.4 Fabricated device and experimental setup

5.4.1 Fabrication process

The optomechanical device shown in Figure 5.1 is fabricated in an SOI process to demonstrate the wavelength tuning and PBIs induced by the attractive and repulsive optical gradient forces. The fabrication is processed at the Southampton Nanofabrication Centre. The whole fabrication consists of four parts, including the fabrication of rib waveguides, the fabrication of strip waveguides, the fabrication of grating couplers and the fabrication of suspended waveguides. The detailed process will be described in the following sections.

5.4.1.1 Fabrication of the rib waveguides

The slab waveguides contain the structures of the coupled microrings and bus waveguides. Figure 5.12 shows the fabrication process. Step (a) is the preparation of an SOI wafer. This wafer has a 220 nm thick silicon layer with a 2-µm-thick buried oxide layer. Step (b) is the deposition of a thin silicon oxide layer (40 nm) as a hard mask on top of the silicon layer using plasma-enhanced chemical vapour deposition (PECVD). This hard mask is to ensure the waveguides has a good profile and reduce optical loss. Step (iii) contains lithography steps. The resist of ZEP520A (300nm) is coated on the surface of the wafer. Electron beam lithography (EBL) is used to transfer the designs to the resist layer. In step (iv), the resist pattern is used as a maks for inductively coupled plasma (ICP) etching. The etching thickness of the Si layer is 170nm. The gases used for etching are sulfur hexafluoride and octafluorocyclobutane. After etching, the resist left on top of the structure is removed using a Plasma asher at step (v).

i. SOI wafer

ii. PECVD SiO_2

iii. E-beam lithography

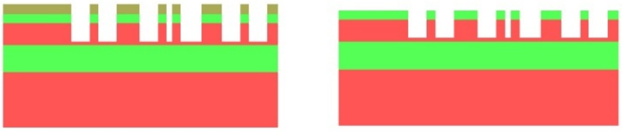

iv. ICP etching

v. Resist removal

Figure 5.12 Fabrication process of the rib waveguides of the optomechanical device.

5.4.1.2 Fabrication of the strip waveguides

This fabrication is to obtain the strip waveguides, which will be used as suspended waveguides. Figure 5.13 shows the detailed fabrication process. In step (i), EBL is used to define the patterns on the resist layer. Then the patterned resist layer is used as a mask for the ICP etching in step (ii). The etching depth into Si is 50nm. So the buried oxide layer is exposed. In step (iii), a Plasma asher is used to strip the left resist on the surface of the SOI wafer.

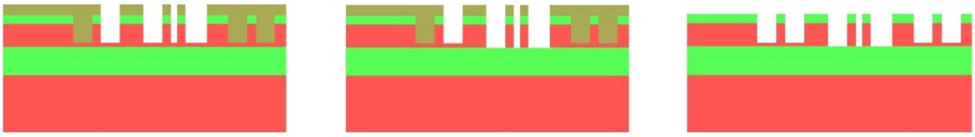

i. E-beam lithography

ii. ICP etching

iii. Resist removal

Figure 5.13 Fabrication process of the strip waveguides of the optomechanical device.

5.4.1.3 Fabrication of the grating couplers

Grating couplers of the devices are obtained in this fabrication process. In experiments, the light will be coupled in and out of the waveguides by the couplers. Figure 5.14 shows the detailed fabrication process. In step (i), EBL is used to define the patterns on the resist layer. Then the patterned resist layer is used as a mask for the ICP etching in step (ii). The etching depth into Si is 70nm. A Plasma asher is used to strip the left resist on the surface of the SOI wafer in step (iii).

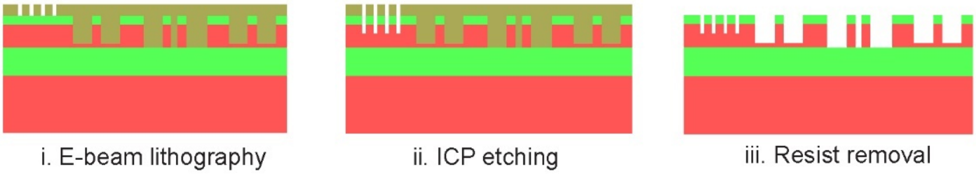

Figure 5.14 Fabrication process of the grating couplers of the optomechanical device.

5.4.1.4 Fabrication of the suspended waveguides.

The last fabrication process, shown in Figure 5.15, releases the strip waveguides and obtains the suspended waveguides. The oxide under the striped waveguides is removed by HF vapour. Meanwhile, the hard mask of SiO_2 is removed as well. The concentration of HF solutions is 40%, and the temperature for etching is 48°C.

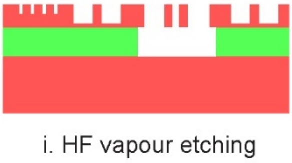

Figure 5.15 Fabrication process of the suspended waveguides of the optomechanical device.

The SEM image of the fabricated device after HF vapour etching is shown in Figure 5.16(a). In the coupling region between the bus waveguide and the left microring, two arrows in Figure 5.16(a) show that light couples in and out of the microring with the power coupling efficiency *k*. The efficiency is 27% when the wavelength is 1545.58 nm. The dashed rectangles indicate the regions shown in Figure 5.16(b)(c). Figure 5.16(b) shows the connection between the suspended waveguides and the rib waveguides. Figure 5.16(c) shows the central region of the two coupled suspended waveguides.

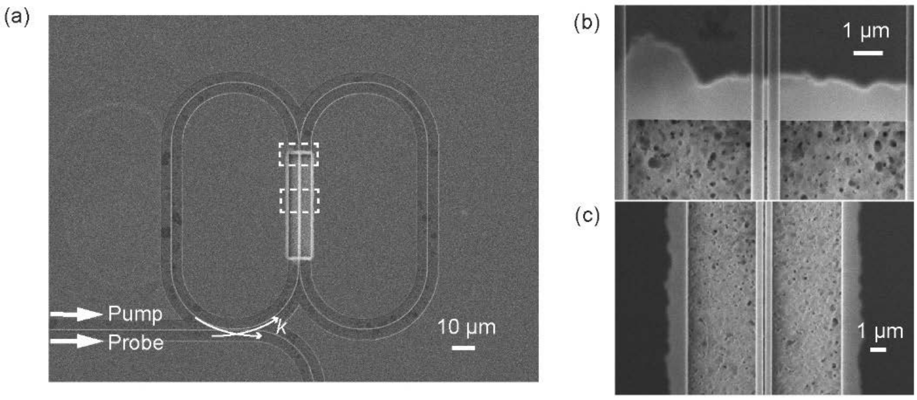

Figure 5.16 SEM image of the fabricated nano-optomechanical device. (a) This device includes two coupled microrings and a bus waveguide. Each microring has a free-standing waveguide. The two dashed rectangles indicate the regions shown in (b) and (c). (b) SEM image of the connections between the rib waveguides and the suspended waveguides. (c) SEM image of the centre region of the suspended waveguides.

5.4.2 Experimental setup

The schematic of the experimental setup used to measure the transmission spectra of the coupled microrings is illustrated in Figure 5.17.

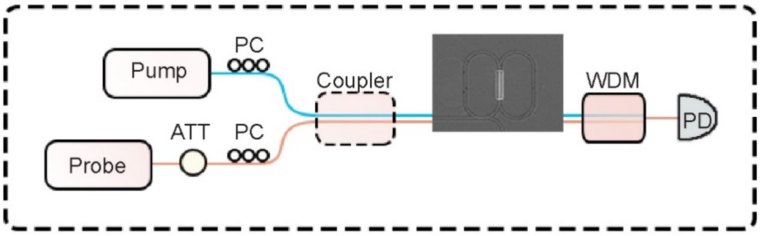

Figure 5.17 Schematic of the experimental setup. The pump light is used to control optical forces, and the probe light is used to read out shifts of the device's resonances. The pump and probe are coupled using an optical coupler and launched into the bus waveguide. A wavelength division multiplexer is used to filter the pump light. The optical transmission spectrum is obtained from the photodetector that is synchronized with the probe light source.

The pump laser is high-power and utilized to induce optical gradient forces to deflect the two suspended waveguides. The low-power probe laser sweeps in wavelength to read out the resonance shift of the device. An attenuator (ATT) is used to reduce the power of the probe laser. A polarization controller (PC) is used after each laser to excite transverse electric mode in the device. The pump and probe are coupled using an optical coupler (OC) and launched into the bus waveguide. The output pump and probe are separated by a wavelength division multiplexer (WDM). A photodetector (PD) is synchronized with the probe laser to record the probe transmission.

The photo of the experimental setup is shown in Figure 5.18. The pump light is from Pure Photonics PPCL550 laser, and the probe light is from the Keysight 81940A laser. The optical coupler is Thorlabs 10202A-50-APC. The microscope is utilized to check the positions of fibres and grating couplers. The 3-axis stages are used to achieve the alignment between the fibres and grating couplers. So the pump and probe can be coupled in and out of the device. The WDM is Thorlabs WD1525A. The probe light is detected by Keysight 81634B power sensor.

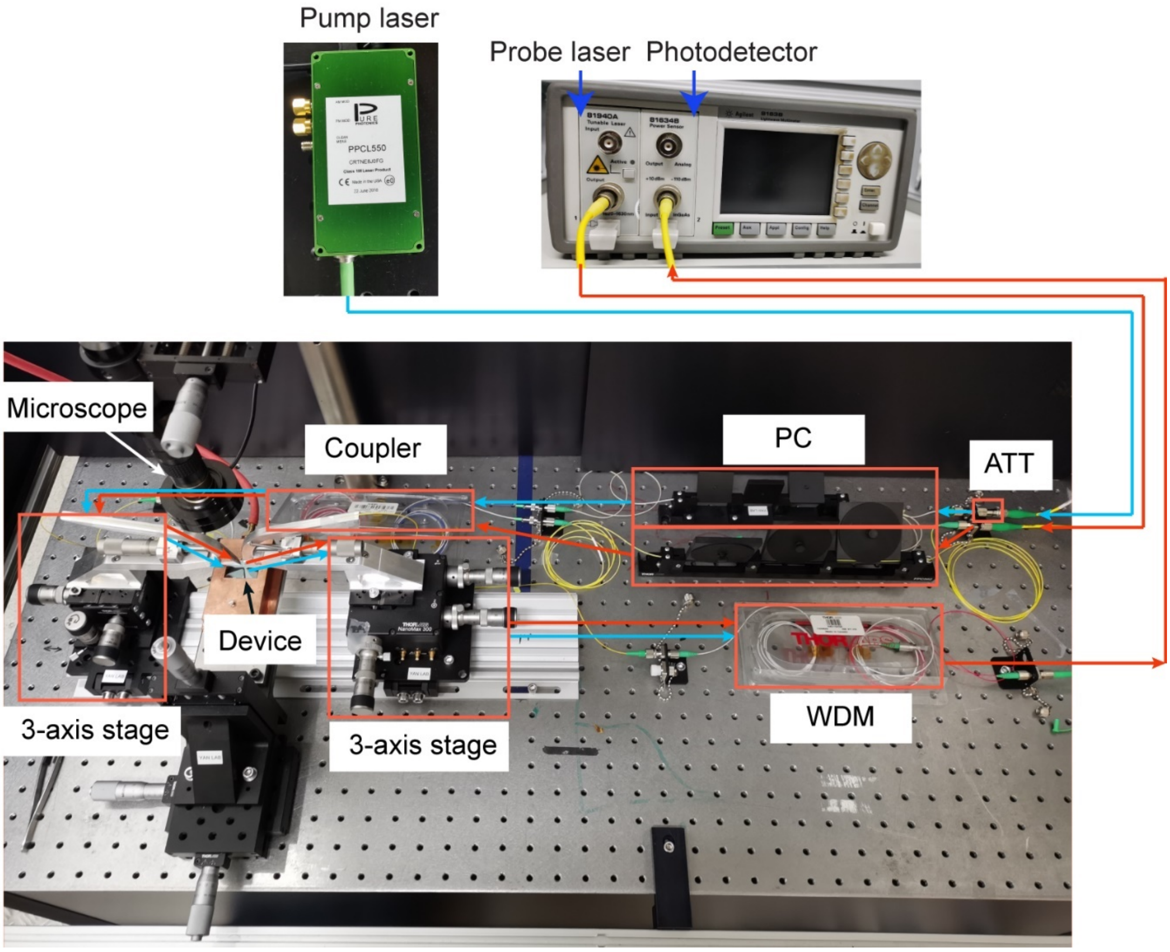

Figure 5.18 Picture of the experimental setup.

5.5 Experimental results

5.5.1 Shifts of split resonances when the device is pumped

Figure 5.19 presents the transmission spectrum of the device using the probe laser in the bus waveguide. The split notches in the transmission indicate the occurrence of mode splitting. The S- and AS-modes can be identified based on FSR [226]. The measured FSRs for the split modes are shown in Figure 5.19. The FSR for the left mode in the pump scan region (Orange region) is 1.814 nm, and the FSR for the right mode in the region is 1.804 nm. The larger FSR indicates that the left mode in the region is S-mode and the right mode in the region is AS-mode. The theoretical values of the FSRs of the S- (1545.58 nm) and AS- (1546.21 nm) resonances are 1.800 nm and 1.790 nm, respectively, [180] matching well with the FSRs obtained directly from Figure 5.19. For the two modes in the probe scan region (Blue region), the left mode with the FSR of 1.853 nm is recognized as the S-mode. The right mode with the FSR of 1.842 nm is the AS-mode. In the experiments, the pump wavelength is increased in the pump scan region and induces optical gradient forces. In the probe scan region, the probe transmission is recorded to measure the resonance shifts.

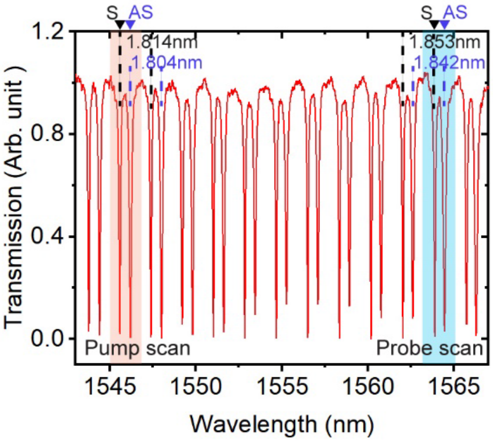

Figure 5.19 The transmission spectrum when only the probe light is used. The orange region highlights the pump scan region (1545.35-1546.45 nm). The blue region (1563.3-1565 nm) highlights the probe scan region.

Pumping the device will induce the optomechanical actuation and thermo-optical effect. The S- and AS-resonances will be shifted by the two effects. The optomechanical actuation changes the gap between the two microrings. The optical coupling coefficient between the two microrings depends exponentially on the gap. According to Figure 5.9, increasing the gap will blue shift the S-mode and red-shift the AS-modes while decreasing the gap will red-shift the S-mode and blue-shift the AS-mode. For the shifts of the S-and AS-resonances due to the thermo-optical effect, their ratio can be calculated based on Eq. (5.19). The ratio is $\delta\lambda_{to}^{+}/\delta\lambda_{to}^{-} = (\lambda_{r0}^{+}/n_g^{+})/(\lambda_{r0}^{-}/n_g^{-}) = 1$, where

λ_{r0}^{+}=1545.58 nm, λ_{r0}^{-}=1546.21 nm. n_g^{+}/n_g^{-} is calculated based on the FSRs (1.814 nm for the S-mode and 1.804 nm for the AS-mode) [180]. The ratio of 1 means the thermo-optical effect lead to the same shifts of the S-and AS-resonances.

In Figure 5.20(a), the S-mode in the pump scan region is pumped. The transmission with pump laser wavelength of 1545.35 nm is for reference as no pump power drops into the microrings. When the pump laser wavelength changes by 310 pm from 1545.35 nm to 1545.66 nm, It is measured that the S-resonance is red-shifted by 97 pm, and the AS-resonance is red-shifted by 51 pm. The red-shifts of the S- and AS-resonances indicate that the thermo-optical effect dominates the wavelength tuning. If the optomechanical actuation dominates, one resonance will be red-shifted, and another will be blue-shifted. It is also observed that the S-resonance has a larger shift compared to the AS-resonance. This is because the attractive optical gradient force is induced by pumping the S-mode in the pump scan region, decreasing the gap between two microrings and causing the red-shift of the S-resonance and the blue-shift of the AS-resonance. When the pump laser wavelength increases by 20 pm from 1545.66 nm to 1545.68 nm, both the S- and AS-resonances experience significant decreases. When the pump laser wavelength is 1545.68 nm, the resonances in the probe scan region are very close to the reference resonances with no pump power dropping into the microrings. This means the two suspended waveguides are almost pulled back to their initial positions, and the pPBI occurs.

In Figure 5.20(b), the AS-mode in the pump scan region is pumped. The transmission with pump laser wavelength of 1546 nm is for reference as no pump power drops into the microrings. When the pump laser wavelength increases from 1546 nm to 1546.29 nm, both the S- and AS-resonances are red-shifted, indicating that the thermo-optical effect dominates the wavelength tuning. Compared to the S-resonance, the AS-resonance has a larger wavelength shift. This is because the repulsive optical gradient force increases the gap between the microrings. When the pump laser wavelength increases from 1546.29 nm to 1546.31 nm, the S- and AS-resonances experience significant decreases and are close to the reference resonances. This indicates the occurrence of the nPBI.

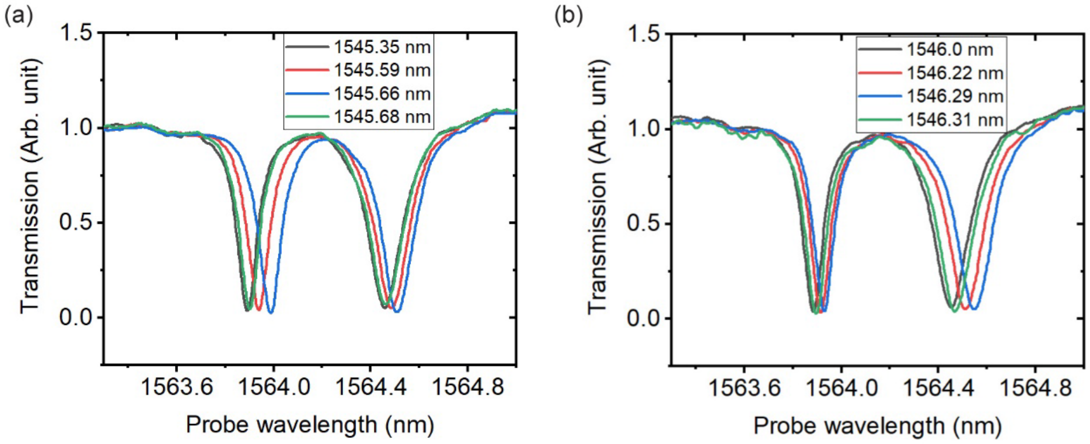

Figure 5.20 Shifts of split resonances when the device is pumped. (a) Measured transmission spectra when the pump laser wavelength increases and pumps the left notch in the pump region. The inset shows the wavelengths of the pump laser. (b) Measured transmission spectra when the pump laser wavelength increases and pumps the right notch in the pump region. The inset shows the wavelengths of the pump laser.

Figure 5.21 summarises the shifts of the S- and AS-resonances in the probe scan region. The pump laser wavelength increases in the pump scan region from 1545.35 nm to 1546.45 nm. The measurement is carried out with the pump power of 7.5 dBm and 5.5 dBm, respectively.

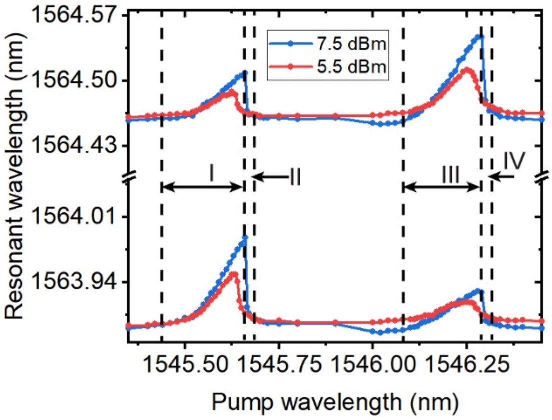

Figure 5.21 Shifts of the S- and AS-resonances in the probe scan region when the pump laser wavelength increases in the pump scan region. The resonant wavelengths are measured using the probe laser.

It is observed that each resonance experiences four main changes. Region I, II, III and IV are shown to present the four changes when the pump power is 7.5 dBm. Region I and II show the shifts of the S- and AS-resonances when the S-mode in the pump scan region is pumped. The significant change of the resonances in region II is due to pPBI. Regions III and IV present the shifts of the S- and AS-resonances when the pump the AS-mode in the pump scan region is pumped. The significant change of the resonances in region IV is due to nPBI.

5.5.2 Variation of mode splitting width when the device is pumped

The shifts of split resonances shown in Figure 5.21 result from the optomechanical actuation and the thermo-optical effect. It is necessary to decouple the thermo-optical effect in order to obtain the wavelength tuning due to optomechanical actuation. As discussed above, the thermo-optical effect leads to the same shifts of the S- and AS-resonances. Therefore, the variation of the splitting width between the S- and AS-resonances presents the contribution from optomechanical actuation. Figure 5.22 shows the measured variations of the splitting width between the S- and AS-resonances in the probe scan region. The pump laser wavelength increases in the pump scan region from 1545.35 nm to 1546.45 nm.

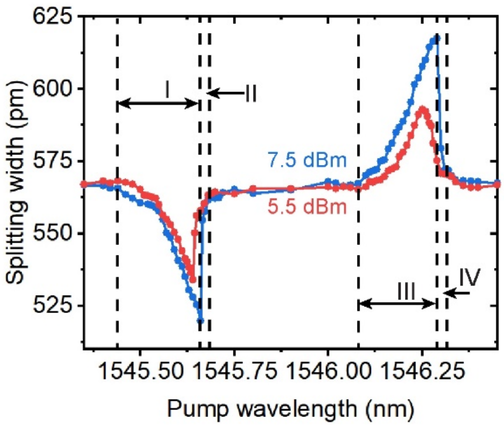

Figure 5.22 Measured splitting width between the S- and AS-resonances in the probe scan region. The pump wavelength is increased in the pump scan region.

The splitting width experience four main changes when the pump laser wavelength increases. Regions I, II, III and IV are plotted to present the four changes when the pump power is 7.5 dBm. The regions are the same as the regions in Figure 5.21. It clearly shows that the splitting width experiences a significant increase in Region II where the pPBI occurs, and a significant decrease in Region IV where the nPBI occurs. It can also be observed that the difference between the blue (7.5 dBm) and red (5.5 dBm) lines change nonlinearly with the pump wavelength. The significant differences appear in regions II and IV where the PBIs occur.

Figure 5.23 shows the simulation and experimental results of the mode splitting width between the S- and AS-resonances. The pump power is 7.5 dBm in Figure 5.23(a) and is 5.5 dBm in Figure 5.23(b). In the simulation, the absorption limited quality factors, Q_{abs}=1.4×10^6 for the S-mode and 1.2×10^6

for the AS-mode, are used to fit the experimental results. Figure 5.23(a)(b) shows that the simulation results agree well with the experimental results, which verifies the theoretical analysis of PBIs.

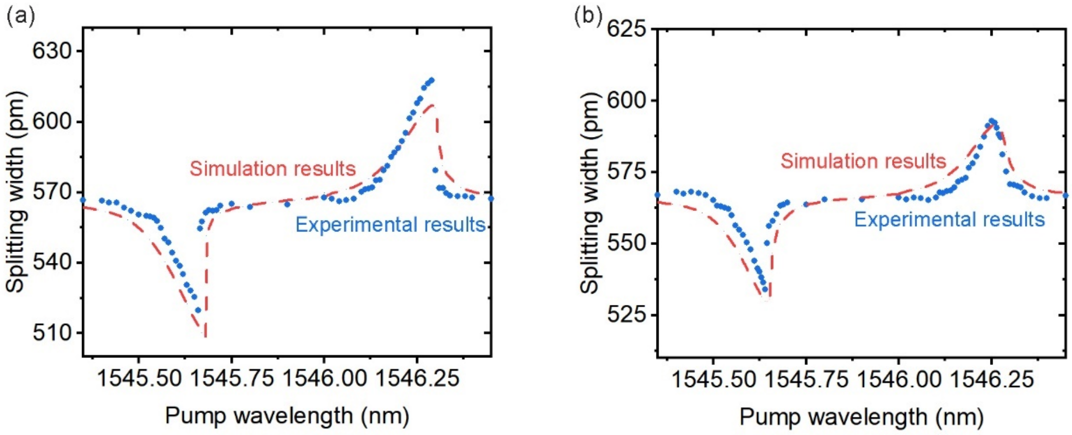

Figure 5.23 Comparison between the simulation and experimental results of the splitting width. The splitting width is between the S- and AS-resonances in the probe scan region. (a) The pump power is 7.5 dBm, and the pump wavelength is increased in the pump scan region. (b) Comparison between the simulation and experimental results of the splitting width when the pump power is 5.5 dBm.

5.6 Potential applications of the devices

The pPBI and nPBI have been theoretically and experimentally studied in an optomechanical device based on two coupled microrings. The pPBI originates from the attractive optical gradient force generated by pumping the S-optical mode. The occurrence of pPBI induces a significant increase in the splitting width between the S- and AS-resonances. On the contrary, the nPBI originates from the repulsive optical gradient force generated by pumping the AS-optical mode. The nPBI induces a significant decrease in the splitting width.

The PBIs are physically similar to the optomechanical buckling transitions [230]. The stable positions of moveable nanostructures in the optomechanical systems are determined by the points where the optical forces balance the mechanical force. When the PBIs or the buckling transitions occur, the positions of the nanostructures experience significant changes. The PBIs will pull the nanostructures back towards their initial positions. On the contrary, the buckling transitions push the nanostructures away from their initial positions.

Figure 5.21 and Figure 5.22 show the changing of the splitting width between the S- and AS-resonances by adjusting the pump wavelength. The tuning of mode splitting width can be applied in the design described in Chapter 3. Two input light beams pump the S- and AS-resonances, respectively, for THz generation. An additional pump laser will be required for controlling the optical gradient forces. For a specific OAM state, the wavelength of the generated THz vortex beam can be tuned by changing the wavelength of the pump laser. Particularly, when PBI occurs, a great change in THz wavelength can be achieved by a small variation of the wavelength of the pump laser.

Figure 5.21 shows that the shifts of the S- and AS-resonances are due to the optomechanical-tuning and thermal effects. The wavelength tuning can be combined with the VV beam emitter proposed in Chapter 4. A pump is used to induce the optical gradient force and the thermal effect. Controlling the wavelength of the pump laser can adjust the resonant wavelength of the device. Two light beams, TE and TM waveguide modes, pump the tunable resonance can generate the FOPS beam with the desired wavelength.

The wavelength tuning based on the optomechanical-tuning effect and the thermal effect can also be explored for optical information processing. The optomechanical-tuning effect can be adjusted by changing the dimensions of the suspended waveguides or the gap between them. When the wavelength tuning due to the optomechanical actuation is balanced by the tuning due to the thermal effect, the S- and AS-resonances can be controlled individually. The selective control can benefit the reconfigurable optical filter and optical router.

Figure 5.22 shows the significant changes in the mode splitting width when PBIs occur. The changes can be utilized for ultra-sensitive sensing. For example, it can be used to measure the variations in the refractive index of the coupled microrings. The variations cause the resonance shift and induce the PBIs. The information of variations can be extracted from the significant change in the splitting width between S- and AS-resonances.

5.7 Conclusion

We have demonstrated an on-chip optomechanical device based on two coupled microring resonators. The coupled resonators possess positive and negative PBIs originating from the attractive and repulsive optical gradient forces, respectively. By measuring the splitting width between the self-referenced S- and AS-resonances, the wavelength tuning by optomechanical actuation is decoupled from the tuning by the thermo-optical effect. The splitting width experiences a significant increase when the pPBI occurs and experience a significant decrease when the nPBI occurs. The nonlinear changes of the splitting width are studied by combining the numerical calculation and experimental results.

The tuning of mode splitting width based on optical gradient forces could be applied in the design of the vortex beam emitters proposed in Chapters 3 and 4. The wavelength of the vortex beam can be adjusted, which would be useful for potential applications such as LiDAR systems based on the frequency-modulated continuous-wave approach. Besides, the optomechanical actuation and thermo-optical effect of the Si optomechanical device can be used to design all-optical photonic devices for optical information processing, such as optical filters. The device can also be utilized for ultrasensitive sensing, based on the significant change of the mode splitting width induced by the PBIs. The design can be further explored for achieving phonon lasing [231, 232], light delaying [233, 234], exceptional points in parity-time symmetric systems [235, 236] or extending the mode localization effects from MEMS coupled resonant sensors [237] to the optomechanical domain to achieve ultrasensitive optomechanical mode-localized sensors.

Chapter 6 Conclusion and outlook

6.1 Conclusion

A vortex beam possesses theoretically unbounded OAM and a spatially inhomogeneous state of polarization. The features have been exploited for optical sensing, communication, optical manipulation and imaging. The field is still developing and advancing many potential applications. For example, the performance of LiDAR systems may benefit from the two new degrees of freedom provided by the OAM states and SOPs of vortex beams. The generation of the desired vortex beam is the crucial first step. In this thesis, integrated vortex beam emitters based on microring resonators have been studied.

A nonlinear vortex beam emitter that functions in the THz regime is proposed and evaluated based on simulation. The design utilises a $LiNbO_3$ microring, a Si microdisk, and an Au second-order top grating. Two infrared light beams pump the device from a coupling waveguide. The THz wave is generated via a DFG process in the $LiNbO_3$ and is confined by the Si microdisk. The confined THz wave can be vertically emitted into free space by the Au grating. The TC of the radiated THz vortex beam is determined by the azimuthal orders of the two pumps in the microring and the number of grating elements.

This device has been demonstrated to generate an adjustable THz vortex beam by changing the wavelengths of the incident light. The TC ranges from -2 to 4 in the simulated frequency range from 9 THz to 13.5 THz. A frequency shift accompanies the change in the TC, and the magnitude of the frequency change can be controlled by modifying the planar dimensions of the emitter. The proposed emitter has a planar dimension comparable to its functional wavelengths and can impart a tunable TC on a freely propagating THz light beam.

Next, an on-chip light emitter for generating VV beams is studied via numerical simulation. It allows the controllable generation of all points on a FOPS. The generator consists of a waveguide-coupled Si microring resonator decorated with angularly distributed cylindrical holes. By designing the waveguides with the square shape of the cross-section, the waveguide's fundamental TE and TM modes can have almost identical effective indices. The fundamental TE and TM input modes produce radial and azimuthal polarization, respectively, when their azimuthal order of WGMs match with the number of cylindrical holes.

The controlled generation of FOPS beams is demonstrated by utilizing the TE and TM input simultaneously. The generated radial and azimuthal polarization can form the basis to construct the SPs for the FOPS. The output polarization moves longitudinally on a great circle by tuning the phase difference between the two polarized beams that possess the same intensity. By tuning the intensity ratio between the two polarized beams, the polarization can scan horizontally along the equator of the FOPS. We derived the relationship between the target polarization and the two input parameters, the intensity ratio and the phase contrast. Based on the relationship, arbitrary points on the FOPS can be generated. The only assumption used in the derivation is that the TE and TM input modes generate pure radial and azimuthal polarization, respectively. So the relationship can be applied to any FOPS beam emitter that shares the basic configuration of our device.

The wavelength of a specific vortex beam generated by the proposed emitters is not tunable due to the fixed resonant wavelengths of the microring resonators. Applications, such as communications and LiDAR systems based on frequency-modulated continuous-wave approach, would require flexible frequency modulation. Next, a wavelength tuning approach based on an optomechanical device is demonstrated experimentally. The device consists of two coupled free-standing waveguides in two identical microrings, fabricated in the SOI process. The coupling between the two microrings results in mode splitting with the S- and AS-resonances showing in the transmission spectrum of the device. The attractive or repulsive optical force arises when the S- or AS-modes are pumped, respectively. The device demonstrates that both the S- and AS-resonant wavelengths are red-shifted by the optical gradient force and the thermo-optical effect.

Based on the optomechanical device, positive and negative PBIs are theoretically and experimentally studied for the first time. The PBIs originate from attractive and repulsive optical gradient forces, respectively. The wavelength tuning due to the optomechanical actuation can be decoupled from the tuning due to the thermo-optical effect by measuring the splitting width between the self-reference S- and AS-resonances. We demonstrated that the pPBI originates from the attractive optical gradient force. This instability significantly increases the splitting width between the S- and AS-resonances. On the contrary, the nPBI originates from the repulsive optical gradient force. This instability significantly decreases the splitting width.

6.2 Future work

For potential applications such as LiDAR applications and communications, the integrated vortex beam emitters need to be further studied. Some characteristics of the proposed emitters can be explored to improve the emitters' performance. For the THz vortex beam emitter, the conversion efficiency of the DFG process could be improved. For the VV beam emitter, the controlled polarization states can be extended to higher-order Poincaré spheres. For the generation of vortex beams with flexible wavelength-modulation, the combination between the proposed vortex beam emitters and the all-optical wavelength tuning should be considered. The following will describe the future work related to the desired improvement of the vortex beam emitters.

The proposed integrated vortex beam emitter can produce adjustable vortex beams in the THz frequency range. Two infrared pumps generate the THz via a DFG process. With both input lights set at a test value of 10 W, the output reaches the value of 2.0×10^{-5} W at l= 2. High-efficient radiation sources are desired for the applications of sensing and communication. The conversion efficiency can be improved by increasing the Q-factor of the microring. According to Section 3.1.2, the Q-factor is related to the length of the microring and the coupling coefficient between the bus waveguide and the microring. Therefore, the radius of the $LiNbO_3$ microring and the gap between the bus waveguide and microring can be optimized. Another method to increase the conversion efficiency is to reduce the momentum mismatch between the generated THz wave and the two infrared pumps. The quasi-phase-matching method can be explored.

The proposed integrated VV beam emitter can generate controlled polarization states on the FOPS. Generation of controlled polarization on an arbitrary HOP sphere is highly desired to expand the applications of sensing and communications. According to section 2.4, SPs for a l^{th}-order Poincaré sphere can be formed by the left and right circularly polarized vortex beams with TCs of $+l$ and $-l$, respectively. The two desired circularly polarized vortex beams can be generated based on the proposed VV beam emitter. For example, the TE and TM input modes, propagating along the x-direction in the bus waveguide, can generate an LHCP vortex beam with TC of $+l$ by optimizing the intensity ratio and phase contrast between the two input modes. When the same TE and TM input mode propagating along the -x-direction in the bus waveguide, an RHCP vortex beam with TC of $-l$ will be generated. So, by optimizing the intensity ratio and phase contrast between the LHCP and RHCP vortex beams, controlled polarization on a l^{th}-order Poincaré sphere can be generated.

Chapter 5 presents an integrated optomechanical device that can change the splitting width between the S- and AS-modes by adjusting the pumping wavelength. The device may be combined with the proposed THz vortex beam emitter to achieve a tunable wavelength at a specific TC. The material of the optomechanical device should be changed to be nonlinear for the THz generation via the DFG process. Three infrared pumps will be required. Two infrared pumps are used for the THz generation, and another infrared pump is used for inducing the optical gradient force and achieving the wavelength tuning. In order to achieve a large wavelength tuning, the optimization of the geometry of the two coupled microrings and the gap between them should be conducted.

The optomechanical device can also be combined with the proposed VV beam emitter to achieve FOPS beams with tunable wavelength. Angularly distributed holes should be etched on the top of the waveguides of the optomechanical device for outcoupling light. The optomechanical actuation and thermo-optical effect of the Si device can be utilised to tune the resonant wavelength. So, apart from the two infrared pumps for the generation of FOPS beams, another infrared pump for inducing optical gradient force and thermo-optical effect is required.

Bibliography

1. A. M. Yao and M. J. Padgett, "Orbital angular momentum: origins, behavior and applications," Advances in Optics and Photonics **3**(2), 161-204 (2011).
2. L. Allen, M. W. Beijersbergen, R. Spreeuw, and J. Woerdman, "Orbital angular momentum of light and the transformation of Laguerre-Gaussian laser modes," Physical Review A **45**(11), 8185-8189 (1992).
3. H. Rubinsztein-Dunlop, A. Forbes, M. V. Berry, M. R. Dennis, D. L. Andrews, M. Mansuripur, C. Denz, C. Alpmann, P. Banzer, and T. Bauer, "Roadmap on structured light," Journal of Optics **19**(1), 013001 (2016).
4. I. Kim, R. J. Martins, J. Jang, T. Badloe, S. Khadir, H.-Y. Jung, H. Kim, J. Kim, P. Genevet, and J. Rho, "Nanophotonics for light detection and ranging technology," Nature Nanotechnology **16**(5), 508-524 (2021).
5. M. Smit, J. Van der Tol, and M. Hill, "Moore's law in photonics," Laser & Photonics Reviews **6**(1), 1-13 (2012).
6. D. Thomson, A. Zilkie, J. E. Bowers, T. Komljenovic, G. T. Reed, L. Vivien, D. Marris-Morini, E. Cassan, L. Virot, and J.-M. Fédéli, "Roadmap on silicon photonics," Journal of Optics **18**(7), 073003 (2016).
7. S. Royo and M. Ballesta-Garcia, "An Overview of Lidar Imaging Systems for Autonomous Vehicles," Applied Sciences **9**(19), 4093 (2019).
8. D. L. Andrews and M. Babiker, *The Angular Momentum Of Light* (Cambridge University Press, Cambridge, UK, 2012).
9. S. M. Barnett, M. Babiker, and M. J. Padgett, "Optical orbital angular momentum," Philosophical Transactions of the Royal Society A: Mathematical, Physical and Engineering Sciences **375**(2087), 20150444 (2017).
10. Q. Zhan, "Cylindrical vector beams: from mathematical concepts to applications," Advances in Optics and Photonics **1**(1), 1-57 (2009).
11. Y. Shen, X. Wang, Z. Xie, C. Min, X. Fu, Q. Liu, M. Gong, and X. Yuan, "Optical vortices 30 years on: OAM manipulation from topological charge to multiple singularities," Light: Science & Applications **8**(1), 90 (2019).
12. K. Y. Bliokh, A. Y. Bekshaev, and F. Nori, "Optical momentum, spin, and angular momentum in dispersive media," Physical Review Letters **119**(7), 073901 (2017).
13. K. Y. Bliokh and F. Nori, "Transverse and longitudinal angular momenta of light," Physics Reports **592**, 1-38 (2015).
14. R. Fickler, G. Campbell, B. Buchler, P. K. Lam, and A. Zeilinger, "Quantum entanglement of angular momentum states with quantum numbers up to 10,010," Proceedings of the National Academy of Sciences **113**(48), 13642-13647 (2016).
15. M. P. Lavery, F. C. Speirits, S. M. Barnett, and M. J. Padgett, "Detection of a spinning object using light’s orbital angular momentum," Science **341**(6145), 537-540 (2013).
16. W. Zhang, J. Gao, D. Zhang, Y. He, T. Xu, R. Fickler, and L. Chen, "Free-space remote sensing of rotation at the photon-counting level," Physical Review Applied **10**(4), 044014 (2018).
17. J. Liu, W. Liu, S. Li, D. Wei, H. Gao, and F. Li, "Enhancement of the angular rotation measurement sensitivity based on SU (2) and SU (1, 1) interferometers," Photonics Research **5**(6), 617-622 (2017).
18. S. Xiao, L. Zhang, D. Wei, F. Liu, Y. Zhang, and M. Xiao, "Orbital angular momentum-enhanced measurement of rotation vibration using a Sagnac interferometer," Optics Express **26**(2), 1997-2005 (2018).
19. Z. Zhang, T. Qiao, K. Ma, J. Zhang, L. Cen, F. Wang, and Y. Zhao, "Super-resolving angular rotation measurement using binary-outcome homodyne detection," Optics Express **24**(16), 18477-18484 (2016).

20. J. Guo, S. Ming, Y. Wu, L. Chen, and W. Zhang, "Super-sensitive rotation measurement with an orbital angular momentum atom-light hybrid interferometer," Optics Express **29**(1), 208-218 (2021).
21. A. H. Dorrah, M. Zamboni-Rached, and M. Mojahedi, "Experimental demonstration of tunable refractometer based on orbital angular momentum of longitudinally structured light," Light: Science & Applications **7**(1), 40 (2018).
22. F. Xia, Y. Zhao, H.-f. Hu, and Y. Zhang, "Optical fiber sensing technology based on Mach-Zehnder interferometer and orbital angular momentum beam," Applied Physics Letters **112**(22), 221105 (2018).
23. R. Lv, L. Qiu, H. Hu, L. Meng, and Y. Zhang, "The phase interrogation method for optical fiber sensor by analyzing the fork interference pattern," Applied Physics B **124**(2), 32 (2018).
24. A. Datta, A. Saha, and A. Shukla, "Investigation of modal-interference-induced fiber optic refractive index sensor: markedly enhanced sensitivity realized by shining an optical vortex beam," Journal of the Optical Society of America A **34**(11), 2034-2045 (2017).
25. N. Cvijetic, G. Milione, E. Ip, and T. Wang, "Detecting lateral motion using light's orbital angular momentum," Scientific Reports **5**(1), 15422 (2015).
26. K. Liu, Y. Cheng, X. Li, and Y. Gao, "Microwave-Sensing Technology Using Orbital Angular Momentum: Overview of Its Advantages," IEEE Vehicular Technology Magazine **14**(2), 112-118 (2019).
27. G. Xie, H. Song, Z. Zhao, G. Milione, Y. Ren, C. Liu, R. Zhang, C. Bao, L. Li, and Z. Wang, "Using a complex optical orbital-angular-momentum spectrum to measure object parameters," Optics Letters **42**(21), 4482-4485 (2017).
28. J. Wang, J.-Y. Yang, I. M. Fazal, N. Ahmed, Y. Yan, H. Huang, Y. Ren, Y. Yue, S. Dolinar, and M. Tur, "Terabit free-space data transmission employing orbital angular momentum multiplexing," Nature Photonics **6**(7), 488-496 (2012).
29. M. Krenn, J. Handsteiner, M. Fink, R. Fickler, R. Ursin, M. Malik, and A. Zeilinger, "Twisted light transmission over 143 km," Proceedings of the National Academy of Sciences **113**(48), 13648-13653 (2016).
30. M. P. Lavery, C. Peuntinger, K. Günthner, P. Banzer, D. Elser, R. W. Boyd, M. J. Padgett, C. Marquardt, and G. Leuchs, "Free-space propagation of high-dimensional structured optical fields in an urban environment," Science Advances **3**(10), e1700552 (2017).
31. L. Gong, Q. Zhao, H. Zhang, X.-Y. Hu, K. Huang, J.-M. Yang, and Y.-M. Li, "Optical orbital-angular-momentum-multiplexed data transmission under high scattering," Light: Science & Applications **8**(1), 27 (2019).
32. N. Bozinovic, Y. Yue, Y. Ren, M. Tur, P. Kristensen, H. Huang, A. E. Willner, and S. Ramachandran, "Terabit-scale orbital angular momentum mode division multiplexing in fibers," Science **340**(6140), 1545-1548 (2013).
33. Z. Xie, S. Gao, T. Lei, S. Feng, Y. Zhang, F. Li, J. Zhang, Z. Li, and X. Yuan, "Integrated (de) multiplexer for orbital angular momentum fiber communication," Photonics Research **6**(7), 743-749 (2018).
34. J. Liu, S. Li, Y. Ding, S. Chen, C. Du, Q. Mo, T. Morioka, K. Yvind, L. K. Oxenløwe, and S. Yu, "Orbital angular momentum modes emission from a silicon photonic integrated device for km-scale data-carrying fiber transmission," Optics Express **26**(12), 15471-15479 (2018).
35. M. Erhard, R. Fickler, M. Krenn, and A. Zeilinger, "Twisted photons: new quantum perspectives in high dimensions," Light: Science & Applications **7**(3), 17146 (2018).
36. M. Mafu, A. Dudley, S. Goyal, D. Giovannini, M. McLaren, M. J. Padgett, T. Konrad, F. Petruccione, N. Lütkenhaus, and A. Forbes, "Higher-dimensional orbital-angular-momentum-based quantum key distribution with mutually unbiased bases," Physical Review A **88**(3), 032305 (2013).
37. A. Sit, F. Bouchard, R. Fickler, J. Gagnon-Bischoff, H. Larocque, K. Heshami, D. Elser, C. Peuntinger, K. Günthner, and B. Heim, "High-dimensional intracity quantum cryptography with structured photons," Optica **4**(9), 1006-1010 (2017).

38. S.-K. Liao, H.-L. Yong, C. Liu, G.-L. Shentu, D.-D. Li, J. Lin, H. Dai, S.-Q. Zhao, B. Li, and J.-Y. Guan, "Long-distance free-space quantum key distribution in daylight towards inter-satellite communication," Nature Photonics **11**(8), 509-513 (2017).
39. X.-L. Wang, X.-D. Cai, Z.-E. Su, M.-C. Chen, D. Wu, L. Li, N.-L. Liu, C.-Y. Lu, and J.-W. Pan, "Quantum teleportation of multiple degrees of freedom of a single photon," Nature **518**(7540), 516-519 (2015).
40. E. Nagali, L. Sansoni, F. Sciarrino, F. De Martini, L. Marrucci, B. Piccirillo, E. Karimi, and E. Santamato, "Optimal quantum cloning of orbital angular momentum photon qubits through Hong–Ou–Mandel coalescence," Nature Photonics **3**(12), 720-723 (2009).
41. A. Nicolas, L. Veissier, L. Giner, E. Giacobino, D. Maxein, and J. Laurat, "A quantum memory for orbital angular momentum photonic qubits," Nature photonics **8**(3), 234-238 (2014).
42. T. Stav, A. Faerman, E. Maguid, D. Oren, V. Kleiner, E. Hasman, and M. Segev, "Quantum entanglement of the spin and orbital angular momentum of photons using metamaterials," Science **361**(6407), 1101-1104 (2018).
43. Y. Yang, Y. Ren, M. Chen, Y. Arita, and C. Rosales-Guzmán, "Optical trapping with structured light: a review," Advanced Photonics **3**(3), 034001 (2021).
44. M. Padgett and R. Bowman, "Tweezers with a twist," Nature photonics **5**(6), 343-348 (2011).
45. H. He, M. Friese, N. Heckenberg, and H. Rubinsztein-Dunlop, "Direct observation of transfer of angular momentum to absorptive particles from a laser beam with a phase singularity," Physical Review Letters **75**(5), 826-829 (1995).
46. N. Simpson, K. Dholakia, L. Allen, and M. Padgett, "Mechanical equivalence of spin and orbital angular momentum of light: an optical spanner," Optics Letters **22**(1), 52-54 (1997).
47. M. Dienerowitz, M. Mazilu, P. J. Reece, T. F. Krauss, and K. Dholakia, "Optical vortex trap for resonant confinement of metal nanoparticles," Optics Express **16**(7), 4991-4999 (2008).
48. K. Gahagan and G. J. Swartzlander, "Optical vortex trapping of particles," Optics Letters **21**(11), 827-829 (1996).
49. A. O'neil, I. MacVicar, L. Allen, and M. Padgett, "Intrinsic and extrinsic nature of the orbital angular momentum of a light beam," Physical Review Letters **88**(5), 053601 (2002).
50. V. Garcés-Chávez, D. McGloin, M. Padgett, W. Dultz, H. Schmitzer, and K. Dholakia, "Observation of the transfer of the local angular momentum density of a multiringed light beam to an optically trapped particle," Physical Review Letters **91**(9), 093602 (2003).
51. K. Ladavac and D. G. Grier, "Microoptomechanical pumps assembled and driven by holographic optical vortex arrays," Optics Express **12**(6), 1144-1149 (2004).
52. G. A. Swartzlander, E. L. Ford, R. S. Abdul-Malik, L. M. Close, M. A. Peters, D. M. Palacios, and D. W. Wilson, "Astronomical demonstration of an optical vortex coronagraph," Optics Express **16**(14), 10200-10207 (2008).
53. S. Fürhapter, A. Jesacher, S. Bernet, and M. Ritsch-Marte, "Spiral interferometry," Optics Letters **30**(15), 1953-1955 (2005).
54. K. I. Willig, S. O. Rizzoli, V. Westphal, R. Jahn, and S. W. Hell, "STED microscopy reveals that synaptotagmin remains clustered after synaptic vesicle exocytosis," Nature **440**(7086), 935-939 (2006).
55. P. Tan, X.-C. Yuan, G. Yuan, and Q. Wang, "High-resolution wide-field standing-wave surface plasmon resonance fluorescence microscopy with optical vortices," Applied Physics Letters **97**(24), 241109 (2010).
56. C. Zhang, C. Min, L. Du, and X.-C. Yuan, "Perfect optical vortex enhanced surface plasmon excitation for plasmonic structured illumination microscopy imaging," Applied Physics Letters **108**(20), 201601 (2016).
57. X. W. Wang, Z. Q. Nie, Y. Liang, J. Wang, T. Li, and B. H. Jia, "Recent advances on optical vortex generation," Nanophotonics **7**(9), 1533-1556 (2018).
58. M. Beijersbergen, R. Coerwinkel, M. Kristensen, and J. Woerdman, "Helical-wavefront laser beams produced with a spiral phaseplate," Optics Communications **112**(5), 321-327 (1994).
59. G. Campbell, B. Hage, B. Buchler, and P. K. Lam, "Generation of high-order optical vortices using directly machined spiral phase mirrors," Applied Optics **51**(7), 873-876 (2012).

60. E. Brasselet, M. Malinauskas, A. Žukauskas, and S. Juodkazis, "Photopolymerized microscopic vortex beam generators: Precise delivery of optical orbital angular momentum," Applied Physics Letters **97**(21), 211108 (2010).

61. K. Weber, F. Hütt, S. Thiele, T. Gissibl, A. Herkommer, and H. Giessen, "Single mode fiber based delivery of OAM light by 3D direct laser writing," Optics Express **25**(17), 19672-19679 (2017).

62. H. T. Chen, A. J. Taylor, and N. F. Yu, "A review of metasurfaces: physics and applications," Reports on Progress in Physics **79**(7), 076401 (2016).

63. S. B. Glybovski, S. A. Tretyakov, P. A. Belov, Y. S. Kivshar, and C. R. Simovski, "Metasurfaces: From microwaves to visible," Physics Reports **634**, 1-72 (2016).

64. J. Sun, X. Wang, T. Xu, Z. A. Kudyshev, A. N. Cartwright, and N. M. Litchinitser, "Spinning light on the nanoscale," Nano Letters **14**(5), 2726-2729 (2014).

65. C.-F. Chen, C.-T. Ku, Y.-H. Tai, P.-K. Wei, H.-N. Lin, and C.-B. Huang, "Creating optical near-field orbital angular momentum in a gold metasurface," Nano Letters **15**(4), 2746-2750 (2015).

66. M. Decker and I. Staude, "Resonant dielectric nanostructures: a low-loss platform for functional nanophotonics," Journal of Optics **18**(10), 103001 (2016).

67. P. Genevet, F. Capasso, F. Aieta, M. Khorasaninejad, and R. Devlin, "Recent advances in planar optics: from plasmonic to dielectric metasurfaces," Optica **4**(1), 139-152 (2017).

68. K. E. Chong, I. Staude, A. James, J. Dominguez, S. Liu, S. Campione, G. S. Subramania, T. S. Luk, M. Decker, and D. N. Neshev, "Polarization-independent silicon metadevices for efficient optical wavefront control," Nano Letters **15**(8), 5369-5374 (2015).

69. R. Dharmavarapu, K.-i. Izumi, I. Katayama, S. H. Ng, J. Vongsvivut, M. J. Tobin, A. Kuchmizhak, Y. Nishijima, S. Bhattacharya, and S. Juodkazis, "Dielectric cross-shaped-resonator-based metasurface for vortex beam generation at mid-IR and THz wavelengths," Nanophotonics **8**(7), 1263-1270 (2019).

70. H. Zhang, X. Zhang, Q. Xu, Q. Wang, Y. Xu, M. Wei, Y. Li, J. Gu, Z. Tian, and C. Ouyang, "Polarization-independent all-silicon dielectric metasurfaces in the terahertz regime," Photonics Research **6**(1), 24-29 (2018).

71. K. Huang, H. Liu, S. Restuccia, M. Q. Mehmood, S.-T. Mei, D. Giovannini, A. Danner, M. J. Padgett, J.-H. Teng, and C.-W. Qiu, "Spiniform phase-encoded metagratings entangling arbitrary rational-order orbital angular momentum," Light: Science & Applications **7**(3), 17156 (2018).

72. J. Wang, Z. Shao, Y. Wen, X. Qiu, Y. Chen, Y. Zhang, S. Yu, and L. Chen, "All-dielectric metasurface grating for on-chip multi-channel orbital angular momentum generation and detection," Optics Express **27**(13), 18794-18802 (2019).

73. A. Zhan, S. Colburn, R. Trivedi, T. K. Fryett, C. M. Dodson, and A. Majumdar, "Low-contrast dielectric metasurface optics," ACS Photonics **3**(2), 209-214 (2016).

74. M. L. Chen, L. J. Jiang, and W. E. Sha, "Orbital angular momentum generation and detection by geometric-phase based metasurfaces," Applied Sciences **8**(3), 362 (2018).

75. S. Pancharatnam, "Generalized theory of interference and its applications," Proceedings of the Indian Academy of Sciences - Section A **44**(5), 247-262 (1956).

76. G. Biener, A. Niv, V. Kleiner, and E. Hasman, "Formation of helical beams by use of Pancharatnam–Berry phase optical elements," Optics Letters **27**(21), 1875-1877 (2002).

77. L. Marrucci, C. Manzo, and D. Paparo, "Optical spin-to-orbital angular momentum conversion in inhomogeneous anisotropic media," Physical Review Letters **96**(16), 163905 (2006).

78. N. Yu, P. Genevet, M. A. Kats, F. Aieta, J.-P. Tetienne, F. Capasso, and Z. Gaburro, "Light propagation with phase discontinuities: generalized laws of reflection and refraction," Science **334**(6054), 333-337 (2011).

79. E. Karimi, S. A. Schulz, I. De Leon, H. Qassim, J. Upham, and R. W. Boyd, "Generating optical orbital angular momentum at visible wavelengths using a plasmonic metasurface," Light: Science & Applications **3**(5), e167 (2014).

80. D. Hakobyan, H. Magallanes, G. Seniutinas, S. Juodkazis, and E. Brasselet, "Tailoring orbital angular momentum of light in the visible domain with metallic metasurfaces," Advanced Optical Materials **4**(2), 306-312 (2016).
81. S. Chen, Y. Cai, G. Li, S. Zhang, and K. W. Cheah, "Geometric metasurface fork gratings for vortex‐beam generation and manipulation," Laser & Photonics Reviews **10**(2), 322-326 (2016).
82. R. C. Devlin, A. Ambrosio, D. Wintz, S. L. Oscurato, A. Y. Zhu, M. Khorasaninejad, J. Oh, P. Maddalena, and F. Capasso, "Spin-to-orbital angular momentum conversion in dielectric metasurfaces," Optics Express **25**(1), 377-393 (2017).
83. A. Niv, Y. Gorodetski, V. Kleiner, and E. Hasman, "Topological spin-orbit interaction of light in anisotropic inhomogeneous subwavelength structures," Optics Letters **33**(24), 2910-2912 (2008).
84. R. C. Devlin, A. Ambrosio, N. A. Rubin, J. B. Mueller, and F. Capasso, "Arbitrary spin-to–orbital angular momentum conversion of light," Science **358**(6365), 896-901 (2017).
85. M. Harris, C. Hill, and J. Vaughan, "Optical helices and spiral interference fringes," Optics Communications **106**(4), 161-166 (1994).
86. E. Abramochkin, N. Losevsky, and V. Volostnikov, "Generation of spiral-type laser beams," Optics Communications **141**(1), 59-64 (1997).
87. R. Oron, N. Davidson, A. A. Friesem, and E. Hasman, "Efficient formation of pure helical laser beams," Optics Communications **182**(1), 205-208 (2000).
88. P.-A. Belanger, R. L. Lachance, and C. Pare, "Super-Gaussian output from a CO_2 laser by using a graded-phase mirror resonator," Optics Letters **17**(10), 739-741 (1992).
89. I. A. Litvin, L. Burger, and A. Forbes, "Petal-like modes in Porro prism resonators," Optics Express **15**(21), 14065-14077 (2007).
90. J. Bourderionnet, A. Brignon, J.-P. Huignard, A. Delboulbe, and B. Loiseaux, "Spatial mode control of a diode-pumped Nd: YAG laser by an intracavity liquid-crystal light valve," Optics Letters **26**(24), 1958-1960 (2001).
91. S. Ngcobo, I. Litvin, L. Burger, and A. Forbes, "A digital laser for on-demand laser modes," Nature Communications **4**(1), 2289 (2013).
92. E. Maguid, R. Chriki, M. Yannai, V. Kleiner, E. Hasman, A. A. Friesem, and N. Davidson, "Topologically controlled intracavity laser modes based on pancharatnam-berry phase," ACS Photonics **5**(5), 1817-1821 (2018).
93. H. Sroor, Y.-W. Huang, B. Sephton, D. Naidoo, A. Valles, V. Ginis, C.-W. Qiu, A. Ambrosio, F. Capasso, and A. Forbes, "High-purity orbital angular momentum states from a visible metasurface laser," Nature Photonics **14**(8), 498-503 (2020).
94. X. Cai, J. Wang, M. J. Strain, B. Johnson-Morris, J. Zhu, M. Sorel, J. L. O'Brien, M. G. Thompson, and S. Yu, "Integrated Compact Optical Vortex Beam Emitters," Science **338**(6105), 363-366 (2012).
95. S. Li, Y. Ding, X. Guan, H. Tan, Z. Nong, L. Wang, L. Liu, L. Zhou, C. Yang, and K. Yvind, "Compact high-efficiency vortex beam emitter based on a silicon photonics micro-ring," Optics Letters **43**(6), 1319-1322 (2018).
96. Z. Xie, T. Lei, F. Li, H. Qiu, Z. Zhang, H. Wang, C. Min, L. Du, Z. Li, and X. Yuan, "Ultra-broadband on-chip twisted light emitter for optical communications," Light: Science & Applications **7**(4), 18001 (2018).
97. H. Li, D. B. Phillips, X. Wang, Y.-L. D. Ho, L. Chen, X. Zhou, J. Zhu, S. Yu, and X. Cai, "Orbital angular momentum vertical-cavity surface-emitting lasers," Optica **2**(6), 547-552 (2015).
98. P. Miao, Z. Zhang, J. Sun, W. Walasik, S. Longhi, N. M. Litchinitser, and L. Feng, "Orbital angular momentum microlaser," Science **353**(6298), 464-467 (2016).
99. J. Zhang, C. Sun, B. Xiong, J. Wang, Z. Hao, L. Wang, Y. Han, H. Li, Y. Luo, and Y. Xiao, "An InP-based vortex beam emitter with monolithically integrated laser," Nature Communications **9**(1), 2652 (2018).
100. G. Thalhammer, R. W. Bowman, G. D. Love, M. J. Padgett, and M. Ritsch-Marte, "Speeding up liquid crystal SLMs using overdrive with phase change reduction," Optics Express **21**(2), 1779-1797 (2013).

101. M. J. Strain, X. Cai, J. Wang, J. Zhu, D. B. Phillips, L. Chen, M. Lopez-Garcia, J. L. O’Brien, M. G. Thompson, and M. Sorel, "Fast electrical switching of orbital angular momentum modes using ultra-compact integrated vortex emitters," Nature Communications **5**(1), 4856 (2014).
102. C. Huang, C. Zhang, S. Xiao, Y. Wang, Y. Fan, Y. Liu, N. Zhang, G. Qu, H. Ji, and J. Han, "Ultrafast control of vortex microlasers," Science **367**(6481), 1018-1021 (2020).
103. Z. Zhang, X. Qiao, B. Midya, K. Liu, J. Sun, T. Wu, W. Liu, R. Agarwal, J. M. Jornet, and S. Longhi, "Tunable topological charge vortex microlaser," Science **368**(6492), 760-763 (2020).
104. N. C. Zambon, P. St-Jean, M. Milićević, A. Lemaître, A. Harouri, L. Le Gratiet, O. Bleu, D. Solnyshkov, G. Malpuech, and I. Sagnes, "Optically controlling the emission chirality of microlasers," Nature Photonics **13**(4), 283-288 (2019).
105. J. Chen, C. Wan, and Q. Zhan, "Vectorial optical fields: recent advances and future prospects," Science Bulletin **63**(1), 54-74 (2018).
106. R. Dorn, S. Quabis, and G. Leuchs, "Sharper focus for a radially polarized light beam," Physical Review Letters **91**(23), 233901 (2003).
107. L. Novotny, M. Beversluis, K. Youngworth, and T. Brown, "Longitudinal field modes probed by single molecules," Physical Review Letters **86**(23), 5251-5254 (2001).
108. M. Neugebauer, P. Woźniak, A. Bag, G. Leuchs, and P. Banzer, "Polarization-controlled directional scattering for nanoscopic position sensing," Nature Communications **7**(1), 11286 (2016).
109. L. Fang, Z. Wan, A. Forbes, and J. Wang, "Vectorial Doppler metrology," Nature Communications **12**(1), 4186 (2021).
110. S. Segawa, Y. Kozawa, and S. Sato, "Resolution enhancement of confocal microscopy by subtraction method with vector beams," Optics Letters **39**(11), 3118-3121 (2014).
111. P. Török and P. Munro, "The use of Gauss-Laguerre vector beams in STED microscopy," Optics Express **12**(15), 3605-3617 (2004).
112. M. Michihata, T. Hayashi, and Y. Takaya, "Measurement of axial and transverse trapping stiffness of optical tweezers in air using a radially polarized beam," Applied Optics **48**(32), 6143-6151 (2009).
113. Y. Kozawa and S. Sato, "Optical trapping of micrometer-sized dielectric particles by cylindrical vector beams," Optics Express **18**(10), 10828-10833 (2010).
114. V. Niziev and A. Nesterov, "Influence of beam polarization on laser cutting efficiency," Journal of Physics D: Applied Physics **32**(13), 1455-1461 (1999).
115. M. Meier, V. Romano, and T. Feurer, "Material processing with pulsed radially and azimuthally polarized laser radiation," Applied Physics A **86**(3), 329-334 (2007).
116. G. Milione, M. P. Lavery, H. Huang, Y. Ren, G. Xie, T. A. Nguyen, E. Karimi, L. Marrucci, D. A. Nolan, and R. R. Alfano, "4× 20 Gbit/s mode division multiplexing over free space using vector modes and a q-plate mode (de) multiplexer," Optics Letters **40**(9), 1980-1983 (2015).
117. V. D'ambrosio, E. Nagali, S. P. Walborn, L. Aolita, S. Slussarenko, L. Marrucci, and F. Sciarrino, "Complete experimental toolbox for alignment-free quantum communication," Nature communications **3**(1), 961 (2012).
118. D. Chen, S.-H. Zhao, L. Shi, and Y. Liu, "Measurement-device-independent quantum key distribution with pairs of vector vortex beams," Physical Review A **93**(3), 032320 (2016).
119. C. Rosales-Guzmán, B. Ndagano, and A. Forbes, "A review of complex vector light fields and their applications," Journal of Optics **20**(12), 123001 (2018).
120. G. Milione, H. Sztul, D. Nolan, and R. Alfano, "Higher-order Poincaré sphere, Stokes parameters, and the angular momentum of light," Physical Review Letters **107**(5), 053601 (2011).
121. X. Yi, Y. Liu, X. Ling, X. Zhou, Y. Ke, H. Luo, S. Wen, and D. Fan, "Hybrid-order Poincaré sphere," Physical Review A **91**(2), 023801 (2015).
122. D. Pohl, "Operation of a ruby laser in the purely transverse electric mode TE01," Applied Physics Letters **20**(7), 266-267 (1972).
123. Y. Kozawa and S. Sato, "Generation of a radially polarized laser beam by use of a conical Brewster prism," Optics Letters **30**(22), 3063-3065 (2005).

124. M. A. Ahmed, A. Voss, M. M. Vogel, and T. Graf, "Multilayer polarizing grating mirror used for the generation of radial polarization in Yb: YAG thin-disk lasers," Optics Letters **32**(22), 3272-3274 (2007).

125. M. A. Ahmed, M. Haefner, M. Vogel, C. Pruss, A. Voss, W. Osten, and T. Graf, "High-power radially polarized Yb: YAG thin-disk laser with high efficiency," Optics Express **19**(6), 5093-5103 (2011).

126. T. Kämpfe, S. Tonchev, A. V. Tishchenko, D. Gergov, and O. Parriaux, "Azimuthally polarized laser mode generation by multilayer mirror with wideband grating-induced TM leakage in the TE stopband," Optics Express **20**(5), 5392-5401 (2012).

127. I. Moshe, S. Jackel, and A. Meir, "Production of radially or azimuthally polarized beams in solid-state lasers and the elimination of thermally induced birefringence effects," Optics Letters **28**(10), 807-809 (2003).

128. A. Ito, Y. Kozawa, and S. Sato, "Selective oscillation of radially and azimuthally polarized laser beam induced by thermal birefringence and lensing," Journal of the Optical Society of America B **26**(4), 708-712 (2009).

129. K. Yonezawa, Y. Kozawa, and S. Sato, "Generation of a radially polarized laser beam by use of the birefringence of a c-cut Nd: YVO_4 crystal," Optics Letters **31**(14), 2151-2153 (2006).

130. D. Naidoo, F. S. Roux, A. Dudley, I. Litvin, B. Piccirillo, L. Marrucci, and A. Forbes, "Controlled generation of higher-order Poincaré sphere beams from a laser," Nature Photonics **10**(5), 327-332 (2016).

131. J.-l. Li, K.-i. Ueda, M. Musha, A. Shirakawa, and L.-x. Zhong, "Generation of radially polarized mode in Yb fiber laser by using a dual conical prism," Optics Letters **31**(20), 2969-2971 (2006).

132. M. Fridman, G. Machavariani, N. Davidson, and A. A. Friesem, "Fiber lasers generating radially and azimuthally polarized light," Applied Physics Letters **93**(19), 191104 (2008).

133. R. Zhou, B. Ibarra-Escamilla, J. W. Haus, P. E. Powers, and Q. Zhan, "Fiber laser generating switchable radially and azimuthally polarized beams with 140 mW output power at 1.6 µm wavelength," Applied Physics Letters **95**(19), 191111 (2009).

134. B. Sun, A. Wang, L. Xu, C. Gu, Z. Lin, H. Ming, and Q. Zhan, "Low-threshold single-wavelength all-fiber laser generating cylindrical vector beams using a few-mode fiber Bragg grating," Optics Letters **37**(4), 464-466 (2012).

135. B. Sun, A. Wang, L. Xu, C. Gu, Y. Zhou, Z. Lin, H. Ming, and Q. Zhan, "Transverse mode switchable fiber laser through wavelength tuning," Optics Letters **38**(5), 667-669 (2013).

136. F. Wang, F. Shi, T. Wang, F. Pang, T. Wang, and X. Zeng, "Method of generating femtosecond cylindrical vector beams using broadband mode converter," IEEE Photonics Technology Letters **29**(9), 747-750 (2017).

137. X. Zeng, Y. Li, L. Feng, S. Wu, C. Yang, W. Li, W. Tong, and J. Wu, "All-fiber orbital angular momentum mode multiplexer based on a mode-selective photonic lantern and a mode polarization controller," Optics Letters **43**(19), 4779-4782 (2018).

138. Y. Zhao, Y. Liu, L. Zhang, C. Zhang, J. Wen, and T. Wang, "Mode converter based on the long-period fiber gratings written in the two-mode fiber," Optics Express **24**(6), 6186-6195 (2016).

139. L. Feng, Y. Li, S. Wu, X. Guan, C. Yang, W. Tong, W. Li, J. Qiu, X. Hong, and Y. Zuo, "All-fiber generation of arbitrary cylindrical vector beams on the first-order Poincaré sphere," Photonics Research **8**(8), 1268-1277 (2020).

140. S. C. Tidwell, D. H. Ford, and W. D. Kimura, "Generating radially polarized beams interferometrically," Applied Optics **29**(15), 2234-2239 (1990).

141. M. A. Neil, F. Massoumian, R. Juškaitis, and T. Wilson, "Method for the generation of arbitrary complex vector wave fronts," Optics Letters **27**(21), 1929-1931 (2002).

142. C. Maurer, A. Jesacher, S. Fürhapter, S. Bernet, and M. Ritsch-Marte, "Tailoring of arbitrary optical vector beams," New Journal of Physics **9**(3), 78 (2007).

143. S. Chen, X. Zhou, Y. Liu, X. Ling, H. Luo, and S. Wen, "Generation of arbitrary cylindrical vector beams on the higher order Poincaré sphere," Optics Letters **39**(18), 5274-5276 (2014).

144. C. Rosales-Guzmán, N. Bhebhe, and A. Forbes, "Simultaneous generation of multiple vector beams on a single SLM," Optics Express **25**(21), 25697-25706 (2017).

145. R. Liu, L.-J. Kong, W.-R. Qi, S.-Y. Huang, Z.-X. Wang, C. Tu, Y. Li, and H.-T. Wang, "Compact, robust, and high-efficiency generator of vector optical fields," Optics Letters **44**(9), 2382-2385 (2019).

146. J. Mendoza-Hernández, M. F. Ferrer-Garcia, J. A. Rojas-Santana, and D. Lopez-Mago, "Cylindrical vector beam generator using a two-element interferometer," Optics Express **27**(22), 31810-31819 (2019).

147. Z. e. Bomzon, V. Kleiner, and E. Hasman, "Pancharatnam–Berry phase in space-variant polarization-state manipulations with subwavelength gratings," Optics Letters **26**(18), 1424-1426 (2001).

148. M. Stalder and M. Schadt, "Linearly polarized light with axial symmetry generated by liquid-crystal polarization converters," Optics Letters **21**(23), 1948-1950 (1996).

149. F. Cardano, E. Karimi, L. Marrucci, C. de Lisio, and E. Santamato, "Generation and dynamics of optical beams with polarization singularities," Optics Express **21**(7), 8815-8820 (2013).

150. A. D'Errico, R. D'Amelio, B. Piccirillo, F. Cardano, and L. Marrucci, "Measuring the complex orbital angular momentum spectrum and spatial mode decomposition of structured light beams," Optica **4**(11), 1350-1357 (2017).

151. F. Cardano, E. Karimi, S. Slussarenko, L. Marrucci, C. de Lisio, and E. Santamato, "Polarization pattern of vector vortex beams generated by q-plates with different topological charges," Applied Optics **51**(10), C1-C6 (2012).

152. M. Beresna, M. Gecevičius, P. G. Kazansky, and T. Gertus, "Radially polarized optical vortex converter created by femtosecond laser nanostructuring of glass," Applied Physics Letters **98**(20), 201101 (2011).

153. A. Arbabi, Y. Horie, M. Bagheri, and A. Faraon, "Dielectric metasurfaces for complete control of phase and polarization with subwavelength spatial resolution and high transmission," Nature Nanotechnology **10**(11), 937-943 (2015).

154. X. Yi, X. Ling, Z. Zhang, Y. Li, X. Zhou, Y. Liu, S. Chen, H. Luo, and S. Wen, "Generation of cylindrical vector vortex beams by two cascaded metasurfaces," Optics Express **22**(14), 17207-17215 (2014).

155. J. Lin, P. Genevet, M. A. Kats, N. Antoniou, and F. Capasso, "Nanostructured holograms for broadband manipulation of vector beams," Nano Letters **13**(9), 4269-4274 (2013).

156. Z. Zhao, J. Wang, S. Li, and A. E. Willner, "Metamaterials-based broadband generation of orbital angular momentum carrying vector beams," Optics Letters **38**(6), 932-934 (2013).

157. R. Li, X. Feng, D. Zhang, K. Cui, F. Liu, and Y. Huang, "Radially polarized orbital angular momentum beam emitter based on shallow-ridge silicon microring cavity," IEEE Photonics Journal **6**(3), 1-10 (2014).

158. Z. Shao, J. Zhu, Y. Chen, Y. Zhang, and S. Yu, "Spin-orbit interaction of light induced by transverse spin angular momentum engineering," Nature communications **9**(1), 926 (2018).

159. K. v. G. Cognée, H. M. Doeleman, P. Lalanne, and A. F. Koenderink, "Generation of Pure OAM Beams with a Single State of Polarization by Antenna-Decorated Microdisk Resonators," ACS Photonics **7**(11), 3049-3060 (2020).

160. Z. Shao, J. Zhu, Y. Zhang, Y. Chen, and S. Yu, "On-chip switchable radially and azimuthally polarized vortex beam generation," Optics Letters **43**(6), 1263-1266 (2018).

161. Y. Chen, K.-Y. Xia, W.-G. Shen, J. Gao, Z.-Q. Yan, Z.-Q. Jiao, J.-P. Dou, H. Tang, Y.-Q. Lu, and X.-M. Jin, "Vector vortex beam emitter embedded in a photonic chip," Physical Review Letters **124**(15), 153601 (2020).

162. D. Saeedkia, *Handbook Of Terahertz Technology For Imaging, Sensing And Communications* (Woodhead Publishing Limited, Cambridge, UK, 2013).

163. A. Y. Pawar, D. D. Sonawane, K. B. Erande, and D. V. Derle, "Terahertz technology and its applications," Drug Invention Today **5**(2), 157-163 (2013).

164. L. Yu, L. Hao, T. Meiqiong, H. Jiaoqi, L. Wei, D. Jinying, C. Xueping, F. Weiling, and Z. Yang, "The medical application of terahertz technology in non-invasive detection of cells and tissues: opportunities and challenges," RSC Advances **9**(17), 9354-9363 (2019).

165. I. F. Akyildiz, J. M. Jornet, and C. Han, "Terahertz band: Next frontier for wireless communications," Physical Communication **12**, 16-32 (2014).
166. Z. Hu, C. Wang, and R. Han, "A 32-unit 240-GHz heterodyne receiver array in 65-nm CMOS with array-wide phase locking," IEEE Journal of Solid-State Circuits **54**(5), 1216-1227 (2019).
167. E. A. Nanni, W. R. Huang, K.-H. Hong, K. Ravi, A. Fallahi, G. Moriena, R. D. Miller, and F. X. Kärtner, "Terahertz-driven linear electron acceleration," Nature Communications **6**, 8486 (2015).
168. A. Sirenko, P. Marsik, C. Bernhard, T. Stanislavchuk, V. Kiryukhin, and S.-W. Cheong, "Terahertz vortex beam as a spectroscopic probe of magnetic excitations," Physical Review Letters **122**(23), 237401 (2019).
169. Y.-S. Lee, *Principles Of Terahertz Science And Technology* (Springer Science & Business Media, New York, 2009).
170. R. W. Boyd, *Nonlinear Optics* (Academic Press, Burlington, 2008).
171. Z. Kai, S. Wei, X. DeGang, L. PengXiang, W. YuYe, M. JiaLin, Y. Chao, F. ShiJie, and Y. JianQuan, "Optically pumped terahertz sources," Science China Technological Sciences **60**(12), 1801-1818 (2017).
172. C. Staus, T. Kuech, and L. McCaughan, "Continuously phase-matched terahertz difference frequency generation in an embedded-waveguide structure supporting only fundamental modes," Optics Express **16**(17), 13296-13303 (2008).
173. Z. Ruan, G. Veronis, K. L. Vodopyanov, M. M. Fejer, and S. Fan, "Enhancement of optics-to-THz conversion efficiency by metallic slot waveguides," Optics Express **17**(16), 13502-13515 (2009).
174. A. Andronico, J. Claudon, J.-M. Gérard, V. Berger, and G. Leo, "Integrated terahertz source based on three-wave mixing of whispering-gallery modes," Optics Letters **33**(21), 2416-2418 (2008).
175. R. Sinha, M. Karabiyik, A. Ahmadivand, C. Al-Amin, P. K. Vabbina, M. Shur, and N. Pala, "Tunable, Room Temperature CMOS-Compatible THz Emitters Based on Nonlinear Mixing in Microdisk Resonators," Journal of Infrared, Millimeter, and Terahertz Waves **37**(3), 230-242 (2016).
176. R. Sinha, M. Karabiyik, C. Al-Amin, P. K. Vabbina, D. O. Guney, and N. Pala, "Tunable Room Temperature THz Sources Based on Nonlinear Mixing in a Hybrid Optical and THz Micro-Ring Resonator," Scientific Reports **5**(1), 9422 (2015).
177. K. M. Schulz, A. Rusche, A. Y. Petrov, and M. Eich, "Integrated Nonlinear Waveguide Optics for High-Efficiency and Wideband-Tunable Generation of THz Radiation," ACS Photonics **5**(9), 3779-3787 (2018).
178. J. H. Kim, S. Jung, Y. Jiang, K. Fujita, M. Hitaka, A. Ito, T. Edamura, and M. A. Belkin, "Double-metal waveguide terahertz difference-frequency generation quantum cascade lasers with surface grating outcouplers," Applied Physics Letters **113**(16), 161102 (2018).
179. C. Pflügl, M. A. Belkin, Q. J. Wang, M. Geiser, A. Belyanin, M. Fischer, A. Wittmann, J. Faist, and F. Capasso, "Surface-emitting terahertz quantum cascade laser source based on intracavity difference-frequency generation," Applied Physics Letters **93**(16), 161110 (2008).
180. W. Bogaerts, P. De Heyn, T. Van Vaerenbergh, K. De Vos, S. K. Selvaraja, T. Claes, P. Dumon, P. Bienstman, D. Van Thourhout, and R. Baets, "Silicon microring resonators," Laser & Photonics Reviews **6**(1), 47-73 (2012).
181. B. E. Little, S. T. Chu, H. A. Haus, J. Foresi, and J.-P. Laine, "Microring resonator channel dropping filters," Journal of Lightwave Technology **15**(6), 998-1005 (1997).
182. H. A. Haus and W. Huang, "Coupled-mode theory," Proceedings of the IEEE **79**(10), 1505-1518 (1991).
183. M. Soltani, "Novel Integrated Silicon Nanophotonic Structures Using Ultra-high Q Resonators," PhD Thesis (Georgia Institute of Technology, Atlanta, 2009).
184. D. G. Rabus, *Integrated Ring Resonators* (Springer, Berlin, Heidelberg, 2007).
185. K. Amarnath, "Active Microring And Microdisk Optical Resonators On Indium Phosphide," PhD Thesis (University of Maryland, Maryland, 2006).

186. A. Yariv, "Critical coupling and its control in optical waveguide-ring resonator systems," IEEE Photonics Technology Letters **14**(4), 483-485 (2002).
187. G. Boyd, T. Bridges, M. Pollack, and E. Turner, "Microwave nonlinear susceptibilities due to electronic and ionic anharmonicities in acentric crystals," Physical Review Letters **26**(7), 387-390 (1971).
188. S. B. Bodrov, A. N. Stepanov, M. I. Bakunov, B. V. Shishkin, I. E. Ilyakov, and R. A. Akhmedzhanov, "Highly efficient optical-to-terahertz conversion in a sandwich structure with $LiNbO_3$ core," Optics Express **17**(3), 1871-1879 (2009).
189. B. N. Carnio and A. Y. Elezzabi, "Enhanced broadband terahertz radiation generation near the reststrahlen band in sub-wavelength leaky-mode LiNbO3 waveguides," Optics Letters **43**(8), 1694-1697 (2018).
190. G. Poberaj, H. Hu, W. Sohler, and P. Gunter, "Lithium niobate on insulator (LNOI) for micro-photonic devices," Laser & Photonics Reviews **6**(4), 488-503 (2012).
191. M. Zhang, C. Wang, R. Cheng, A. Shams-Ansari, and M. Lončar, "Monolithic ultra-high-Q lithium niobate microring resonator," Optica **4**(12), 1536-1537 (2017).
192. V. S. Dmitry, M. Christoph, B. M. Andrey, G. L. S. Harald, and L. Gerd, "Nonlinear and quantum optics with whispering gallery resonators," Journal of Optics **18**(12), 123002 (2016).
193. A. I. Zhmakin, "Enhancement of light extraction from light emitting diodes," Physics Reports-Review Section of Physics Letters **498**(4), 189-241 (2011).
194. Y. Rao, W. J. Yang, C. Chase, M. C. Y. Huang, D. P. Worland, S. Khaleghi, M. R. Chitgarha, M. Ziyadi, A. E. Willner, and C. J. Chang-Hasnain, "Long-Wavelength VCSEL Using High-Contrast Grating," IEEE Journal of Selected Topics in Quantum Electronics **19**(4), 1701311 (2013).
195. L. Mahler, A. Tredicucci, F. Beltram, C. Walther, J. Faist, B. Witzigmann, H. E. Beere, and D. A. Ritchie, "Vertically emitting microdisk lasers," Nature Photonics **3**(1), 46-49 (2009).
196. Y. Jin, L. Gao, J. Chen, C. Wu, J. L. Reno, and S. Kumar, "High power surface emitting terahertz laser with hybrid second- and fourth-order Bragg gratings," Nature Communications **9**(1), 1407 (2018).
197. S. A. Schulz, T. Machula, E. Karimi, and R. W. Boyd, "Integrated multi vector vortex beam generator," Optics Express **21**(13), 16130-16141 (2013).
198. A. Z. Al-Attili, D. Burt, Z. Li, N. Higashitarumizu, F. Y. Gardes, K. Oda, Y. Ishikawa, and S. Saito, "Germanium vertically light-emitting micro-gears generating orbital angular momentum," Optics Express **26**(26), 34675-34688 (2018).
199. M. A. Ordal, R. J. Bell, R. W. Alexander, L. L. Long, and M. R. Querry, "Optical properties of Au, Ni, and Pb at submillimeter wavelengths," Applied Optics **26**(4), 744-752 (1987).
200. E. D. Palik, *Handbook Of Optical Constants Of Solids* (Academic press, San Diego, 1998).
201. J. Fürst, D. Strekalov, D. Elser, A. Aiello, U. L. Andersen, C. Marquardt, and G. Leuchs, "Low-threshold optical parametric oscillations in a whispering gallery mode resonator," Physical Review Letters **105**(26), 263904 (2010).
202. M.-C. Dicaire, "Generation Of Vortex Beam Superpositions Using Angular Gratings," Master's Thesis (University of Ottawa, Ottawa, 2017).
203. D. W. Vogt and R. Leonhardt, "Ultra-high Q terahertz whispering-gallery modes in a silicon resonator," APL Photonics **3**(5), 051702 (2018).
204. I. Moreno, J. A. Davis, I. Ruiz, and D. M. Cottrell, "Decomposition of radially and azimuthally polarized beams using a circular-polarization and vortex-sensing diffraction grating," Optics Express **18**(7), 7173-7183 (2010).
205. P. Chen, S.-J. Ge, W. Duan, B.-Y. Wei, G.-X. Cui, W. Hu, and Y.-Q. Lu, "Digitalized geometric phases for parallel optical spin and orbital angular momentum encoding," ACS Photonics **4**(6), 1333-1338 (2017).
206. W. Shu, X. Ling, X. Fu, Y. Liu, Y. Ke, and H. Luo, "Polarization evolution of vector beams generated by q-plates," Photonics Research **5**(2), 64-72 (2017).
207. J. D. Jackson, *Classical Electrodynamics* (Wiley, New Jersey, 1999).
208. J. Zhu, X. Cai, Y. Chen, and S. Yu, "Theoretical model for angular grating-based integrated optical vortex beam emitters," Optics Letters **38**(8), 1343-1345 (2013).

209. F. Pang, H. Zheng, H. Liu, J. Yang, N. Chen, Y. Shang, S. Ramachandran, and T. Wang, "The orbital angular momentum fiber modes for magnetic field sensing," IEEE Photonics Technology Letters **31**(11), 893-896 (2019).
210. I. M. Fazal, N. Ahmed, J. Wang, J.-Y. Yang, Y. Yan, B. Shamee, H. Huang, Y. Yue, S. Dolinar, and M. Tur, "2 Tbit/s free-space data transmission on two orthogonal orbital-angular-momentum beams each carrying 25 WDM channels," Optics Letters **37**(22), 4753-4755 (2012).
211. A. E. Willner, H. Huang, Y. Yan, Y. Ren, N. Ahmed, G. Xie, C. Bao, L. Li, Y. Cao, and Z. Zhao, "Optical communications using orbital angular momentum beams," Advances in Optics and Photonics **7**(1), 66-106 (2015).
212. M. Ren, J. Huang, H. Cai, J. M. Tsai, J. Zhou, Z. Liu, Z. Suo, and A.-Q. Liu, "Nano-optomechanical actuator and pull-back instability," ACS Nano **7**(2), 1676-1681 (2013).
213. S. L. Chuang, *Physics Of Photonic Devices* (John Wiley & Sons, New Jersey, 2009).
214. Y. Suematsu and K. Kishino, "Coupling coefficient in strongly coupled dielectric waveguides," Radio Science **12**(4), 587-592 (1977).
215. C. E. Campanella, C. M. Campanella, F. De Leonardis, and V. M. N. Passaro, "A high efficiency label-free photonic biosensor based on vertically stacked ring resonators," The European Physical Journal Special Topics **223**(10), 2009-2021 (2014).
216. C. Ciminelli, C. E. Campanella, F. Dell'Olio, and M. N. Armenise, "Fast light generation through velocity manipulation in two vertically-stacked ring resonators," Optics Express **18**(3), 2973-2986 (2010).
217. A. Yariv, "Universal relations for coupling of optical power between microresonators and dielectric waveguides," Electronics Letters **36**(4), 321-322 (2000).
218. P. T. Rakich, M. A. Popović, M. Soljačić, and E. P. Ippen, "Trapping, corralling and spectral bonding of optical resonances through optically induced potentials," Nature Photonics **1**(11), 658-665 (2007).
219. W. Liu and M. Asheghi, "Thermal conduction in ultrathin pure and doped single-crystal silicon layers at high temperatures," Journal of Applied Physics **98**(12), 123523 (2005).
220. B. Peng, Ş. K. Özdemir, W. Chen, F. Nori, and L. Yang, "What is and what is not electromagnetically induced transparency in whispering-gallery microcavities," Nature Communications **5**(1), 5082 (2014).
221. D. Van Thourhout and J. Roels, "Optomechanical device actuation through the optical gradient force," Nature Photonics **4**(4), 211-217 (2010).
222. M. L. Povinelli, M. Lončar, M. Ibanescu, E. J. Smythe, S. G. Johnson, F. Capasso, and J. D. Joannopoulos, "Evanescent-wave bonding between optical waveguides," Optics Letters **30**(22), 3042-3044 (2005).
223. T. Carmon, L. Yang, and K. J. Vahala, "Dynamical thermal behavior and thermal self-stability of microcavities," Optics Express **12**(20), 4742-4750 (2004).
224. Q. Xu and M. Lipson, "Carrier-induced optical bistability in silicon ring resonators," Optics Letters **31**(3), 341-343 (2006).
225. M. Xu, J. Wu, T. Wang, X. Hu, X. Jiang, and Y. Su, "Push–pull optical nonreciprocal transmission in cascaded silicon microring resonators," IEEE Photonics Journal **5**(1), 2200307 (2013).
226. G. S. Wiederhecker, L. Chen, A. Gondarenko, and M. Lipson, "Controlling photonic structures using optical forces," Nature **462**(7273), 633-636 (2009).
227. P. E. Barclay, K. Srinivasan, and O. Painter, "Nonlinear response of silicon photonic crystal microresonators excited via an integrated waveguide and fiber taper," Optics Express **13**(3), 801-820 (2005).
228. P. B. Deotare, I. Bulu, I. W. Frank, Q. Quan, Y. Zhang, R. Ilic, and M. Loncar, "All optical reconfiguration of optomechanical filters," Nature Communications **3**(1), 846 (2012).
229. M. Borselli, T. J. Johnson, and O. Painter, "Beyond the Rayleigh scattering limit in high-Q silicon microdisks: theory and experiment," Optics Express **13**(5), 1515-1530 (2005).
230. H. Xu, U. Kemiktarak, J. Fan, S. Ragole, J. Lawall, and J. M. Taylor, "Observation of optomechanical buckling transitions," Nature Communications **8**(1), 14481 (2017).

231. I. S. Grudinin, H. Lee, O. Painter, and K. J. Vahala, "Phonon Laser Action in a Tunable Two-Level System," Physical Review Letters **104**(8), 083901 (2010).
232. H. Jing, S. K. Özdemir, X.-Y. Lü, J. Zhang, L. Yang, and F. Nori, "PT-Symmetric Phonon Laser," Physical Review Letters **113**(5), 053604 (2014).
233. H. Jing, Ş. K. Özdemir, Z. Geng, J. Zhang, X.-Y. Lü, B. Peng, L. Yang, and F. Nori, "Optomechanically-induced transparency in parity-time-symmetric microresonators," Scientific Reports **5**(1), 9663 (2015).
234. T.-X. Lu, Y.-F. Jiao, H.-L. Zhang, F. Saif, and H. Jing, "Selective and switchable optical amplification with mechanical driven oscillators," Physical Review A **100**(1), 013813 (2019).
235. Ş. Özdemir, S. Rotter, F. Nori, and L. Yang, "Parity–time symmetry and exceptional points in photonics," Nature Materials **18**(8), 783-798 (2019).
236. M.-A. Miri and A. Alù, "Exceptional points in optics and photonics," Science **363**(6422), eaar7709 (2019).
237. P. Thiruvenkatanathan, J. Yan, J. Woodhouse, and A. A. Seshia, "Enhancing parametric sensitivity in electrically coupled MEMS resonators," Journal of Microelectromechanical Systems **18**(5), 1077-1086 (2009).